

Wideband, low loss feed integration with a Pyramidal Sinuous Antenna

by

Zainodean du Toit



*Thesis presented in partial fulfilment of the requirements
for the degree of Master of Engineering (Electrical &
Electronic) in the Faculty of Engineering at Stellenbosch
University*

Supervisor: Dr. C. Van Niekerk

Co-supervisor: Prof. D.I.L. de Villiers

March 2020

Declaration

Plagiarism is the use of ideas, material and other intellectual property of another's work and to present is as my own.

I agree that plagiarism is a punishable offence because it constitutes theft.

I also understand that direct translations are plagiarism.

Accordingly all quotations and contributions from any source whatsoever (including the internet) have been cited fully. I understand that the reproduction of text without quotation marks (even when the source is cited) is plagiarism.

I, the undersigned, declare that the work contained in this assignment is my original work and that I have not previously (in its entirety or in part) submitted it for grading in this module/assignment or another module/assignment.

Signature:
Z du Toit

Date: **March 2020**

Copyright © 2020 Stellenbosch University
All rights reserved

Abstract

Wideband, low loss feed integration with a Pyramidal Sinuous Antenna

Z. du Toit

*Department of Electrical and Electronic Engineering,
University of Stellenbosch,
Private Bag X1, Matieland 7602, South Africa.*

Thesis: MEng (E and E)

March 2020

In this thesis, a pyramidal sinuous antenna is designed to be integrated with a balun. This system is to be used as the feed of a shaped, offset Gregorian reflector.

Initially, a previously designed Marchand balun is chosen due to its maximum amplitude and phase unbalance of ± 0.2 dB and 1.5° , respectively. The balun matched the antennas 300Ω real input impedance component across a 4.5:1 band. A new descrambling network is also designed to allow for the integration of two baluns, yielding a dual polarised sinuous antenna. Using this descrambling network, simulations showed that the antenna and balun integration matched a previous, single polarised integration. The simulated reflection coefficient remained below -10 dB across the majority of the band, reaching a maximum of -7.5 dB. The simulated radiation pattern also showed symmetry across the band, with a BOR₁ (body of revolution type 1) efficiency above 90% and a reflector aperture efficiency above 70%. While the measured radiation pattern also showed symmetry, the reflection coefficient reached a maximum of -6 dB.

Due to the measured reflection coefficient of the integrated balun and antenna, a Phelan balun is designed and suggested as an improvement. This balun was chosen for its inherent 4:1 impedance transformation. Balun simulations showed a maximum amplitude unbalance of 0.02 dB, and a maximum phase unbalance of 3.5% across a 0.26-1.8 GHz range. The simulated and measured reflection coefficient for this balun remained well below -10 dB across the same range.

Opsomming

Wyeband, lae-verliesvoerintegrasië met 'n Piramidiese Sinusvormige Antenna

(“Wideband, low loss feed integration with a Pyramidal Sinuous Antenna”)

Z. du Toit

Departement Elektriese en Elektroniese Ingenieurswese,

Universiteit van Stellenbosch,

Privaatsak X1, Matieland 7602, Suid Afrika.

Tesis: MEng (E en E)

Maart 2020

In hierdie tesis is 'n piramidiese sinusvormige antenna ontwerp om met 'n balun geïntegreer te word. Hierdie stelsel moet dan gebruik word as voer vir 'n gevormde, gekompenseerde Gregoriaanse weerkaatser.

Aanvanklik word 'n voorheen ontwerpte Marchand-balun gekies as gevolg van sy maksimum amplitude en fase-onbalans van onderskeidelik ± 0.2 dB en 1.5° . Die balun pas by die antenna se 300Ω reële invoerimpedansie-komponent oor 'n band van 1.05-4.7 GHz. 'n Nuwe ontknopingsnetwerk is ook ontwerp om die inskakeling van twee baluns moontlik te maak, wat 'n dubbele gepolariseerde sinusvormige antenna lewer. Met behulp van hierdie ontknopingsnetwerk het simulaties getoon dat die antenna- en balun-integrasië ooreenstem met 'n vorige, enkel gepolariseerde integrasië. Die gesimuleerde weerkaatskoeffisiënt bly onder -10 dB oor die grootste deel van die band, en bereik 'n maksimum van -7.5 dB. Die gesimuleerde stralingspatroon het ook simmetrie oor die hele band getoon, met 'n BOR₁ doeltreffendheid bo 90% en 'n reflektoropening doeltreffendheid bo 70%. Terwyl die gemete stralingspatroon ook simmetrie getoon het, bereik die weerkaatskoeffisiënt 'n maksimum van -6 dB.

As gevolg van die gemete weerkaatskoeffisiënt van die geïntegreerde balun en antenna, word 'n Phelan-balun ontwerp en voorgestel as verbetering. Hierdie balun is gekies vir die inherente 4:1 impedansie transformasie. Simulasies het 'n maksimale amplitude-onbalans van 0.02 dB getoon, en 'n maksimum fase-onbalans van 3.5% oor 'n 0.26 - 1.8 GHz-reeks. Die gesimuleerde en gemete weerkaatskoeffisiënt vir hierdie balun het ver onder -10 dB oor dieselfde 0.26-1.8 GHz-reeks gebly.

Acknowledgements

I would like to express my sincere gratitude to the following people and organisations:

- My supervisors, Dr. C. Van Niekerk and Prof. D.I.L. de Villiers, for their valuable insight and incredible patience during the last two years.
- Both sets of parents, for their patience. Including my brother and sister, friends, and family.
- Everyone in S501 (The Penthouse), for tolerating the questions and conversations.
- Special thanks to Mr. Wessel Croukamp and Mr. Gift Lecholo, for building the balun and antennas.

Additionally, I would like to thank Prof. D.B. Davidson, Prof. D.I.L. de Villiers, and the following organisation for my bursary.

This research was supported by the South African Radio Astronomy Observatory, which is a facility of the National Research Foundation, an agency of the Department of Science and Technology.

Contents

Declaration	i
Abstract	ii
Opsomming	iii
Acknowledgements	iv
Contents	v
List of Figures	vii
List of Tables	x
1 Introduction	1
1.1 The Square Kilometre Array	1
1.2 Problem Statement	1
1.3 Thesis Overview and Chapter Layout	2
2 Sinuous Antennas	3
2.1 The Planar Sinuous Antenna	3
2.2 The Pyramidal Sinuous Antenna	9
2.3 Aperture Efficiency	14
2.4 Chapter Summary	17
3 Baluns	18
3.1 Balun Theory	18
3.2 Different Balun Types	20
3.3 Marchand Balun Characterisation	24
3.4 Chapter Summary	27
4 Sinuous Antenna Balun Integration	28
4.1 Substrate Free Sinuous Antenna	28
4.2 Two-arm Balun Integration	35
4.3 Four-arm Descrambling and Balun Integration	38
4.4 Efficiency as a Feed for the SKA Shaped Dish	47
4.5 Chapter Summary	49
5 Phelan Balun Design	50
5.1 Phelan Balun Theory	50

5.2	Design	52
5.3	Chapter Summary	57
6	Conclusion and Recommendations	59
6.1	Results Summary	59
6.2	Recommendations	60
	Bibliography	61

List of Figures

2.1	The formation of a single sinuous arm.	4
2.2	The four-arm planar sinuous antenna.	5
2.3	The surface current highlighting the active regions at three different frequencies, with the current direction in an active region.	6
2.4	Total E-field of the planar sinuous antenna for the $\phi = 0^\circ$ and $\phi = 90^\circ$ cuts.	7
2.5	Descrambling networks for the planar sinuous antenna.	8
2.6	Perspective view of the pyramidal sinuous antenna, showing the angle of inclination and ground plane height parameter.	9
2.7	A visual description of (2.8), showing a pair of opposing pins.	10
2.8	Two step method for measuring the differential electric field for one polarisation, following [9].	11
2.9	Diagrams of a single ended 4-port and differential 2-port devices, following [23].	12
2.10	Two step method for measuring the differential electric field for one polarisation.	13
2.11	Parabla's focal point with feed, showing the subtended angle θ_0	15
3.1	Examples of a balanced and unbalanced transmission line.	18
3.2	Illustration of even and odd modes. Here the odd mode forms a virtual short circuit and even mode forms a virtual open circuit, following [31].	19
3.3	Folded balun connected to a dipole, following [31].	21
3.4	Sleeve balun depicted with differential outputs A and B. These outputs can be connected to differential load, such as a dipole.	21
3.5	The balun as proposed by [32] with its equivalent circuit.	22
3.6	Planar Marchand balun	22
3.7	Phelan balun with current paths describing its operation, following [34].	23
3.8	Simplified equivalent circuit of the Phelan balun.	23
3.9	Marchand balun transmission line equivalent circuit, showing line impedances that are designed and optimised to minimise the reflection coefficient, with output amplitude and phase balance [10].	24
3.10	Four Marchand baluns with similar designs, with an opened balun for a cross sectional view.	25
3.11	Marchand balun reflection coefficient for set 1.	25
3.12	Marchand balun reflection coefficient for set 2.	26
3.13	Simulated amplitude and phase unbalance of the Marchand balun, from [10].	26
3.14	Reflection coefficient as a result of the direct sinuous antenna and balun integration, from [10].	27
4.1	Feeding region	29
4.2	Differential reflection coefficient and input impedance (real component) of base model.	29

4.3	The total E-Field of the base pyramidal sinuous antenna, showing rotational symmetry.	30
4.4	Complete pyramidal sinuous antenna with matching network.	31
4.5	Modified pyramidal sinuous antenna simulated reflection coefficient	32
4.6	The total E-Field of the modified pyramidal sinuous antenna.	32
4.7	Fabricated, substrate free pyramidal sinuous antenna.	33
4.8	Comparison of the measured and simulated E-field for the modified base model at 2 GHz, 4 GHz, and 6 GHz.	34
4.9	Modified pyramidal sinuous antenna measured reflection coefficient.	35
4.10	Two-arm feeding region, with new centre distance	36
4.11	Two-arm pyramidal sinuous antenna simulated reflection coefficient.	36
4.12	Two-arm sinuous antenna integrated with the Marchand balun.	37
4.13	Two-arm antenna and balun integrated simulated reflection coefficient.	37
4.14	Simulated E-field of the two-arm sinuous antenna for the $\phi = 0^\circ$ and $\phi = 90^\circ$ cuts.	38
4.15	The descrambling approach described by [14] to feed planar sinuous antennas with microstrip balun.	38
4.16	Implementation of the alternate descrambling method.	39
4.17	Alternate descrambling approach: Reflection coefficient.	39
4.18	Simulated E-field with alternate descrambling network for the $\phi = 0^\circ$ and $\phi = 90^\circ$ cuts.	40
4.19	New suggested descrambling method.	40
4.20	New descrambling method's with reflection coefficient for the Rogers4003C substrate.	41
4.21	New descrambling method's reflection coefficient for the Rogers5880 substrate.	42
4.22	Simulated E-field for the new descrambling method.	42
4.23	Four-arm sinuous antenna integrated with the Marchand balun.	43
4.24	New descrambling method's reflection coefficient for the Rogers4003C substrate.	43
4.25	Four-arm sinuous antenna integrated with the Marchand balun, including metal strips to add structural integrity.	44
4.26	Final four-arm sinuous antenna with added structural support.	44
4.27	Simulated E-field of the four-arm sinuous antenna with added structural support.	44
4.28	Fabricated pyramidal sinuous antenna with Marchand balun integration. Here the baluns are attached to the descrambling attachment points and glued onto the Rogers4003C substrate.	45
4.29	Measured reflection coefficient of the four-arm sinuous antenna.	45
4.30	Comparison of the measured and simulated E-field for the completed sinuous antenna at 1.1 GHz, 3 GHz, and 4.7 GHz.	47
4.31	Efficiencies of the simulated four-arm microstrip fed and the two-arm balun integrated antennas.	47
4.32	Efficiencies of the simulated four-arm final four-arm antenna, balun integrated.	48
5.1	Series and parallel load topology.	50
5.2	Uncompensated, resonant balun equivalent circuit.	51
5.3	Bandwidth ratio design curves for a given VSWR.	52
5.4	CST simulation models of the Phelan balun.	53
5.5	Simulated Phelan balun reflection coefficient.	54
5.6	The Phelan balun's output ports unbalance.	54

5.7	Power accepted per port showing that the input power divides evenly.	55
5.8	Comparison between the simulated and measured reflection coefficient.	55
5.9	Fabricated Phelan balun.	56
5.10	Another parallel connected balun topology, following [34].	57
5.11	Cross-section of simulated balun.	57
5.12	Simulated reflection coefficient of other parallel-connected balun topology.	57

List of Tables

2.1	Planar sinuous antenna parameter values and their descriptions	7
2.2	Pyramidal sinuous antenna parameters with descriptions	10
3.1	Fourth order Marchand balun design impedances	25
4.1	Base sinuous antenna design parameters	29
4.2	Matching network parameters for base pyramidal sinuous antenna	31
4.3	Two-arm sinuous antenna design parameters	36
5.1	Phelan balun design parameters	53

Chapter 1

Introduction

1.1 The Square Kilometre Array

The Square Kilometre Array (SKA) is an international project tasked with designing and building a radio telescope with a collecting area of 1 square kilometre. The construction of the SKA radio telescope is planned to take place over two phases, with 1 and 2 being abbreviated to SKA1 and SKA2, respectively. SKA1 is situated in both South Africa and Western Australia, while SKA2 is to be spread across other countries in Africa. The purpose of this international effort is to study important phenomena and problems encountered by the field of astronomy. The effort includes studying the formation of the universe and black holes, the formation of stars, other planets, and in general, other properties of the universe such as the distribution of energy and matter [1]. While the SKA is planned to start its operation below the 10 GHz range by the year 2020, there has already been a significant discovery by MeerKAT. The first four letters in MeerKAT translates to “more”, referencing its 64 antennas, while the “KAT” refers to Karoo Array Telescope. The discovery by astronomers, in layman terms, is radio bubbles at the centre of the Milky Way [2]. These bubbles were likely caused by an energy burst millions of years ago, relatively near the supermassive black hole in the Milky Way.

The scientific requirements of the SKA pose difficult engineering challenges. One of the important factors that describe the performance of a telescope is sensitivity. Sensitivity is defined by [3] as the ratio of effective collecting area to the system’s noise. This definition includes losses in and the efficiency of the total system. In [4], the design decisions that lead to maximising the sensitivity of MeerKAT are described. The maximisation problem was done by minimising the system temperature, resulting in a receiver temperature below 7 K. The reflector system that was designed for MeerKAT is a classical offset Gregorian dual-reflector system, fed by a corrugated horn antenna yielding an aperture efficiency above 74%.

1.2 Problem Statement

For a high aperture efficiency, the antenna pattern must remain constant across its band, while being rotationally symmetric to illuminate the reflector evenly. For antennas to yield symmetric and constant patterns, it must be fed by sources that have balanced amplitude and phase outputs across the band of interest. The work in this thesis contributes to the SKA by studying antenna characteristics, feeding methods, and devices called baluns

that can lead to symmetric antenna patterns. A natural challenge that arises from studies that investigate individual components of a system is their eventual integration. Thus, techniques for component integration are also covered, along with their fabrication feasibility. The antenna systems' aperture efficiency is also tested on the SKA's shaped offset Gregorian reflector, via simulation, to confirm the systems total efficacy.

1.3 Thesis Overview and Chapter Layout

The thesis covers the theory behind sinuous antennas and why its characteristics are desirable as a feed for reflectors. Following this, the theory behind baluns is discussed, along with the compatibility of the Marchand balun and the sinuous antenna. After their compatibility is confirmed, these devices are integrated. The Phelan balun is also investigated and suggested as an improvement for integration with the sinuous antenna. The thesis chapter layout, along with brief descriptions is given below:

- **Chapter 2:** This chapter discusses the mathematical description of the planar sinuous antenna structure, where its radiation mechanism is also described. It delves into a motivation for the pyramidal sinuous antenna, and descrambling networks available in the literature are reviewed. Descrambling networks are important for balun integration. The chapter ends with the definition of aperture efficiency.
- **Chapter 3:** The theory behind baluns is studied to understand their operation, and to find a suitable wideband balun to integrate with the sinuous antenna.
- **Chapter 4:** The feasibility of building a sinuous antenna without a substrate on its arms is investigated first. Subsequently, the sinuous antenna and Marchand baluns compatibility is methodically studied. After their compatibility for rotational radiation patterns is confirmed, they are integrated and a prototype is built and measured.
- **Chapter 5:** The Phelan balun is investigated in greater detail due to its inherent 4:1 impedance transformation characteristics. It is suggested for integration to allow for an improved reflection coefficient when compared to the Marchand balun. A Phelan balun is then designed, built, and measured to confirm its simulated performance.

Chapter 2

Sinuuous Antennas

This chapter covers some of the literature available on the planar and pyramidal sinuous antenna. Section 2.1 details the planar sinuous structure, including a brief discussion on how it is fed, and lastly, its radiation characteristics are shown. Section 2.2 shows a projection of the planar structure onto a pyramidal surface. Feeding the pyramidal projection is described briefly. Methods for measuring and extracting the differential reflection coefficient and field parameters are given for the specific case of operating the antenna without a balun. Following this, reflector aperture efficiency is covered. The chapter ends with a summary of the important findings in the literature.

2.1 The Planar Sinuous Antenna

V.H. Rumsey [5], in 1958, described a new class of antennas whose radiation pattern and impedance characteristics were, practically, independent of frequency. For scaling antennas, it was known that when the physical dimensions of an antenna were scaled by a factor of n (where $n \in \mathbb{R}$, $n > 0$), the antenna would retain its electrical properties if its frequency of operation was also scaled by the same factor n . The reasoning behind frequency independence was then that if an antenna was described entirely by angles, its electrical characteristics would be independent of frequency. From this, spiral, conical spiral, and log-periodic antennas were described. Among the list of log-periodic antennas came the focus of this chapter, the sinuous antenna, which was first described by R.H. Duhamel [6] in 1987.

2.1.1 Planar Sinuous Structure

The sinuous antenna is a quasi-log-periodic antenna that is capable of providing dual circular or linear polarisations with similar gain, radiation pattern, impedance, and bandwidth characteristics when compared to the singular polarised Archimedes and log-spiral antennas. The sinuous antenna is described as a quasi-log-periodic antenna (and therefore not truly frequency-independent) as its shape is not entirely specified by angles. The mathematical expression of a single sinuous arm is given by

$$\phi = (-1)^p \alpha_p \sin \left(\pi \frac{\ln \left(\frac{r}{R_p} \right)}{\ln(\tau_p)} \right) \pm \delta, R_p \leq r \leq R_1 \quad (2.1)$$

where r and ϕ are in spherical coordinates. Here, α denotes angular width, τ denotes growth rate, δ is a rotation angle about the origin, and R_p is the outer radius of a cell, with the subscript p defining the number of a cell, numbered 1 to p . A visual representation of (2.1) is given in Fig. 2.1a for $\delta = 0$. It shows points ‘abc’, which is how one sinuous cell is defined, along with its angular width on a domain $[R_1, R_p]$. When this curve is rotated about the origin by a non zero $\pm\delta$, a sinuous arm is formed as depicted in Fig. 2.1b. The points ‘d’ and ‘e’ are tapered down to the centre to allow for excitation.

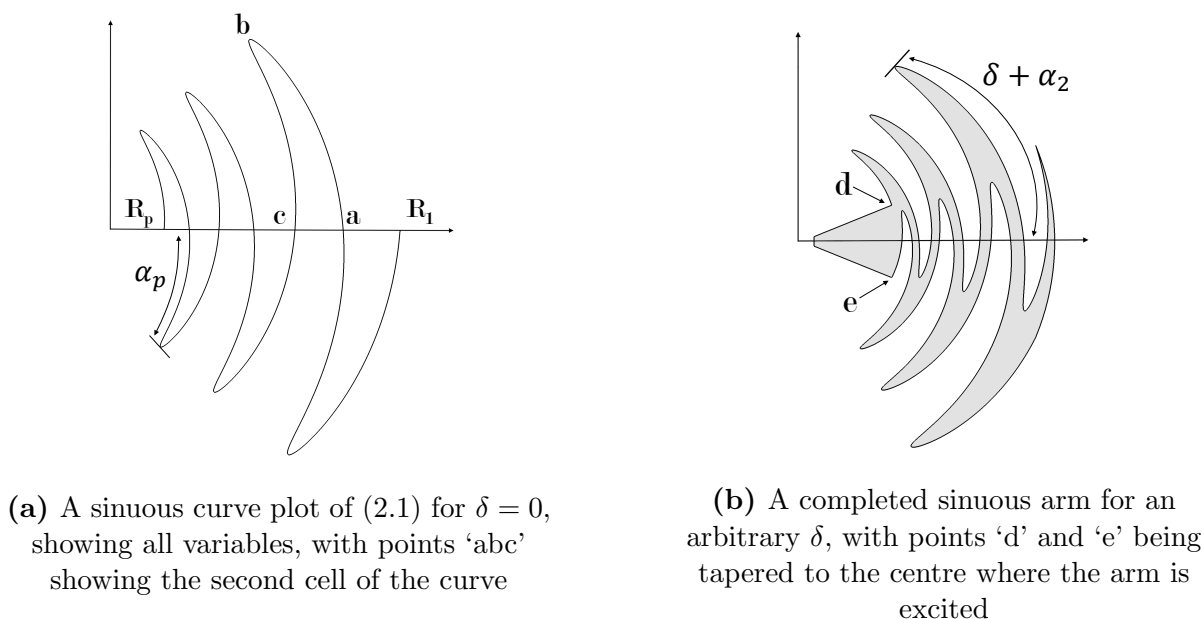


Figure 2.1: The formation of a single sinuous arm.

The radii R_{p+1} and R_p are related by the growth rate τ_p , where the radii are the ratio of the inner to the outer radius of a cell, respectively, given by

$$\tau_p = \frac{R_{p+1}}{R_p} \quad (2.2)$$

If the arm in Fig. 2.1b is copied $N \geq 2$ times and equally spaced in a manner such that a $360^\circ/N$ rotation about the origin gives the same structure, it yields a planar sinuous antenna¹. This is shown in Fig. 2.2 for $N = 4$.

From this, the planar sinuous structure can be described as self-complementary. This means that the grey conducting surface depicted in Fig. 2.2 is the same as the non-conducting white surface, only rotated by some angle. Self-complementary structures have a constant input impedance, regardless of the source frequency [7]. The requirement for a sinuous antenna to be self-complementary is given as $\delta = 180^\circ/2N$.

It is known that sinusoidal functions have an infinite domain if the range of its argument is rational and infinite. In the case of (2.1), it is truncated to allow for a finite structure; this introduces practicality. For the sinuous antenna, a finite structure implies that its bandwidth is limited by the start and end radii. The start and end radii can also be described as the high and low cut-off frequency radii, which will be denoted as R_{start} and R_{end} , respectively. To define R_{start} and R_{end} mathematically, an active region of a

¹It should be noted that $N = 2$ provides single polarisation only.

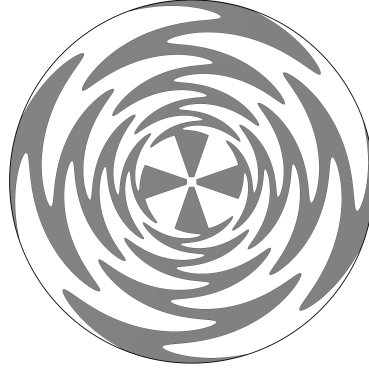


Figure 2.2: The four-arm planar sinuous antenna.

sinuous arm is defined first. An active region is the portion of a sinuous arm where most of the currents are radiated, and is highlighted in Fig. 2.3 at different frequency points. With reference to Fig. 2.1, it can be shown that

$$r(\alpha_p + \delta) = \frac{\lambda}{4} \quad (2.3)$$

with λ being a wavelength. This is due to the approximate length of a cell (a to b to c in Fig. 2.1) being $\lambda/2$ in an active region. Manipulating (2.3), R_{start} and R_{end} becomes

$$R_{start} = \frac{n_H \lambda_H}{4(\alpha_p + \delta)} \quad (2.4)$$

and

$$R_{end} = \frac{n_L \lambda_L}{4(\alpha_p + \delta)} \quad (2.5)$$

where λ_H and λ_L are the high and low cut-off wavelengths, respectively. Equations (2.4) and (2.5) are usually multiplied by some factor n_H and n_L ; n_H is to allow for a transition region between the source and the first active region. Both n_L and n_H reduce edge effects at the low and high-frequency cut-off points [8]–[10], and have typical values of 1.2 and 0.5, respectively.

2.1.2 Feeding the Planar Sinuous Antenna

Taking the self-complementary condition for a planar sinuous antenna into account, Deschamps formula can be used to determine the input impedance of each arm [11]. Deschamps formula is given by

$$z_m = \frac{\zeta}{4 \sin\left(\frac{\pi m}{N}\right)}, m \in \mathbb{Z}, m \neq 0 \quad (2.6)$$

where ζ is the intrinsic impedance of the medium surrounding a self-complementary structure, N is again the number of sinuous arms, and m denotes the voltage mode. If the medium is chosen as free space or air, it follows that $\zeta = 120\pi$, which results in each arm having an input impedance of 133Ω for mode 1 and $N = 4$. The excitation voltage is

$$V_{n,m} = A_m \exp\left(\frac{j2\pi nm}{N}\right) \quad (2.7)$$

where A_m is the amplitude of a given mode m , and n is the arm number up to N . All modes yield radiation patterns that have rotational symmetry, with modes $m = \pm 1$ being the only modes without broadside nulls [12]. In this thesis, the focus will be on mode $m = 1$ due to its radiation pattern characteristics being desirable for reflector feeds. From (2.7) for $N = 4$, it can be seen that opposite arms are out of phase by 180° , indicating that opposite arm pairs are to be excited differentially. As an example, for dual linear polarisation arms [1;2;3;4] (with arms 1,3 and 2,4 being opposite pairs), must have phase $[0^\circ;0^\circ;180^\circ;180^\circ]$. For circular polarisation, adjacent arms must have a 90° phase difference and opposite arms must have a 180° phase difference, i.e., $[0^\circ;90^\circ;180^\circ;270^\circ]$.

2.1.3 Radiation

For an explanation of how the sinuous antenna radiates, the active regions are highlighted by current densities in Fig. 2.3 at different frequencies.

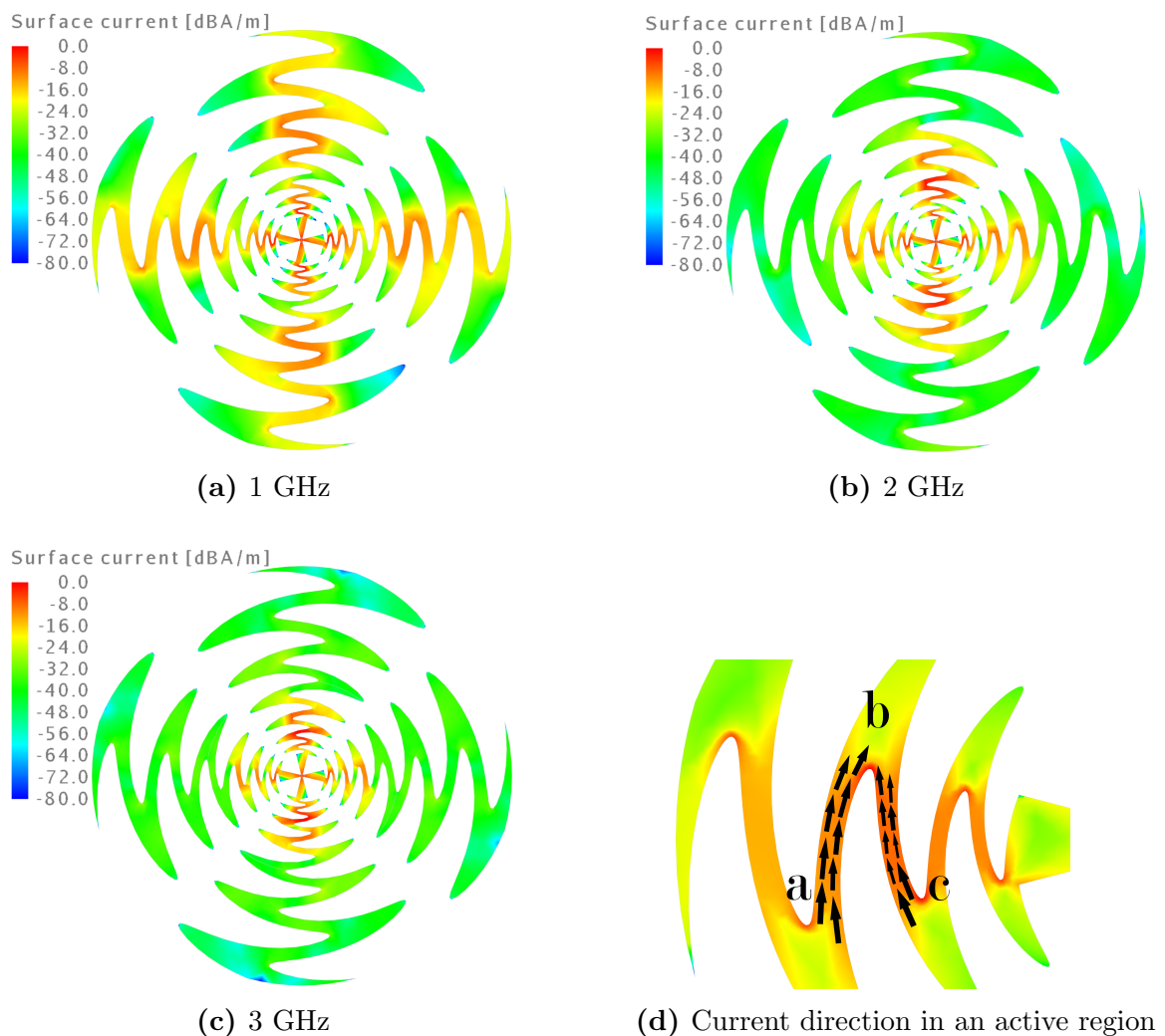


Figure 2.3: The surface current highlighting the active regions at three different frequencies, with the current direction in an active region.

In the discussion pertaining to Fig. 2.1, it is shown that active regions have an electrical path length of approximately $\lambda/2$. This path length causes a 180° phase delay for the currents at the start relative to the currents at the end. This means that the currents

at point ‘c’ are 180° out of phase with the currents at point ‘a’, as shown in Fig. 2.3d. The radiation for one arm for these currents is similar to the radiation mechanism of two wires or dipoles described in [13]. Now, consider a differentially fed two-arm sinuous antenna. The currents on the opposing arm would be similar to Fig. 2.3d, i.e, also pointing “upward”. This combination of currents (on the respective arms) would appear as two dipoles for that particular frequency, approximately $\lambda/2$ apart. This produces the single linear polarisation of the sinuous antenna. It should also be noted the areas where the surface currents are approximately -40 dBA are areas where the electrical path length is not an odd multiple of $\lambda/2$.

Design parameters from a previous study on the planar sinuous antenna [8] were used for simulation in FEKO [14]. The design parameter values and their descriptions are given in Table 2.1. The h parameter, ground plane height is added because the sinuous antenna radiates bidirectionally, while a unidirectional pattern is desired.

Table 2.1: Planar sinuous antenna parameter values and their descriptions

Parameter	Description	Design Value
α	Angular width	29°
δ	Rotation angle	15.94°
τ	Growth rate	0.830
h	Ground plane height	21 mm
f_{min}	Lowest frequency point (Determines outer radius)	2 GHz
f_{max}	Highest frequency point (Determines outer radius)	6 GHz

Polar plots of the radiation pattern can be seen in Fig. 2.4 for the $\phi = 0^\circ$ and $\phi = 90^\circ$ cuts. The antenna was excited with mode $m = 1$, with a voltage excitation that has phase $[0^\circ; 0^\circ; 180^\circ; 180^\circ]$ for dual linear polarisation. Only one polarisation is shown, as both are similar.

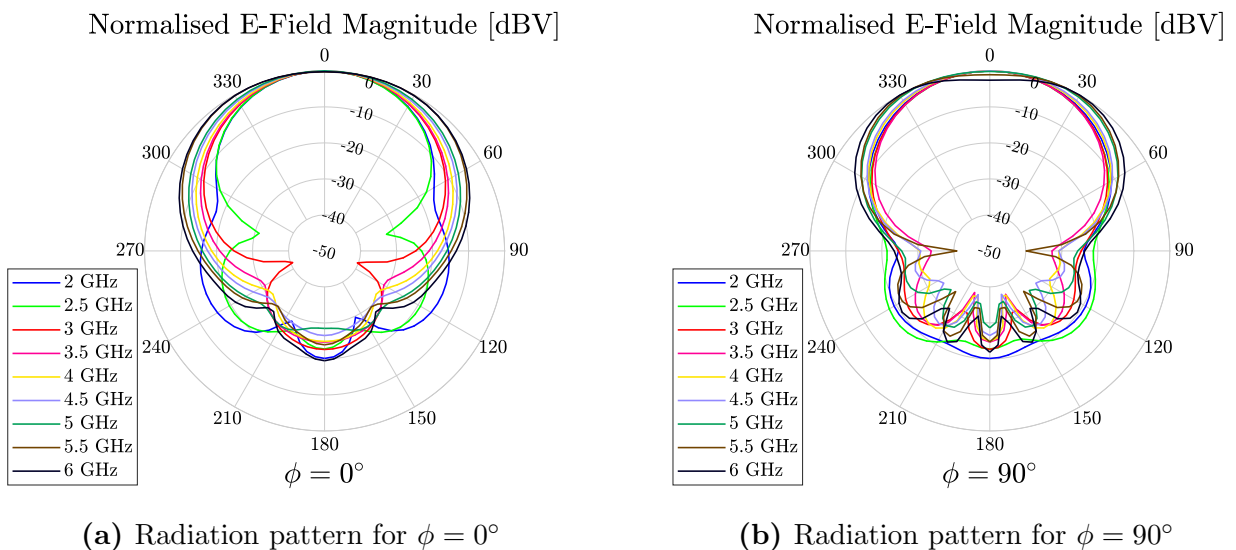
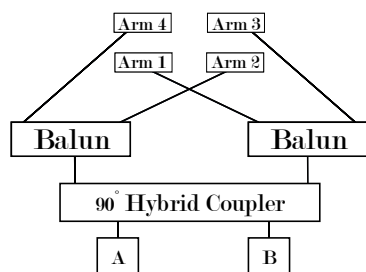


Figure 2.4: Total E-field of the planar sinuous antenna for the $\phi = 0^\circ$ and $\phi = 90^\circ$ cuts.

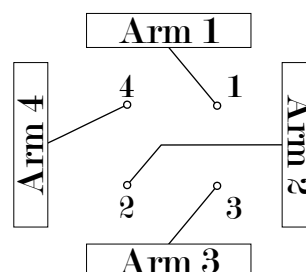
It is clear from the figure above that the planar sinuous antenna’s radiation pattern has rotational symmetry, confirming the theory in section 2.1.2.

Descrambling the Feeding Region

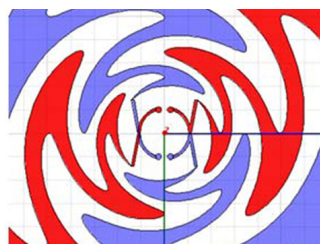
One of the characteristics that make the sinuous antenna appealing for use as a reflector feed is its rotationally symmetric radiation pattern. It is therefore important to consider the effect of feeding schemes that are asymmetric to avoid an asymmetric radiation pattern. The difficulty in feeding the sinuous antenna is due to its differential excitation requirement. From studying Fig. 2.5a, it becomes apparent that to keep all the line lengths the same on a planar surface, one pair of arms will require the output lines from the baluns to cross.



(a) DuHamel's suggestion for feeding a four-arm planar sinuous antenna for circular polarisation, following [6].



(b) A descrambling network for the balun outputs for excitation of both polarisations, following [15].



(c) A descrambling network from [16]. The red arms represents the top layer and blue arms shows the bottom layer of a substrate.

Figure 2.5: Descrambling networks for the planar sinuous antenna.

It is immediately understood that this not a practical solution for a planar surface. The literature has proposed descrambling networks for the balun connections to avoid any balun output line crossing. One such network is to lengthen one line and preserve the symmetry of at least one pair of arms, as shown in Fig. 2.5b, by [15]. Here a balun is connected to points 1 and 3, and another is connected to points 2 and 4. While this worked well at low frequencies, the radiation pattern lost rotational symmetry at higher frequencies. Another descrambling method is shown in Fig. 2.5c. This method achieved good rotational symmetry by maintaining an axial ratio below 2.5 dB, which is around 1 – 2.5 dB higher than previous methods in the literature [16]. For this network the line lengths are kept the same, however, all four arms are not on the same layer. The red arms are printed on the top layer and the blue arms are on the bottom layer. A network that uses a similar technique is described in [17]. As discussed in Chapter 4, this method will be too difficult for practical implementation when the planar sinuous is projected onto a pyramidal surface.

2.2 The Pyramidal Sinuous Antenna

The planar sinuous antenna can be projected onto a conical surface for unidirectional patterns, as well as for gain improvements [6]. It has also been projected onto a hemispherical surface [18] yielding 3:1 bandwidth. The conical sinuous antennas' parameters were optimised in [8] for reflector systems, as it was shown that the planar version was not suitable for use as a reflector feed. However, in the fabrication of this conical version, there was a difficulty in attaching the PCB etched sinuous arms onto the shape of a cone, which yielded undesirable results. A pyramidal projection was then suggested as this would reduce fabrication complexity, which was demonstrated in [9] for 3:1 bandwidth. For wider bands at higher frequencies, performance and efficiencies were adversely affected due to the presence of surface waves in the substrate of the sinuous arms. This was likely due to the substrates' physical thickness being kept constant, while its electrical thickness would increase or decrease with direct proportionality to frequency. A possible solution to this is to decrease the thickness of the substrate logarithmically, but this etching process would be expensive. A similar problem had been encountered by [19] in the design of a circular eleven feed. However, their solution was to scale the radiating elements instead. For the sinuous antenna, this would require scaling the active regions. During the rest of this thesis, the pyramidal sinuous antenna is investigated without using a substrate on the arms to avoid exciting surface waves.

2.2.1 Structure

The operation and structure of the pyramidal antenna are similar to that of its planar counterpart, with the difference being a projection 'upward' onto a pyramidal surface, as shown in Fig. 2.6. This introduces an angle of inclination as a parameter (the angle between the square base and any triangular face), which will be referred to symbolically as ψ . The set of parameters describing the pyramidal sinuous antenna is given in Table 2.2.

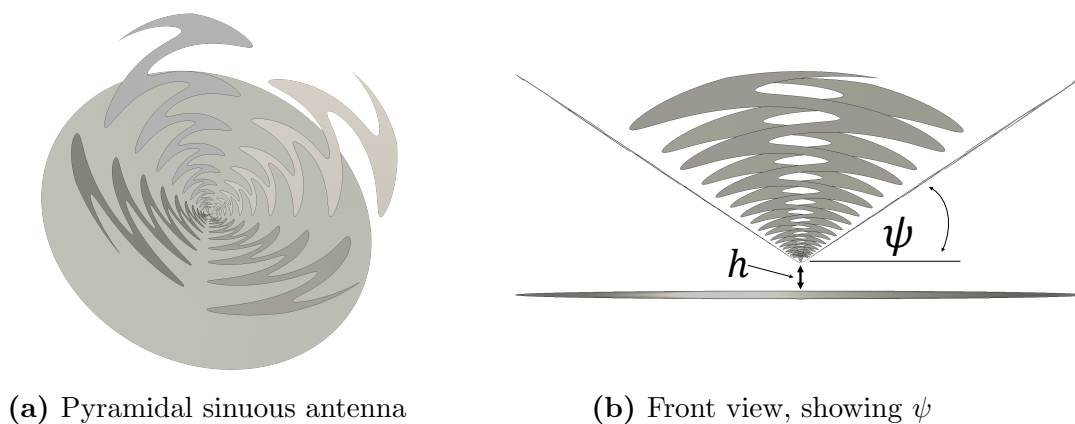


Figure 2.6: Perspective view of the pyramidal sinuous antenna, showing the angle of inclination and ground plane height parameter.

The pyramidal structure is supported by 4 pins of height ($h +$ thickness of the ground planes' substrate), as was done in [9]. An illustration of how the pins would connect to the sinuous arms can be found in Fig. 2.7. These pins are fed through the ground plane where it connected to a descrambling network. Physically, each arm can be supported individually by styrofoam trapezoidal prisms with angle ψ . The styrofoam material is

Table 2.2: Pyramidal sinuous antenna parameters with descriptions

Parameter	Description
α	Angular width
δ	Rotation angle
τ	Growth rate
h	Ground plane height
ψ	Angle of inclination
f_{min}	Lowest frequency point (Determines outer radius)
f_{max}	Highest frequency point (Determines inner radius)

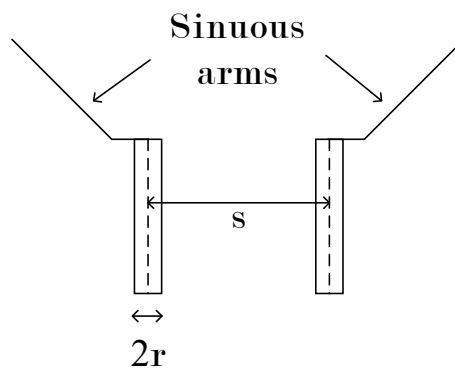
chosen for its ϵ_r (relative permittivity) of 1. Another solution is to hold each arm up with hollow, truncated metal cylinders with a radius equal to the ground plane. Metal cylinders can be used because most of the currents are radiated before they reach the transition region at the low-frequency point, as discussed for (2.5). This solution may provide a robust structure, however, this may influence the radiation pattern.

2.2.2 Feeding the Pyramidal Structure

With the structure being fed by 4 pins, each opposite pair of pins (Fig. 2.7) is treated as a parallel wire transmission line. Parallel wire transmission lines have a characteristic impedance given by [20]

$$Z_0 = \frac{1}{\pi\sqrt{\epsilon_r}} \sqrt{\frac{\mu_0}{\epsilon_0}} \operatorname{arccosh} \left(\frac{s}{2r} \right) \quad (2.8)$$

where s is the distance between opposing conductors' centres, r is their radii, and ϵ_r is the relative permittivity of the surrounding material, with μ_0 and ϵ_0 being the permeability and permittivity of free space, respectively.

**Figure 2.7:** A visual description of (2.8), showing a pair of opposing pins.

The characteristic impedance (2.8) must be matched with the differential impedance of opposing sinuous arms. As a result of symmetry between the lines and a differential excitation [9], [21], the differential impedance can be written as

$$Z_{\text{diff}} = 2Z_0 \quad (2.9)$$

where Z_{0o} is the odd mode impedance of a single transmission line. Furthermore, it can be written that

$$Z_{\text{diff}} = 2Z_0 \quad (2.10)$$

if the given lines are uncoupled. Here Z_0 is the characteristic impedance of the line. Similar to what was illustrated in Section 2.1.2, the pyramidal sinuous antenna is also excited by applying (2.7) with mode $m = 1$.

2.2.3 Parameter Extraction

If the sinuous antenna is operated without a balun, then some post-processing is required to retrieve the differential field and S-parameters. Due to a differential excitation scheme, these parameters cannot be measured directly on a Vector Network Analyser (VNA). A method for measuring these parameters will also be described.

Differential Field Extraction

A two-step method for measuring one polarisation of the sinuous antenna is shown in Fig. 2.8. In step 1 the electric field is measured from the single-ended port with a VNA while the antenna is in the anechoic chamber. The rest of arms are connected to $Z_0 = 50 \Omega$ loads². For step 2, the same is done to the opposing arm, again attaching $Z_0 = 50 \Omega$ loads to the unused arms. For reference, the left-most port measured in step 1 will be considered as port 1, with the rest of the ports being numbered in a clockwise direction. This means that the port measured in step 2 is numbered as 3. This 2-Step process is then repeated for the next set of opposing arms.

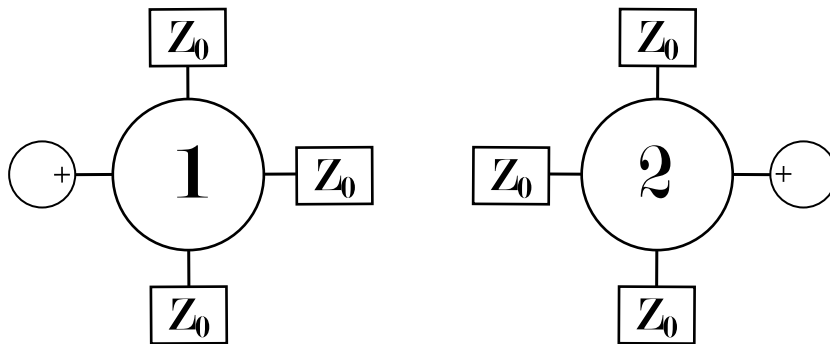


Figure 2.8: Two step method for measuring the differential electric field for one polarisation, following [9].

According to [9], [22], these single-ended electric field measurements can be used to obtain the differential and common mode field patterns via superposition, due to linearity. Therefore, once the first set of data has been measured, the differential and common mode fields can be calculated by

$$E_d(\theta, \phi) = \frac{\sqrt{2}}{2} [E_1(\theta, \phi) - E_3(\theta, \phi)] \quad (2.11)$$

and

²It should be noted that each arms' impedance has been stepped down to 50Ω , as in Chapter 4.

$$E_c(\theta, \phi) = \frac{\sqrt{2}}{2} [E_1(\theta, \phi) + E_3(\theta, \phi)], \quad (2.12)$$

where E_d is the differential mode field pattern, E_c is the common-mode field pattern, E_1 and E_3 represents port 1 and port 3, respectively. Equations (2.11) and (2.12) are only applicable when the single-ended ports have symmetry. For this thesis, only (2.11) will be used, due to the differential excitation requirement for a single polarisation.

Differential Reflection Coefficient Extraction

To calculate the differential reflection coefficient, mixed-mode S-parameters are considered. The term ‘‘mixed-mode S-parameters’’ is the combination of both differential and common mode S-parameters. The differential S-parameters will be derived as in [23].

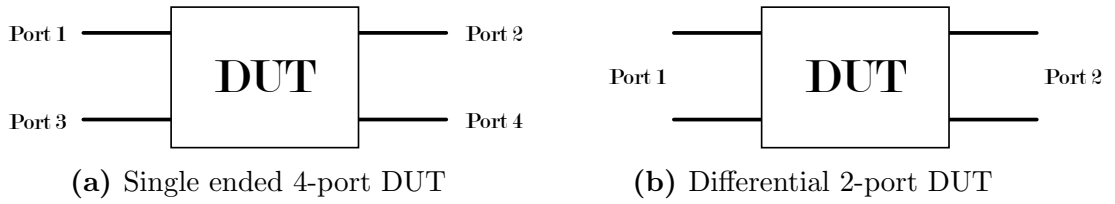


Figure 2.9: Diagrams of a single ended 4-port and differential 2-port devices, following [23].

Regarding the DUT (Device Under Test) in Fig. 2.9a, it is known that the so-called standard S-parameters of a 4-port DUT is given by

$$B_{std} = S_{std} A_{std} \quad (2.13)$$

$$\begin{bmatrix} b_1 \\ b_2 \\ b_3 \\ b_4 \end{bmatrix} = \begin{bmatrix} S_{11} & S_{12} & S_{13} & S_{14} \\ S_{21} & S_{22} & S_{23} & S_{24} \\ S_{31} & S_{32} & S_{33} & S_{34} \\ S_{41} & S_{42} & S_{43} & S_{44} \end{bmatrix} \begin{bmatrix} a_1 \\ a_2 \\ a_3 \\ a_4 \end{bmatrix} \quad (2.14)$$

where the incident wave and response matrices are given by A_{std} and B_{std} respectively.

The mixed-mode S-parameters is given by

$$\begin{bmatrix} b_{d1} \\ b_{d2} \\ b_{c1} \\ b_{c2} \end{bmatrix} = \begin{bmatrix} S_{d1d1} & S_{d1d2} & S_{d1c1} & S_{d1c2} \\ S_{d2d1} & S_{d2d2} & S_{d2c1} & S_{d2c2} \\ S_{c1d1} & S_{c1d2} & S_{c1c1} & S_{c1c2} \\ S_{c2d1} & S_{c2d2} & S_{c2c1} & S_{c2c2} \end{bmatrix} \begin{bmatrix} a_{d1} \\ a_{d2} \\ a_{c1} \\ a_{c2} \end{bmatrix}. \quad (2.15)$$

For readability, the differential and common mode S-parameters in are denoted by S_{didj} and S_{cicj} , respectively, where $i, j = \{1, 2\}$. Here the upper half of the B and A matrices describe a differential source and response, respectively, and the upper left quadrant of the s-matrix describes the performance as a result of the differential source. If port 1 and 3 (same for port 2 and 4) in Fig. 2.9 is used as a single differential port, a transformation matrix

$$M = \frac{\sqrt{2}}{2} \begin{bmatrix} 1 & 0 & -1 & 0 \\ 0 & 1 & 0 & -1 \\ 1 & 0 & 1 & 0 \\ 0 & 1 & 0 & 1 \end{bmatrix} \quad (2.16)$$

can be used to relate the standard S-parameters to the mixed mode S-parameters. This matrix M is set up by using the standard incident and response matrix to create a mixed-mode response. Using M, the mixed-mode incident and response matrices can be formulated as

$$A_{mm} = M A_{std} \quad (2.17)$$

$$B_{mm} = M B_{std}. \quad (2.18)$$

Lastly, relating the standard S-parameters to the mixed mode S-parameters yields

$$S_{mm} = M S_{std} M^{-1} = \begin{bmatrix} S_{d1d1} & S_{d1d2} & S_{d1c1} & S_{d1c2} \\ S_{d2d1} & S_{d2d2} & S_{d2c1} & S_{d2c2} \\ S_{c1d1} & S_{c1d2} & S_{c1c1} & S_{c1c2} \\ S_{c2d1} & S_{c2d2} & S_{c2c1} & S_{c2c2} \end{bmatrix} \quad (2.19)$$

$$= \frac{1}{2} \begin{bmatrix} S_{11} - S_{13} - S_{31} + S_{33} & S_{12} - S_{14} - S_{32} + S_{34} & S_{11} + S_{13} - S_{31} - S_{33} & S_{12} + S_{14} - S_{32} - S_{34} \\ S_{21} - S_{23} - S_{41} + S_{43} & S_{22} - S_{24} - S_{42} + S_{44} & S_{21} + S_{23} - S_{41} - S_{43} & S_{22} + S_{24} - S_{42} - S_{44} \\ S_{11} - S_{13} + S_{31} - S_{33} & S_{12} - S_{14} + S_{32} - S_{34} & S_{11} + S_{13} + S_{31} + S_{33} & S_{12} + S_{14} + S_{32} + S_{34} \\ S_{21} - S_{23} + S_{41} - S_{43} & S_{22} - S_{24} + S_{42} - S_{44} & S_{21} + S_{23} + S_{41} + S_{43} & S_{22} + S_{24} + S_{42} + S_{44} \end{bmatrix}.$$

From (2.19), only the differential reflection coefficient S_{d1d1} is of interest, which is calculated as

$$S_{d1d1} = S_{11} - S_{13} - S_{31} + S_{33}. \quad (2.20)$$

In order to perform the measurement of ports 1 and 3 as shown in (2.20), the 2-Step process in Fig. 2.10 is considered.

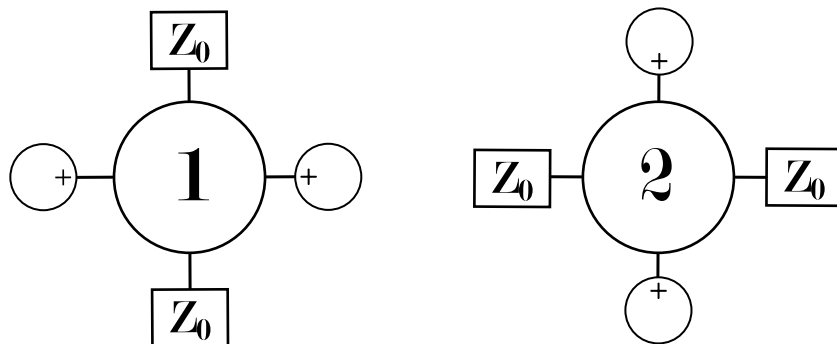


Figure 2.10: Two step method for measuring the differential electric field for one polarisation.

Again, 50Ω loads are attached to the unused ports. In step 1, the left-most port is port 1, and the opposing port is port 3. These measurements are repeated in step 2 where ports 2 and 4 are measured, and S_{d1d1} is calculated accordingly.

2.3 Aperture Efficiency

As a result of the sinuous antennas rotationally symmetric radiation pattern, it is tested as a feed for a SKA reflector system. The reflector antenna system of interest is the SKA's shaped offset Gregorian reflector, a method for deriving a mapping function for this reflector is described in [24]. This section will briefly cover the definitions and equations that measure the performance of reflector antennas, from [25]. A performance metric often used for reflectors is aperture efficiency, which can be factorised into various sub-efficiencies as in [26]. Code that calculates these efficiencies was developed by members of the electromagnetics engineering group at Stellenbosch University. At this stage, it should be noted calculations with the code was performed with the assistance of a colleague [F. Mokhupuki 2019, personal communication, 12 November].

Aperture efficiency can be written as

$$\eta_{ap} = \eta_{BOR_1} \eta_{sp} \eta_{ill} \eta_{ph} \eta_{pol} \quad (2.21)$$

where

- η_{BOR_1} is the BOR₁ (Body of Revolution Type 1) efficiency,
- η_{sp} is spillover efficiency,
- η_{ill} is illumination efficiency,
- η_{ph} is phase efficiency, and
- η_{pol} is the polarisation efficiency.

There are other factors that influence aperture efficiency, such as reflector surface tolerances, aperture blockages, and edge diffraction efficiencies. These factors aren't taken into account in this thesis. To define these efficiencies, preamble mathematics is covered first. In general, a radiation pattern defined in terms of an electric field $\mathbf{E}(r, \theta, \phi)$ can be written as [27], [28]

$$\mathbf{E}(r, \theta, \phi) = \frac{1}{r} \exp(-jkr) \mathbf{G}(\theta, \phi) \quad (2.22)$$

$$\mathbf{G}(\theta, \phi) = \mathbf{G}_\theta(\theta, \phi) \hat{\boldsymbol{\theta}} + \mathbf{G}_\phi(\theta, \phi) \hat{\boldsymbol{\phi}} \quad (2.23)$$

where r is the length from an observation point to the phase reference, k is the wave number, $\exp(-jkr)$ is the phase factor, and $\mathbf{G}(\theta, \phi)$ is the far-field pattern. The unit vectors $\hat{\boldsymbol{\theta}}$ and $\hat{\boldsymbol{\phi}}$ are in the θ and ϕ directions, respectively, of a spherical coordinate system. In spherical coordinates, the far-field has 2π periodicity and thus can be written as a Fourier series

$$\mathbf{G}_\theta(\theta, \phi) = \sum_{n=0}^{\infty} [A_n(\theta) \sin(n\phi) + B_n(\theta) \cos(n\phi)] \quad (2.24)$$

$$\mathbf{G}_\phi(\theta, \phi) = \sum_{n=0}^{\infty} [C_n(\theta) \cos(n\phi) - D_n(\theta) \sin(n\phi)] \quad (2.25)$$

where $A_n(\theta)$, $B_n(\theta)$, $C_n(\theta)$, and $D_n(\theta)$ are the Fourier coefficients. The $\mathbf{G}_\theta(\theta, \phi)$ and $\mathbf{G}_\phi(\theta, \phi)$ field components can be discretised as in [28] and the Fourier coefficients can be calculated with the discrete inverse Fourier transform.

Next, from Ludwig's third definition [29], the co- and cross-polar fields in the $\phi = 45^\circ$ plane are calculated from the Fourier coefficients as in [25]. It should be noted that the rest of this section considers a BOR₁ antenna excited with a $\hat{\mathbf{y}}$ directed incremental electric current. This results in an excitation of $A_1(\theta)$ and $C_1(\theta)$ in (2.24). An $\hat{\mathbf{x}}$ directed current would excite $B_1(\theta)$ and $D_1(\theta)$ in (2.25). Now the co- and cross-polar fields are calculated as

$$CO(\theta) = \frac{1}{2} [A_1(\theta) + C_1(\theta)] \quad (2.26)$$

$$XP(\theta) = \frac{1}{2} [A_1(\theta) - C_1(\theta)]. \quad (2.27)$$

It should be noted that the following equations describe the efficiency of a parabolic reflector with a subtended angle θ_0 , as shown in Fig. 2.11. The sub-efficiencies that are calculated with the subtended angle θ_0 are the spillover, illumination, phase, and polarisation efficiencies.

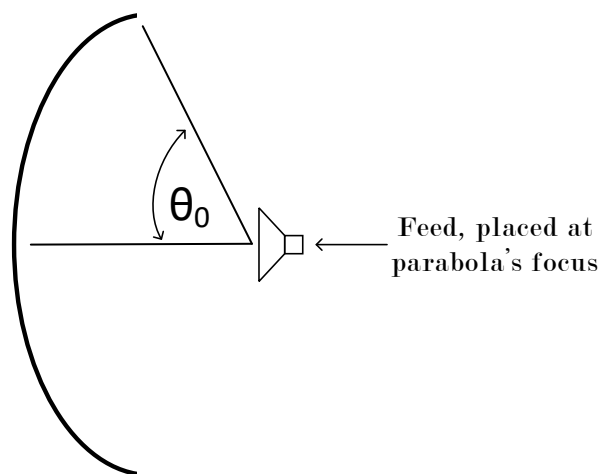


Figure 2.11: Parabla's focal point with feed, showing the subtended angle θ_0 .

BOR₁ Efficiency

In spherical coordinates, the subscript '1' in BOR₁ is a reference 1st order azimuthal variation of an E-fields' $\hat{\theta}$ and $\hat{\phi}$ components. Thus, BOR₁ efficiency defined as the ratio of the power radiated in the 1st order ϕ mode to the total radiated power. The subscript '1' in this definition also refers to the first subscript in the mode description of a circular cylindrical waveguide. As a result, this efficiency is calculated as

$$\eta_{BOR_1} = \frac{\int_0^{2\pi} \int_0^\pi [|G_{\theta 1}|^2 + |G_{\phi 1}|^2] \sin \theta d\theta d\phi}{\int_0^{2\pi} \int_0^\pi [|G_\theta(\theta, \phi)|^2 + |G_\phi(\theta, \phi)|^2] \sin \theta d\theta d\phi} \quad (2.28)$$

with

$$G_{\theta_1} = A_1(\theta) \sin \phi + B_1(\theta) \cos \phi \quad (2.29)$$

$$G_{\phi_1} = C_1(\theta) \cos \phi + D_1(\theta) \sin \phi \quad (2.30)$$

and the denominator in (2.28) is equivalent to

$$\pi \int_0^\pi [|A_1(\theta)|^2 + |B_1(\theta)|^2 + |C_1(\theta)|^2 + |D_1(\theta)|^2] \sin \theta d\theta. \quad (2.31)$$

Spillover Efficiency

Spillover efficiency is the total power that reaches the surface of the reflector in relation to the total power radiated from a feed. The spillover efficiency is critical in radio astronomy applications and must be as high as possible to reduce system noise. The spillover efficiency is given by

$$\eta_{sp} = \frac{\int_0^{\theta_0} [|CO(\theta)|^2 + |XP(\theta)|^2] \sin \theta d\theta}{\int_0^\pi [|CO(\theta)|^2 + |XP(\theta)|^2] \sin \theta d\theta}. \quad (2.32)$$

Illumination Efficiency

Illumination efficiency describes a feeds' radiation pattern variation on the surface of a reflector [13]. This is calculated as

$$\eta_{ill} = 2 \cot^2 \left(\frac{\theta_0}{2} \right) \frac{\left[\int_0^{\theta_0} |CO(\theta)| \tan \left(\frac{\theta}{2} \right) d\theta \right]^2}{\int_0^{\theta_0} |CO(\theta)|^2 \sin \theta d\theta}. \quad (2.33)$$

Phase Efficiency

Phase efficiency is a measure of the phase uniformity in the co-polar field and is written as

$$\eta_{ph} = \frac{\left| \left[\int_0^{\theta_0} CO(\theta) \tan \left(\frac{\theta}{2} \right) d\theta \right] \right|^2}{\left[\int_0^{\theta_0} |CO(\theta)| \tan \left(\frac{\theta}{2} \right) d\theta \right]^2}. \quad (2.34)$$

Polarisation Efficiency

Polarisation efficiency is defined as the ratio between the co-polar field power to the total field power, as

$$\eta_{pol} = \frac{\int_0^{\theta_0} [|CO(\theta)|^2] \sin \theta d\theta}{\int_0^{\theta_0} [|CO(\theta)|^2 + |XP(\theta)|^2] \sin \theta d\theta}. \quad (2.35)$$

2.4 Chapter Summary

Firstly, the planar sinuous antennas structure is described mathematically, with a brief analysis on how a sinuous arm is formed. Following the analysis of the sinuous arm, the antennas feeding and radiation characteristics are discussed. In this discussion, it was found that the planar sinuous antenna has an input impedance of approximately 133Ω with a rotationally symmetric radiation pattern. In terms of feeding the sinuous antenna, various descrambling methods that are available in the literature is shown. Secondly, a motivation for the pyramidal sinuous antenna is given. The differences between the planar and pyramidal structure are presented, along with the necessary feed changes that are required for the pyramidal structure. Methods for extracting the measured differential electric field and differential reflection coefficient is covered. These methods are to be used with a 4-port sinuous antenna fed with impedance transforming microstrip lines. Lastly, the aperture efficiency of reflector antennas is discussed, along with the sub-efficiencies that are calculated in later chapters.

Chapter 3

Baluns

In this thesis, a large part of the work was to integrate an existing balun with the pyramidal sinuous antenna. Another portion also includes a balun design. It is therefore important to study the literature available on baluns. Section 3.1 reviews the operation of baluns and why they are necessary for certain applications. Various baluns are then discussed in section 3.2. Next in section 3.3, the coaxial Marchand balun and its operation are discussed due to its wideband performance, and suitability for integration with the sinuous antenna. Lastly, a Phelan balun is covered in section 3.2.4 and is suggested as an improvement over the coaxial Marchand balun.

3.1 Balun Theory

The main function of a balun is to transform an unbalanced single-ended transmission line into a balanced differential transmission line with equal magnitude and an accurate phase difference of 180° . In devices such as mixers, push-pull amplifiers, and oscillators, a balun is necessary to provide phase transformation between other unbalanced and balanced devices. For oscillators and power amplifiers, operation without a balun can result in low output power and poor efficiencies [30]. Given that antennas are either balanced or unbalanced, baluns also find use as feeds for antennas that require a balanced, differential input. Though not a requirement, another characteristic of some baluns are that they also provide impedance transformation, which is desirable for antennas as their input impedance is not necessarily 50Ω .

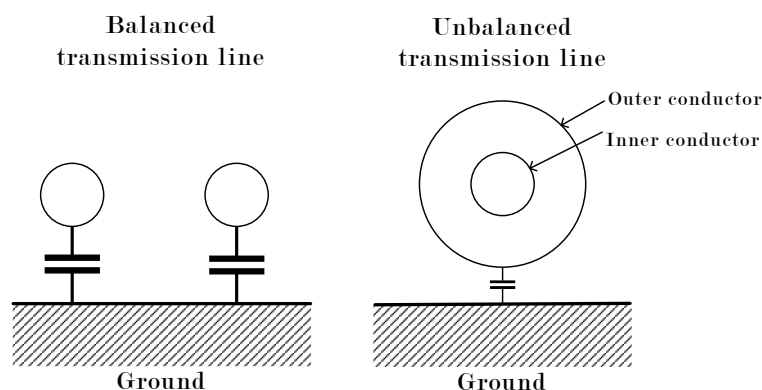


Figure 3.1: Examples of a balanced and unbalanced transmission line.

To aid the understanding of why baluns are necessary, inherently balanced and unbalanced structures are first studied as in [13], [31]. In Fig. 3.1, both such structures are shown. Due to the presence of the ground plane, these transmission lines are regarded as a three-wire transmission line. The parallel wire transmission line is an example of a balanced structure; this twin line can support currents of equal magnitude with a 180° phase difference, with each line having an equal capacitance to ground. On the coaxial transmission line on the right, it is shown that there is an unequal capacitance to ground for the inner and outer conductors, with the only the outside face of an outer conductor having a direct connection. As a result, this structure cannot support currents of equal magnitude and 180° phase difference because both currents do not follow the same path to ground.

3.1.1 Even and Odd Mode Excitation

In section 3.2, a folded balun will be shown to have a similar structure to a balanced transmission line by using even and odd mode excitations as in [31]. It is therefore important to cover the fundamentals of this method. By using the principle of superposition, the total excitation at a port will be the sum of its even and odd modes, due to their linearity. To do this simply, Fig. 3.2 is studied, assuming equal loads at ports 2 and 4. For the odd mode (balanced mode), ports 1 and 3 have sources with voltages that excite currents of equal magnitude but with a 180° phase difference. This configuration forms a virtual short circuit where E-field is normal to the plane of symmetry between the transmission lines.

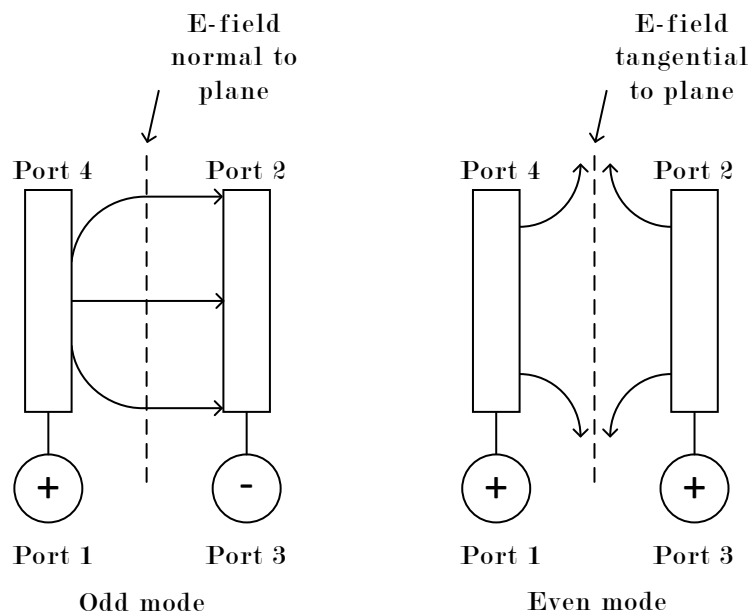


Figure 3.2: Illustration of even and odd modes. Here the odd mode forms a virtual short circuit and even mode forms a virtual open circuit, following [31].

For the even mode (unbalanced mode), ports 1 and 3 have sources with voltages that excite currents of equal magnitude and phase. This configuration forms a virtual open circuit where the E-field is tangential to the plane of symmetry between the transmission lines.

3.1.2 Transmission Line Input Impedance

Quarter-wavelength transformations of transmission lines that are terminated in either a short or open-circuit are used in nearly every balun structure. As a result, it is briefly covered in this section. From [21] the input impedance of a lossless transmission line terminated with a load Z_L was calculated as

$$Z_{\text{in}} = Z_0 \frac{Z_L + j Z_0 \tan \beta l}{Z_0 + j Z_L \tan \beta l} \quad (3.1)$$

where β is the propagation constant, l is the length of the transmission line, and $j = \sqrt{-1}$. For a short-circuit termination $Z_L = 0$, thus the input impedance is then calculated as

$$Z_{\text{in,sc}} = j Z_0 \tan \beta l \quad (3.2)$$

and for an open-circuit termination, $Z_L \rightarrow \infty$. Computing this limit for (3.1)

$$Z_{\text{in,oc}} = Z_0 \lim_{Z_L \rightarrow \infty} \frac{Z_L + j Z_0 \tan \beta l}{Z_0 + j Z_L \tan \beta l} = -j Z_0 \cot \beta l. \quad (3.3)$$

From the asymptotes and roots of (3.2) and (3.3), it is noted that when a signal travels for a quarter-wavelength (that is $\beta l = -\lambda/4$, from $\beta l = 0$), it observes an open-circuit and short-circuit, respectively. This is a useful result as it can be used to preserve the operation of a load (such as an antenna) attached to a balun, as will be demonstrated in section 3.2.

3.2 Different Balun Types

In this section, different supplementary baluns are discussed to understand their operation. As mentioned in Chapter 2, the sinuous antenna has a wideband operation and will, therefore, require a wideband balun. Thus, baluns described in [13], [31] are studied to understand their operation.

3.2.1 Folded Balun

A folded balun is depicted in Fig. 3.3, already integrated with a dipole antenna. The structure starts with an unbalanced coaxial input, which splits into two sections. On the left-hand side, the input transmission lines' outer conductor is attached to a dipole arm. On the right, a dummy cylinder of length L is connected to the outer conductor of the input line. This connection also forms a ground for the balun. The dummy cylinder has the same radius as the input coaxial line and is also connected to the other arm of the dipole. Finally, the centre conductor of the input line is connected to the dummy cylinder.

For an even mode excitation, an E-field tangential to the plane of symmetry between the dummy line and input is formed. This plane of symmetry runs through the ground of the balun. As a result, the balun is now equivalent to a single transmission line with an open-circuit at the ground connection. If L is a quarter wavelength at the frequency of operation, that is $L = \lambda/4$, then there is a short-circuit between the dipole arms. Any even mode currents are thus shorted at the input. For an odd mode excitation, the E-fields are normal to the plane of symmetry between the dummy line and input, again running through the ground connection. The result is a shorted stub in parallel with the dipole arm, with the outer conductors forming a balanced transmission line

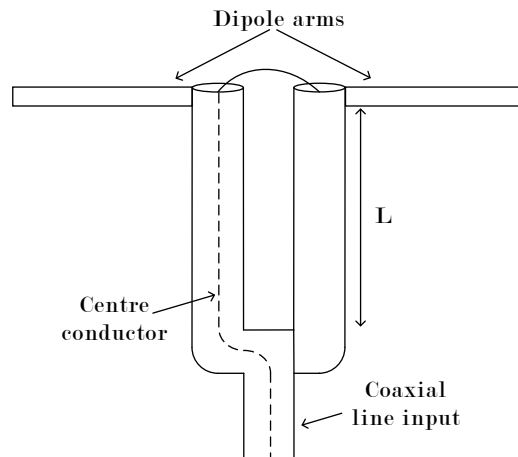


Figure 3.3: Folded balun connected to a dipole, following [31].

as in Fig. 3.1. This means that for $L = \lambda/4$, the dipole arm will observe an infinite impedance, and its operation won't be affected by the addition of the stub. With this configuration, any unbalanced currents will observe the same impedance to ground, and will thus be cancelled at the ground connection due to their equal magnitude and 180° phase difference. This balun has narrowband functionality, and the length L is only chosen as a quarter-wavelength (or as an odd, positive integer multiple of a quarter wavelength) to preserve the operation of the dipole antenna. The currents will still be cancelled if another length L is used.

3.2.2 Sleeve Balun

The sleeve baluns' structure consists of an input coaxial line with a "sleeve" shorted to the inputs' outer conductor. The top end of the sleeve remains unconnected and has length L . The outputs A and B can be connected to a differential load such as an antenna (as in Fig. 3.3).

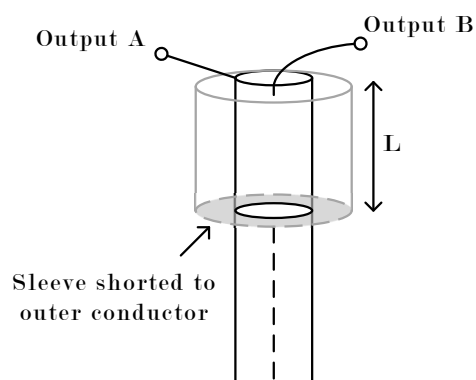


Figure 3.4: Sleeve balun depicted with differential outputs A and B. These outputs can be connected to differential load, such as a dipole.

To study the operation of this balun, Fig. 3.4 is considered first without its sleeve. If a differential load is connected directly to the output, the current at output A will observe this loads' impedance, and an impedance to ground via the outer conductor of

the input line. Depending on the magnitude of the impedance to ground, the current at point A will divide between the load and ground, resulting in unbalanced currents at both outputs. With the addition of a sleeve with $L = \lambda/4$ at the frequency of operation, the impedance to the ground can be made sufficiently large so that any current to ground is minimised. This is due to the shorted point being transformed into an open-circuit. This configuration is relatively simple to implement and results in balanced currents, however, it has a narrow bandwidth due to the length requirement of $L = \lambda/4$.

3.2.3 Roberts and Marchand Balun

Roberts balun [32] is similar to the folded balun, with the difference being an extension of the centre conductor into the “dummy” cylinder. The balun and its equivalent circuit are depicted in Fig. 3.5.

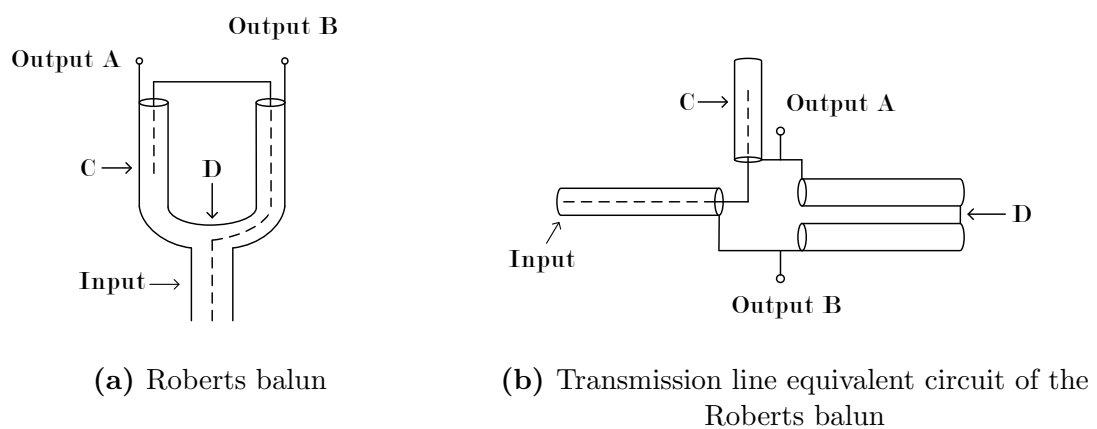


Figure 3.5: The balun as proposed by [32] with its equivalent circuit.

The extension of the centre conductor, depicted as point 'C', creates an open-circuited stub with the dummy cylinder. It should be noted that the centre is no longer connected to the outer conductor as with the folded balun. For an odd mode excitation, a dual resonance caused by the new addition of the open-circuited stub's reactance, and the existing short-circuited stub's reactance of the folded balun. The result of the opposing reactance is a bandwidth wider than the folded balun, as it is capable of 10:1 bandwidth ratios. This balun is known as a compensated balun, as the shorted lines' reactance is compensated for by the open-circuited stub.

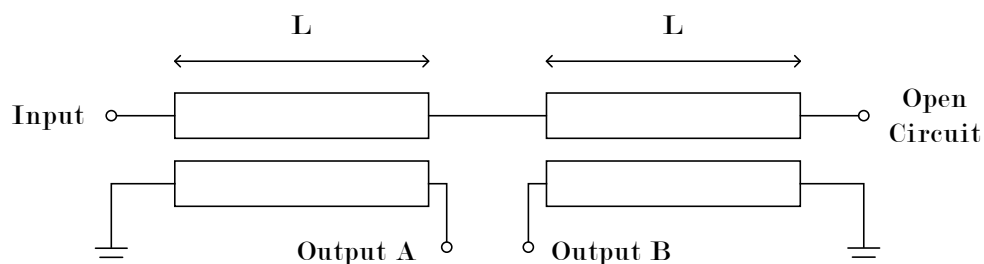


Figure 3.6: Planar Marchand balun.

This equivalent compensated balun was first described by N. Marchand in 1944 and later reinvented by W.K. Roberts in 1957 as stated by [33]. In the following sections, this balun will be referred to as the Marchand balun to follow the literature. An equivalent balun can also be realised as a coupled planar structure with transmission line lengths $L = \lambda/4$ as in Fig. 3.6.

3.2.4 Phelan Balun

The Phelan balun is a parallel-connected, uncompensated resonant balun capable of 25:1 bandwidth ratios [34]. The balun consists of a coaxial input and outputs, and a solid dummy rod, all surrounded by a cavity as in Fig. 3.7. The purpose of the dummy rod is to maintain symmetry inside the cavity.

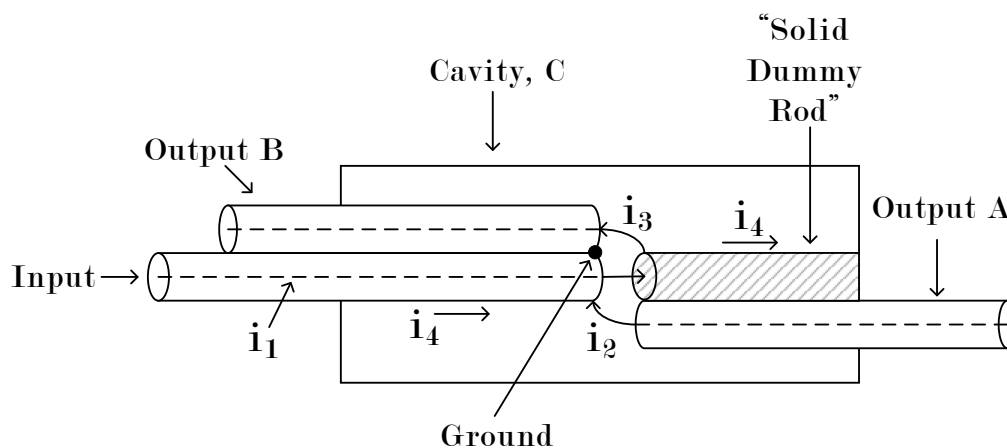


Figure 3.7: Phelan balun with current paths describing its operation, following [34].

With regards to the operation of the balun, the current i_1 divides into currents i_2 and i_3 . Also of note here is that i_1 is in phase with i_3 (output B), and 180° out of phase with i_2 (output A). Both of the outputs are also connected in parallel with the cavity. With the current directions defined, a simplified equivalent circuit can be formulated as in Fig. 3.8.

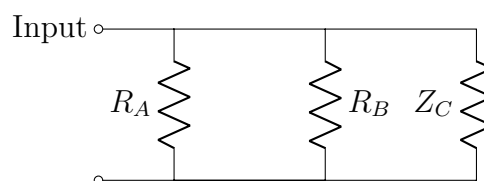


Figure 3.8: Simplified equivalent circuit of the Phelan balun.

At the resonant frequency of the cavity, its impedance approaches infinity and thus only the impedances A and B are seen at the input. Outputs A and B must be connected to a balanced load, that is $R_A = R_B = Z_L/2$, which gives the balun an inherent 4:1 impedance transformation. As a result, the balun also yields an inherent 4:1 bandwidth ratio. This will be covered more extensively in Chapter 5.

3.3 Marchand Balun Characterisation

In [10] a planar and coaxial, resonant version of the Marchand balun was designed and fabricated for integration with a pyramidal sinuous antenna. This section presents the coaxial version's design process and performance metrics from that work. The balun has a 4.5:1 bandwidth, with a frequency range of 1.05 GHz to 4.7 GHz.

3.3.1 Fourth-Order Marchand Balun Design

The compensated Marchand balun, also known as the fourth-order Marchand balun, has an equivalent transmission line equivalent circuit as in Fig. 3.9. Starting from the left-hand side, Z_0 is the input impedance of a source, Z_1 is used for quarter-wave input impedance transformation, Z_b is the open-circuited line compensating for the short-circuit reactance (and also for symmetry inside the cavity), Z_{ab} is the cavity's impedance that is shunted at the balun junction, and lastly Z_4 is for matching the balun junction's impedance to the load, Z_L .

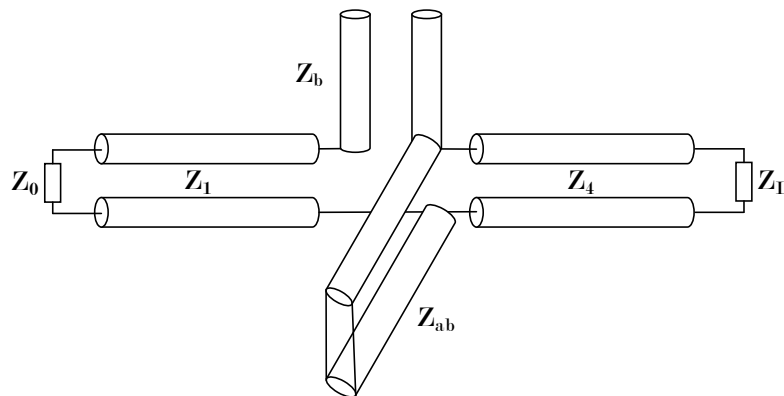


Figure 3.9: Marchand balun transmission line equivalent circuit, showing line impedances that are designed and optimised to minimise the reflection coefficient, with output amplitude and phase balance [10].

In 1979, a method for solving the impedances in Fig. 3.9 was used by [35]. However, in 1994, closed-form expressions for minimising the reflection coefficient of the first, second, third, and fourth-order Marchand balun was derived by [36]. These closed-form expressions allowed for simpler implementation in Computer-Aided Design (CAD) packages and was thus used as a starting point for the impedance calculations. With a source impedance of $Z_0 = 50 \Omega$, the load impedance $Z_L = 300 \Omega$ was chosen to match the real impedance of the pyramidal sinuous antenna. The final results are shown in Table 3.1.

The impedances Z_1 , Z_b , and Z_{ab} can then be converted to their coaxial transmission line equivalence by computing

$$Z = \sqrt{\frac{\mu}{\epsilon}} \frac{\ln(b/a)}{2\pi} \quad (3.4)$$

where a and b are the radii of the centre and outer conductors, respectively. The twin transmission line dimensions of Z_4 can be calculated by using (2.8).

Table 3.1: Fourth order Marchand balun design impedances

Design Parameter	Impedance
Z_1	90 Ω
Z_b	104 Ω
Z_4	165 Ω
Z_{ab}	130 Ω
Z_0	50 Ω
Z_L	300 Ω

3.3.2 Balun Performance

A model of the balun with the parameters found in Table 3.1 was constructed in FEKO and CST [37] to calculate its reflection coefficient, amplitude and phase balance. After the simulated results were found to be acceptable, four balun's were fabricated and are displayed in Fig. 3.10.

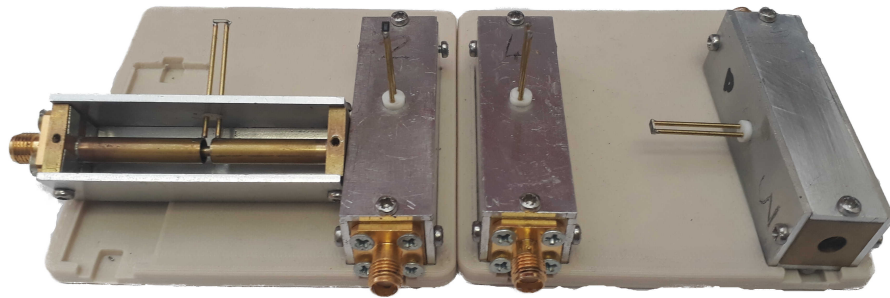


Figure 3.10: Four Marchand baluns with similar designs, with an opened balun for a cross sectional view.

The simulated and measured reflection coefficients of the baluns are presented in Figs. 3.11 and 3.12. Set 1 consists of balun A and B, with set 2 being C and D.

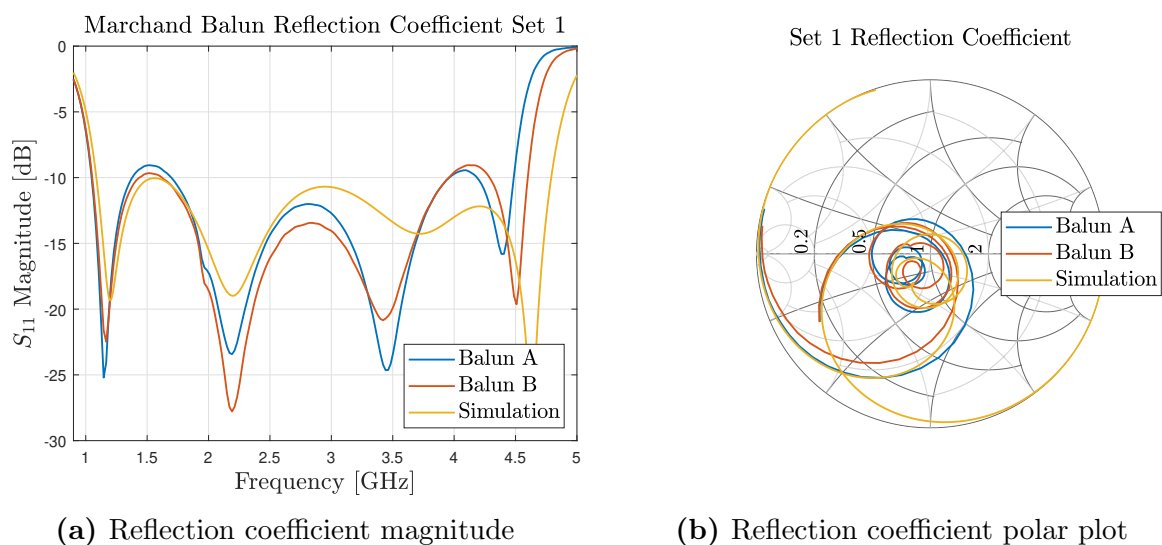


Figure 3.11: Marchand balun reflection coefficient for set 1.

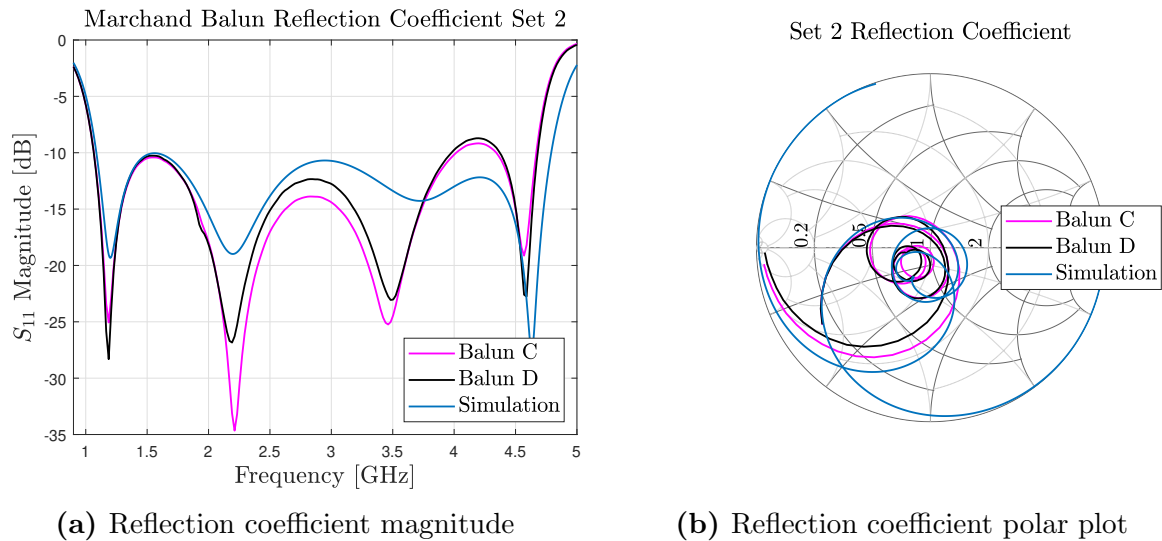


Figure 3.12: Marchand balun reflection coefficient for set 2.

The fabricated baluns' show consistency in their measured reflection coefficients, with both sets remaining below -10 dB across most of the 1-5 GHz band. However, set 2 shows a slight improvement of around 1.5 GHz.

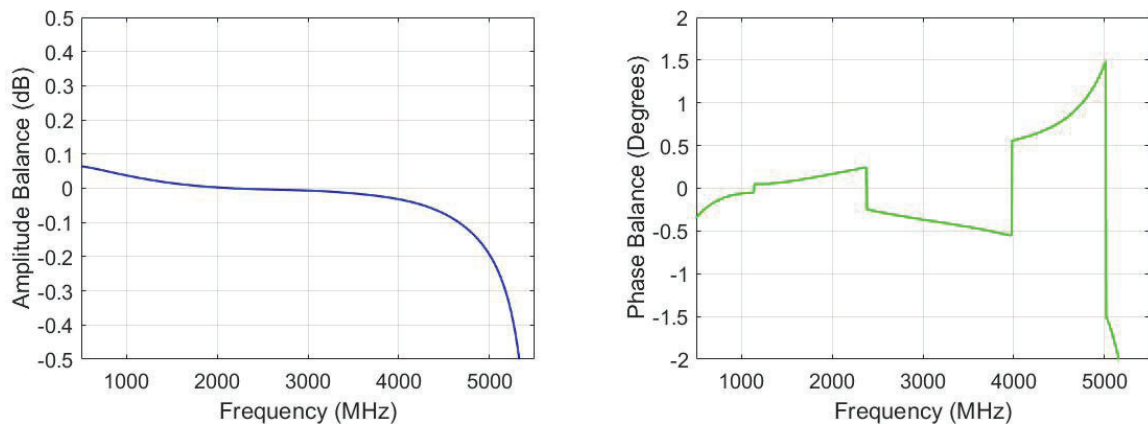


Figure 3.13: Simulated amplitude and phase unbalance of the Marchand balun, from [10].

The simulated amplitude and phase unbalance of this Marchand balun are shown in Fig. 3.13. The maximum amplitude unbalance is ± 0.2 dB, and maximum phase unbalance is 1.5° across the 1-5 GHz band of interest. Based on these results, baluns C and D are chosen for integration with a sinuous antenna.

In [10], the balun was directly connected with a two-arm sinuous antenna. The results are shown in Fig. 3.14, along with an image of the antenna and balun integration in simulation. While the result remains below -10 dB across most of the 1.05-4.7 GHz band, there are some peaks at -7.5 dB. This is because the balun was optimised for a 300Ω load, thus only the real component of the antennas impedance. Any input reactance from the

antenna was ignored. However, due to its excellent amplitude and phase balance, it was decided to match this performance with an indirect connection for a four-arm sinuous antenna. The reason is that the amplitude and phase balance would yield rotationally symmetric antenna patterns, which could result in high aperture efficiency when used as a feed for a reflector. It should be noted that the reflection coefficient shown in Fig 3.14a will be considered as acceptable for the integrated antenna and balun simulations and fabrication in the rest of the thesis.

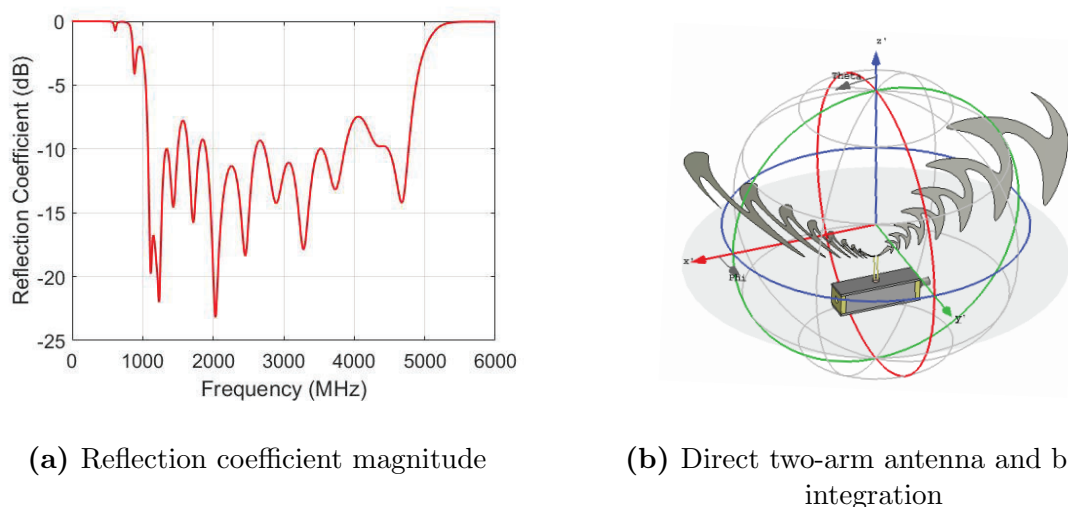


Figure 3.14: Reflection coefficient as a result of the direct sinuous antenna and balun integration, from [10].

3.4 Chapter Summary

Firstly, the necessity and main functions of baluns were discussed in terms of structures that are inherently unbalanced/balanced. Next, the theory needed to understand the operation of the baluns discussed in this thesis is covered, such as even and odd mode excitations and transmission line input impedance. By the principle of superposition, the total excitation of a balun (or any other structure) can be divided into their even (common mode) and odd (differential mode) excitations due to its linearity.

Subsequently, various baluns were investigated, namely the folded, sleeve, Roberts and/or Marchand, and Phelan balun. Here it was found that the Roberts/Marchand and Phelan balun have suitable wideband impedance transformation properties. A Marchand balun design from [10] is then characterised. This design is then chosen due to its amplitude and phase balance characteristics, which may yield rotationally symmetric antenna patterns. It has a bandwidth ratio of 4.5:1, with a maximum amplitude unbalance of ± 0.2 dB, and a maximum phase unbalance of 1.5° across the balun's 1-5 GHz band. The goal was therefore set to match the performance found with a two-arm sinuous antenna to that of a four-arm sinuous antenna.

Chapter 4

Sinuuous Antenna Balun Integration

In Chapter 3, the Marchand balun was chosen as a suitable candidate for integration with a pyramidal sinuous antenna. Thus, this chapter investigates the performance of this choice as a feed for the sinuous antenna, and of the resulting system as a feed for reflectors. The first section (4.1) investigates the difficulties in designing and fabrication of a sinuous antenna without a substrate on the arms. This is done to avoid exciting surface waves, which can result in degraded antenna performance in wideband applications. Section 4.2 follows the simulation of integrating the coaxial Marchand balun to a two-arm pyramidal sinuous antenna. This is followed by a four-arm integration with a new descrambling network in section 4.3. Its manufacturing process is discussed, with a comparison of its simulated and measured performance. Lastly, the reflector efficiency of each antenna is calculated as a feed for the SKA shaped dish, in section 4.4.

4.1 Substrate Free Sinuous Antenna

In section 2.2, a motivation for a pyramidal sinuous antenna without a substrate on its arms was given. Such an antenna without a substrate presents a structural difficulty, as the feeding pins alone cannot support the weight and angle of each arm. It was then decided that the arms will be supported by blocks styrofoam, cut to the desired angle of the pyramidal shape. This choice of material has the added advantage of having a dielectric constant that is approximately the same as free space, which reduces computational times of Method of Moment (MoM) solvers like FEKO. Thus, this section follows the design of a pyramidal sinuous antenna with four single-ended ports as a feasibility study.

4.1.1 Design and Simulation

For the design and simulation procedure, the base pyramidal sinuous antennas' performance is first established. Following this, the base model is modified to introduce 4 single-ended ports with impedance transforming lines.

Base model

A frequency range of 2-6 GHz was chosen for this design, resulting in a 3:1 bandwidth ratio. The antenna can in principle be scaled to any bandwidth ratio due to its frequency independence, however manufacturing becomes difficult for higher frequencies due to the small size of the feed region. The 2-6 GHz range makes this antenna manufacturable. The

parameters describing the antenna are given in Table 4.1, and its feeding region can be seen in Fig. 4.1. A model of this sinuous antenna can be seen in Fig. 2.6. The following results were computed in FEKO by using an edge port as a differential source, with an input impedance of 300Ω that matches the mean of Fig. 4.2b. Considering that this is a MoM solver, the triangle edge length of each mesh cell was equated to $1/12$ the wavelength at the highest frequency to ensure accuracy. Opposing arms had a phase difference of 180° for dual linear polarisation. This is the setup that will be used in FEKO for this section unless stated otherwise.

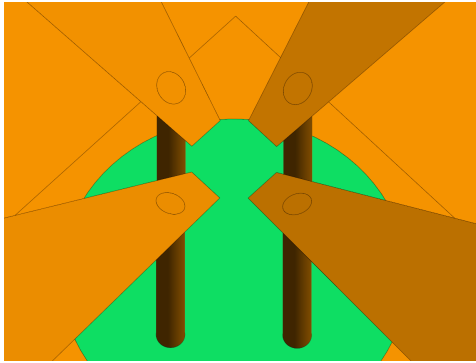
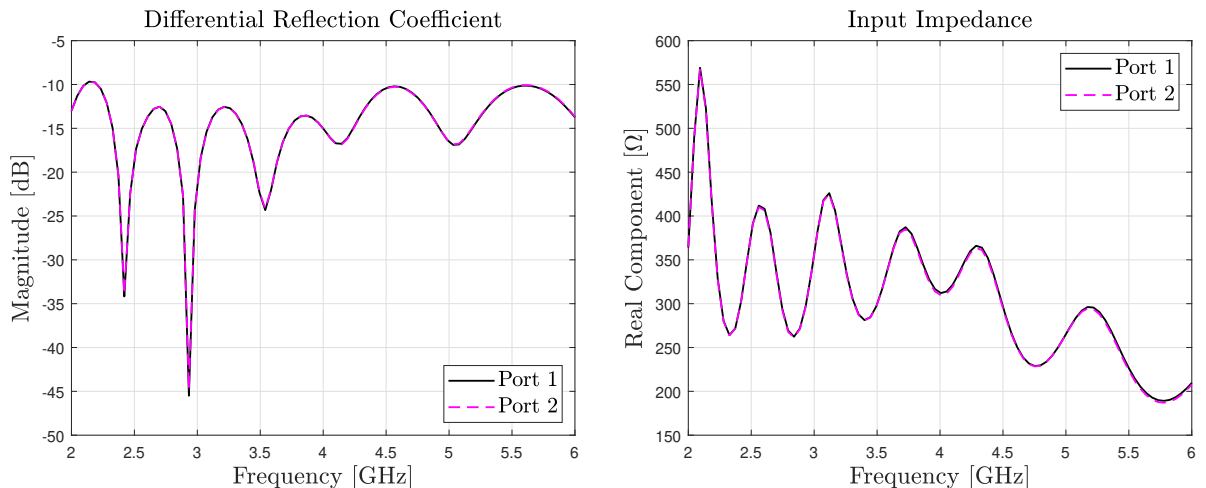


Figure 4.1: Feeding region

Table 4.1: Base sinuous antenna design parameters

Parameter	Value
α	24.85°
δ	14.95°
τ	0.842
h	5 mm
ψ	33.52°
f_{min}	2 GHz
f_{max}	6 GHz

The reflection coefficient and the input impedance of the resultant model are presented in Fig. 4.2. Figure 4.2a shows that the reflection remains below -10 dB across the majority of the band, which is a result similar to what was found in [9].



(a) Differential reflection coefficient as seen by port 1 and 2

(b) Real component of input impedance as seen by port 1 and 2

Figure 4.2: Differential reflection coefficient and input impedance (real component) of base model.

The total, normalised E-field of the base model is shown in Fig. 4.3, maintaining the constant radiation property across frequency found with the planar sinuous antenna as in section 2.1. It should be noted that only one polarisation is shown as both polarisations are similar.

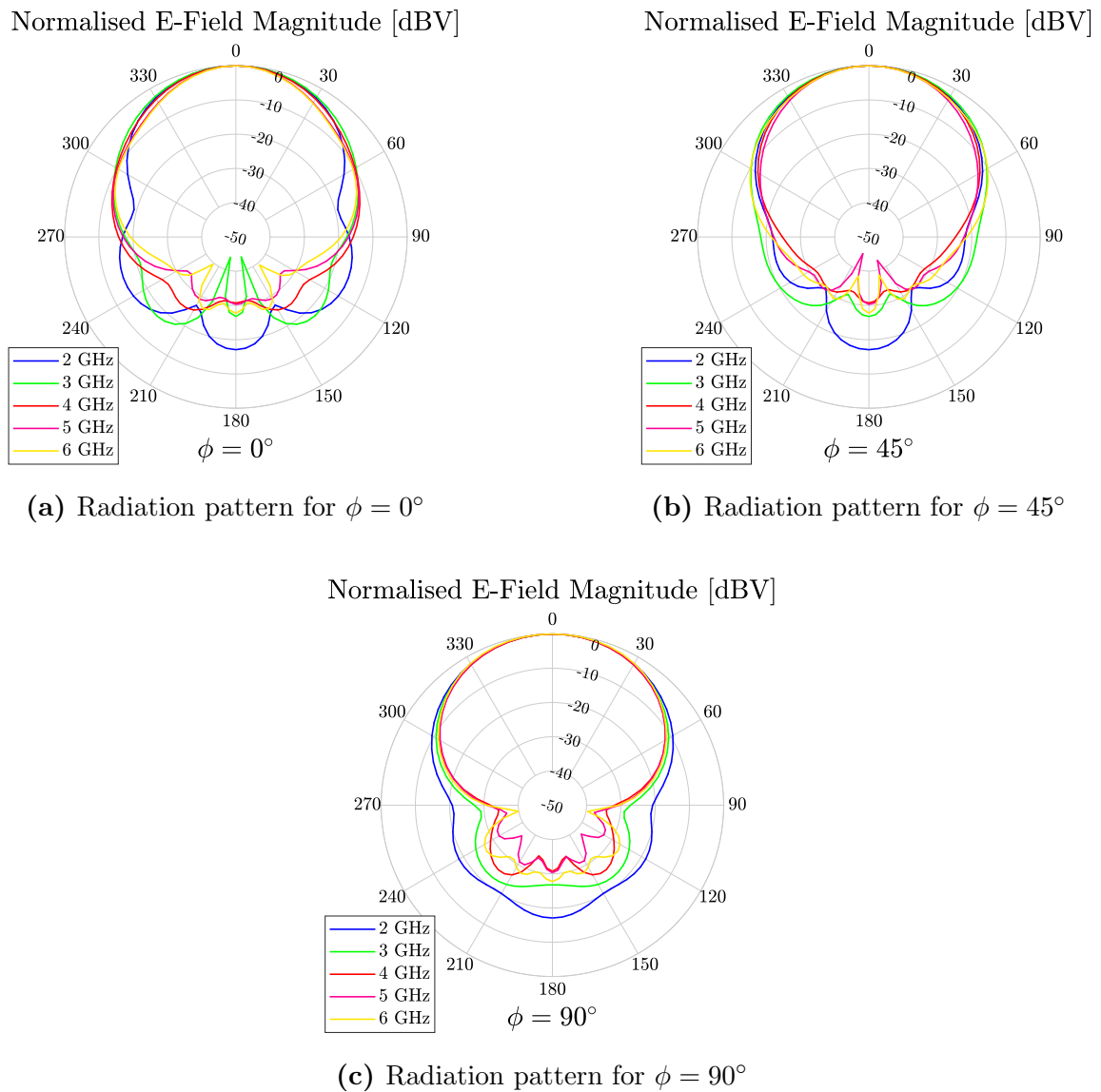


Figure 4.3: The total E-Field of the base pyramidal sinuous antenna, showing rotational symmetry.

Base model modification

With the base models' performance established, its feeding region was modified with pins. The pins were designed by using (2.8) to give a differential impedance 300Ω . With this information, it is found that by choosing the pins' diameter as 0.5 mm and $\epsilon_r = 1$, the distance between their centres should be 3.1 mm (this refers to the antenna's feeding region, shown in Fig. 4.1). The ground plane of the antenna was from a Rogers4003C substrate. This substrate of thickness 1.5 mm will simultaneously be used as a ground for both the antenna and its matching network. An isometric view of the antenna is displayed in Fig. 4.4, alongside the bottom view to show its matching network. The 8 cyan coloured cylindrical structures in the ground plane represents nylon screws that will hold the styrofoam blocks in place. The diameter of each nylon screw is 3 mm , with 2 screws being adjacent to each microstrip line.

To design the matching network, the point at which each arm's pin exits the substrate was extended with a quasi-microstrip line. The reason that this small portion is not a

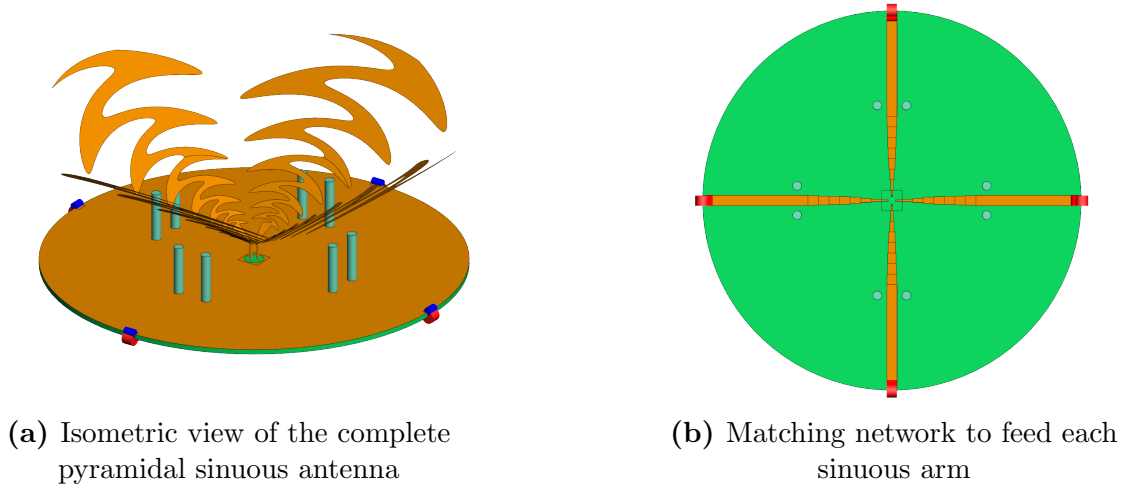


Figure 4.4: Complete pyramidal sinuous antenna with matching network.

true microstrip line is due to the absence of a ground plane directly above it, making it a floating line. However, its total length is less than $1/20$ of the wavelength at 6 GHz, thus any effects of the floating line would be minimised. It was at the end of this line where 150Ω edge ports were attached for each arm, and the 4-port S-parameters of the antenna was extracted via simulation. The S-parameters were then imported into AWR [38], and (2.20) was minimised by using a multi-section impedance transforming line. AWR's gradient optimisation method was used, with a source impedance set to 50Ω . The resultant length and width of each section is given in Table 4.2, starting with the line that has the highest impedance.

Table 4.2: Matching network parameters for base pyramidal sinuous antenna

Section Number	Width	Length
1	0.8 mm	3.60 mm
2	1.4 mm	3.60 mm
3	2.2 mm	3.60 mm
4	2.6 mm	3.60 mm
5	2.8 mm	3.60 mm
6	3.0 mm	3.60 mm
7	3.3 mm	3.60 mm
8	3.5 mm	36.0 mm

The differential reflection coefficient that resulted from this matching network can be found in Fig. 4.5. The magnitude remains below -10 dB for the majority of the band. Port 2 performs slightly worse at 5.25 GHz, and from the smith chart, it shows that port 2 is also more capacitive than port 1. The reason for the differences could be that 4 edge ports were used in simulation instead of waveguide ports. The opposing edge ports reflection coefficients were then averaged to give the result as a single port (summing both signals and halving the result). A waveguide port would provide more accuracy when applied to an SMA (Sub-miniature Version A) connector model. However, the result was still considered acceptable given the similarities between both ports with a maximum difference of around 1 dB at the peaks. The total E-field of the modified antenna remained similar to the base model and can be found in Fig. 4.6.

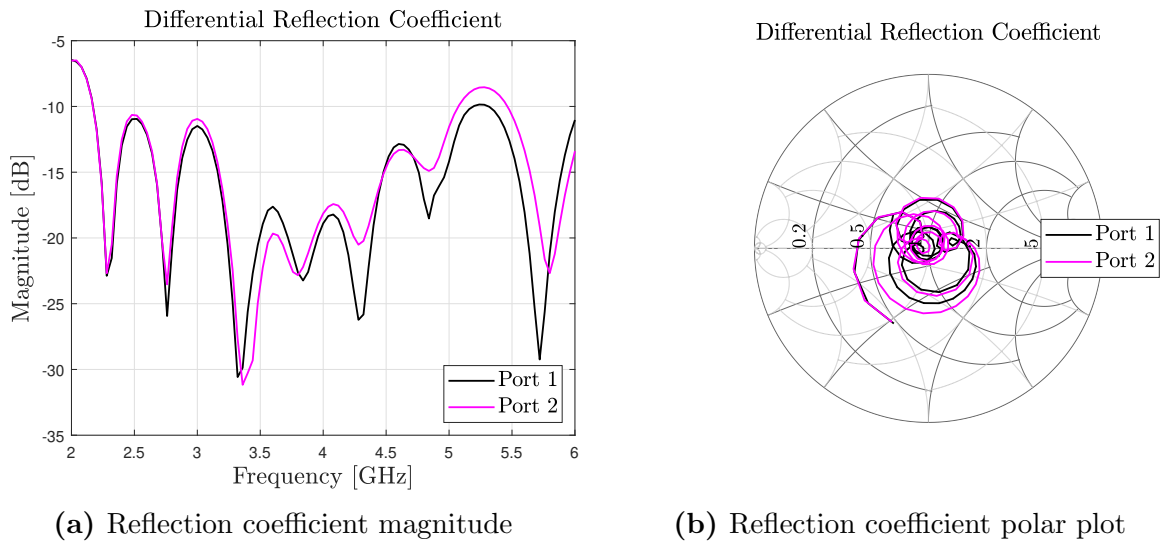


Figure 4.5: Modified pyramidal sinuous antenna simulated reflection coefficient

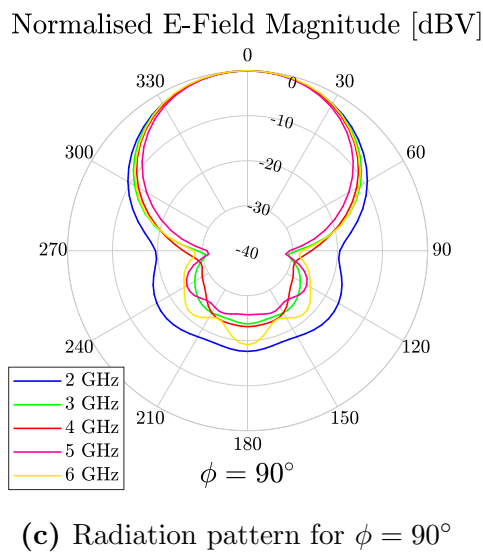
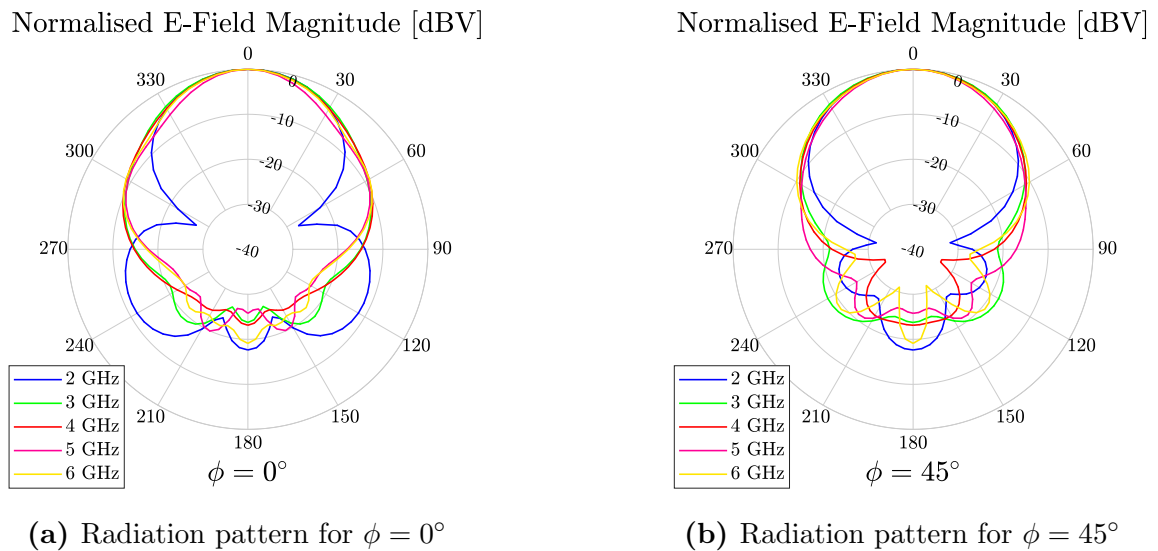


Figure 4.6: The total E-Field of the modified pyramidal sinuous antenna.

4.1.2 Fabrication and Measurements

The modified base pyramidal sinuous antenna was fabricated according to the parameters given in Tables 4.1 and 4.2. The sinuous arms were laser cut from a thin tin material. Four styrofoam blocks were cut into appropriate shapes to support the sinuous arms, with two nylon screws holding each styrofoam block in place. The arms were then taped onto the styrofoam blocks to ensure that they stayed in place. The completed antenna is shown in Fig. 4.7.

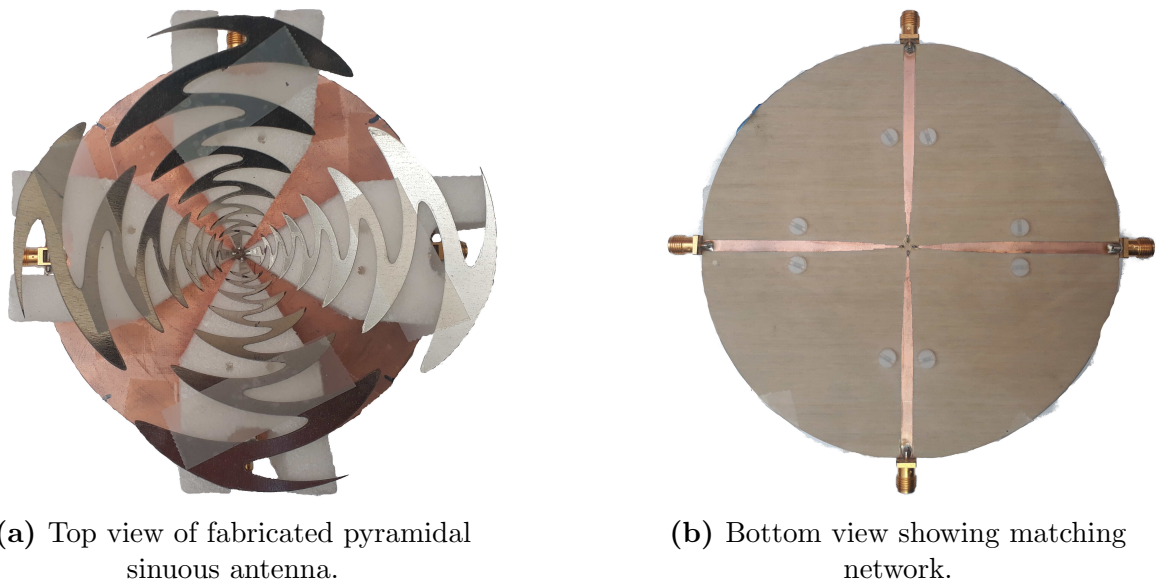
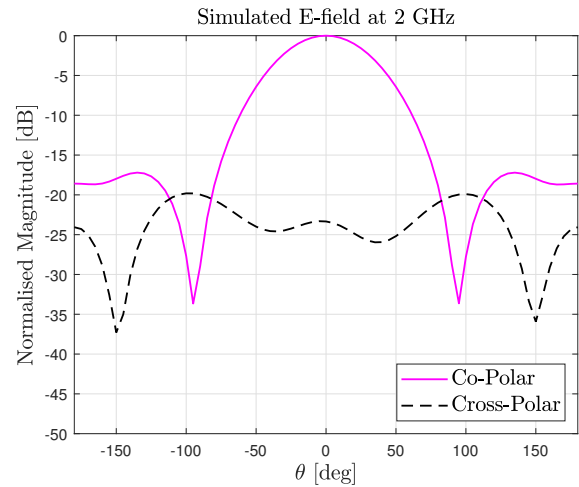
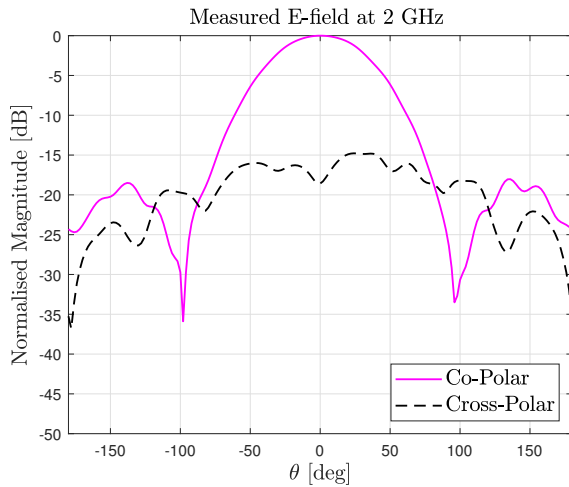


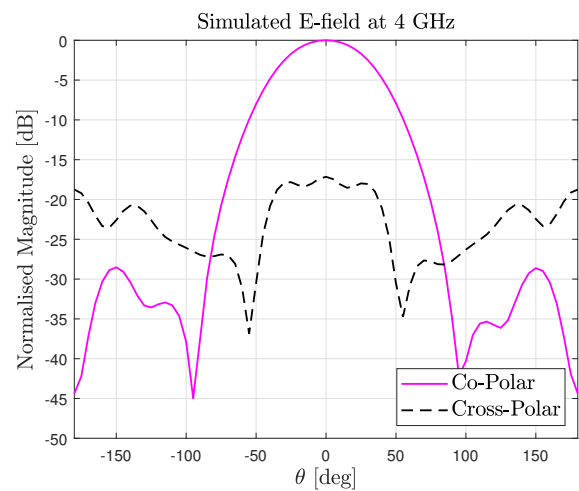
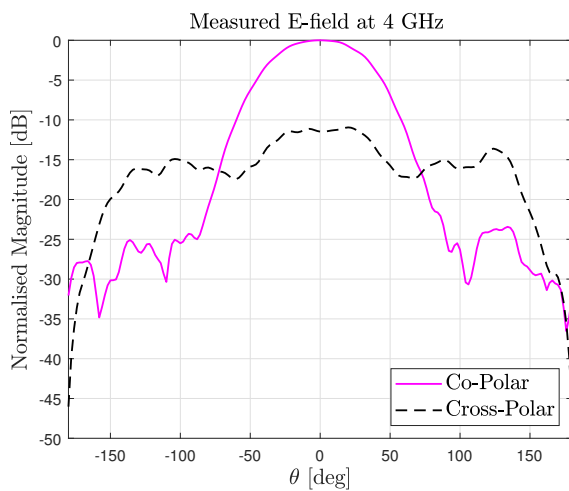
Figure 4.7: Fabricated, substrate free pyramidal sinuous antenna.

After construction, the antenna's radiation pattern was measured in an anechoic chamber using the measurement method described in section 2.2.3. This method only allows for the measurement of one polarisation at a time, and thus only one polarisation is shown in Fig. 4.8. Thus, only the E-field in the E-plane is shown. Furthermore, instead of polar coordinates, the measurement is plotted in rectangular coordinates to show the result clearly. The co and cross-polar components are both normalised to the co-polar component. For a fair comparison between the measured and simulated results, the antenna was set up similarly in FEKO to produce only one polarisation. The results in FEKO were also normalised to the fields' co-polar component. In comparison, the measured and simulated results are in agreement, indicating the fabrication process was accurate. The high wide angle cross polarisation levels in simulation can be reduced with a larger ground plane. The reflection coefficient of the antenna was measured according to the description given in section 2.2.3. The reflection coefficient can be found in Fig. 4.9. When compared to the simulation, the measured reflection coefficient matches up well. As mentioned in the previous section, both differential ports have the same response across the band. However, the fabricated model performs slightly worse at the 2.5 GHz region. The performance at this region can be attributed to the simulated model being excited by the less accurate edge ports. An excitation with waveguide ports may have highlighted this region as an area for a more optimised matching network before fabrication. However, the reflection coefficient remains below -10 dB for most of the band, which is an acceptable result.



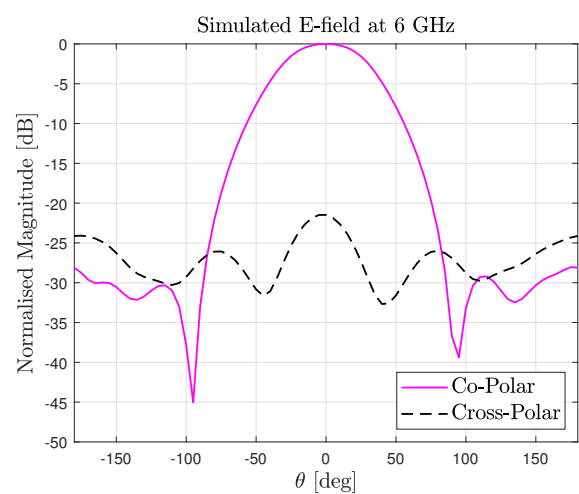
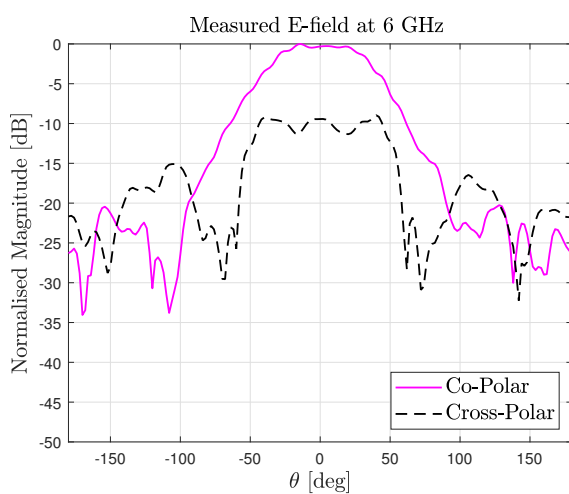
(a) Measured E-field in the E-plane at 2 GHz

(b) Simulated E-field in the E-plane at 2 GHz



(c) Measured E-field in the E-plane at 4 GHz

(d) Simulated E-field in the E-plane at 4 GHz



(e) Measured E-field in the E-plane at 6 GHz

(f) Simulated E-field in the E-plane at 6 GHz

Figure 4.8: Comparison of the measured and simulated E-field for the modified base model at 2 GHz, 4 GHz, and 6 GHz.

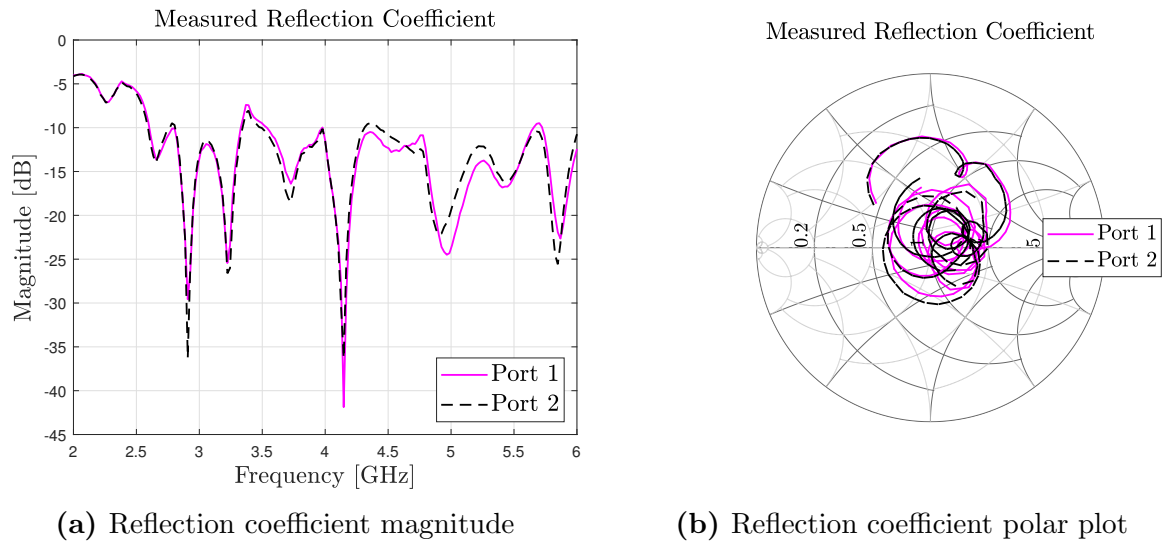


Figure 4.9: Modified pyramidal sinuous antenna measured reflection coefficient.

Feasibility

From a fabrication perspective, there were some difficulties in the construction of the sinuous antenna without any substrate on its arms. The first note is the feeding region in Fig. 4.1. There was difficulty in aligning the height of each arm to exactly 5 mm due to the angle at which the pins intersect with the arm. A suggestion was that a small part of the tapered region of the arm is bent to the angle ψ . This will make the fabrication process easier in terms of giving each arm the same height above ground. To facilitate this, the new laser cut arms will be made of a thicker brass or tin material. Secondly, the distance between the pins was too close. Special precautions had to be taken to ensure that the arms aren't shorted together during measurements. Lastly, to make the antenna more robust, the arms will be glued to the styrofoam. All of these adjustments will be explored in the following sections.

4.2 Two-arm Balun Integration

Before integrating the Marchand balun with the four-arm sinuous antenna, it is first tested with a two-arm antenna. Doing this ensures that compatibility is established beforehand. Another advantage of addressing the two-arm antenna first is simulation time, which allows for faster troubleshooting. The changes that were suggested in the previous section will be included in the FEKO model. The two important changes that were included in the FEKO model are: Bending the arm at the tapered region and an increased distance between the pins. It should also be noted that the Marchand balun was optimised for a 300 Ω load, not including any input reactance from the antenna. Thus, the goal is to match the performance found by [10], where the balun was connected directly to the sinuous arms, as discussed in Chapter 3.

4.2.1 Design and Simulation

To match the Marchand baluns' 1.05-4.7 GHz band, the sinuous antennas parameters are updated and can be found in Table 4.3. From Fig. 4.10, the new two-arm feeding

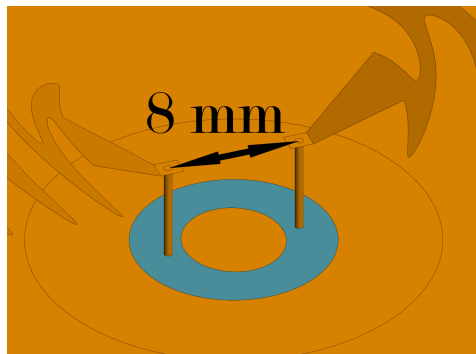
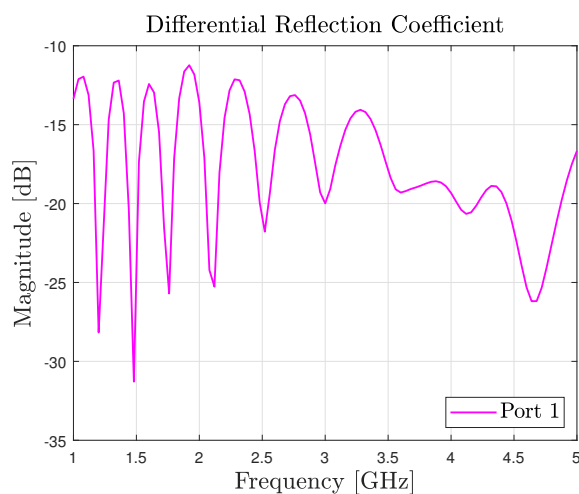


Figure 4.10: Two-arm feeding region, with new centre distance

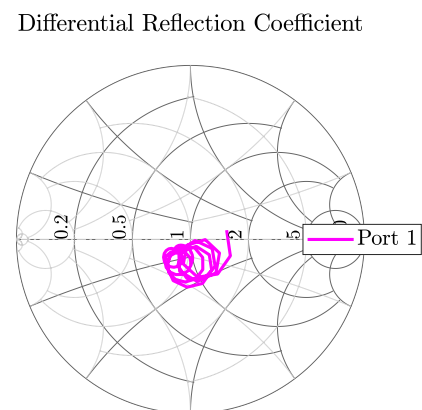
Table 4.3: Two-arm sinuous antenna design parameters

Parameter	Value
α	24.85°
δ	14.95°
τ	0.842
h	6 mm
ψ	33.52°
f_{min}	1 GHz
f_{max}	4.5 GHz

region is displayed, including the suggested changes to ease fabrication. This new model was tested with 300Ω edge port as a differential source and a Rogers4003C substrate. The new distance between the pin centres was chosen as 8 mm to provide adequate room for fabrication, which increased the impedance between the pins to 416Ω . The resulting reflection coefficient is shown in Fig. 4.11, indicating that the increased impedance as a result of the increased distance between the pins is acceptable. The radiation pattern is not plotted again as it remained similar to the simulated E-plane plots in Fig. 4.8, with the different frequency range accounted for.



(a) Reflection coefficient magnitude



(b) Reflection coefficient polar plot

Figure 4.11: Two-arm pyramidal sinuous antenna simulated reflection coefficient.

With the confirmation of the two-arm antenna's performance, the Marchand balun is simply integrated. The balun is attached to the 2 short lines that are connected to the point where the pins exit the substrate beneath the ground plane. The antenna and balun integration is shown in Fig. 4.12, where the white cylindrical object is made of styrofoam to support the arms at the height of 5 mm. For this model, a waveguide port is attached to the baluns' SMA connector. The simulation time and memory requirement increased due to the addition of the balun, styrofoam cylinder, and large substrate radius and thickness. Simulation times can be reduced by decreasing the memory requirement, which is 6.8 GB for the model in Fig. 4.12. If the substrates' radius is decreased, fewer mesh cells are

required, thus decreasing both the simulation time and memory requirement. To further aid simulation times, the triangle edge length has been changed to 1/10 (from 1/12) of a wavelength at the highest frequency. With these changes, the memory requirement was reduced to 1.7 GB, yielding reasonable simulation times.

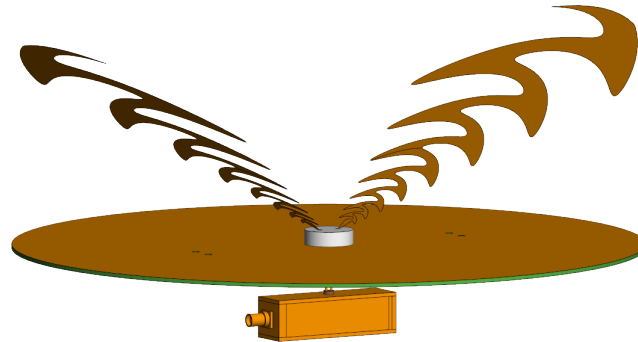


Figure 4.12: Two-arm sinuous antenna integrated with the Marchand balun.

The performance of the antenna was tested with two different substrates on the ground plane. The first is Rogers4003C substrate, the second being Rogers5880. Their relative permittivities are 3.38 and 2.2, respectively. It was suspected that the abrupt change in permittivity for the pins (from the substrate to free space or air) could affect the reflection coefficient, and the solution was to keep the substrates' permittivity as close to 1 as possible. The reflection coefficient results are shown in Fig. 4.13, which confirms that the substrate with the lower permittivity performs better. The Rogers4003C substrate performs marginally better at 1.6 GHz, however, the Rogers5880 shows a significant improvement around the 4 GHz region. These performances match what is found in Fig. 3.14.

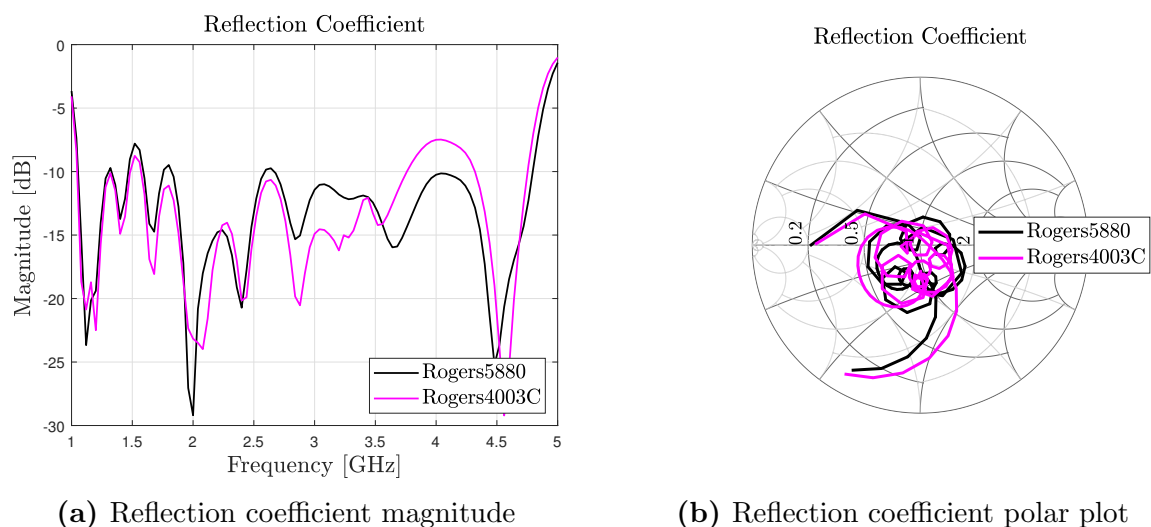


Figure 4.13: Two-arm antenna and balun integrated simulated reflection coefficient.

The radiation pattern of the version with the Rogers4003C substrate is shown in Fig. 4.14. The result is similar to the simulated and measured models in Fig. 4.8. The version with the Rogers5880 substrate is not shown because the patterns are similar. Now that it has been demonstrated that integrating the two-arm sinuous antenna with

the Marchand balun yields results similar to what was found in [10], the focus is shifted to the four-arm sinuous antenna in section 4.3.

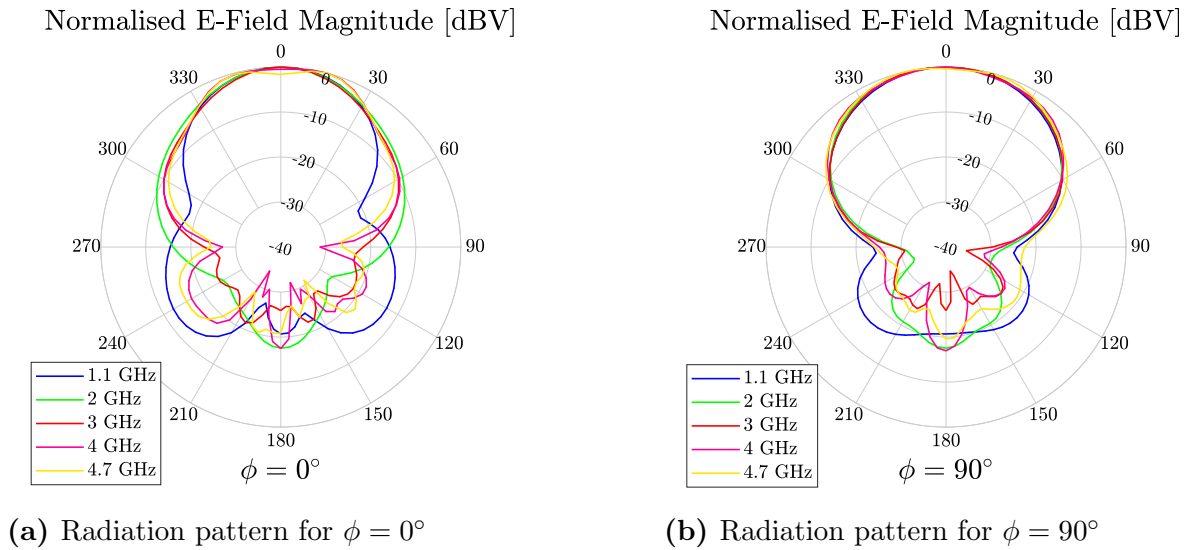


Figure 4.14: Simulated E-field of the two-arm sinuous antenna for the $\phi = 0^\circ$ and $\phi = 90^\circ$ cuts.

4.3 Four-arm Descrambling and Balun Integration

In order to connect two baluns to a four-arm sinuous antenna, a descrambling network is required. From the discussion in 2.1.2, a requirement for descrambling network is physical/electrical symmetry to ensure that the radiation patterns retain symmetry. This section presents an existing network in the literature alongside a new suggestion.

4.3.1 Descrambling Method Simulations

The first approach was to use the descrambling network described in [16]. The network can be seen in Fig. 4.15, and its purpose was to descramble microstrip baluns for planar

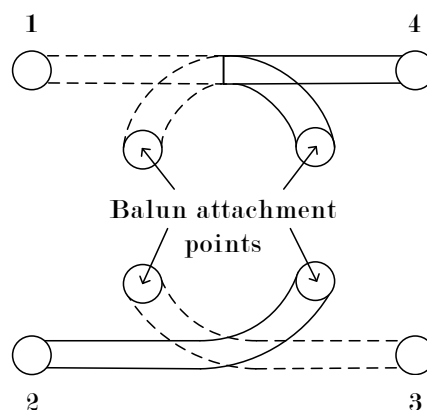


Figure 4.15: The descrambling approach described by [16] to feed planar sinuous antennas with microstrip balun.

sinuous antennas. The dashed lines represent the bottom layer of the substrate where diagonal opposing arms 1 and 3 can be connected by lines with an equal line length. The same applies to the solid lines that connected to arms 2 and 4, except that they represent the top layer of the substrate. The idea was that this approach is repurposed for the pyramidal sinuous antenna for use with the Marchand balun. The network was built in FEKO to run with a sinuous antenna with the same parameters as in Table 4.3, including all four arms. A top view of the implementation is shown in Fig. 4.16. The simulation was run with similar mesh settings as with the two-arm version. It should also be noted that at the time of manufacturing, the Rogers5880 substrate was not available in the departments' workshop, and thus the Rogers4003C substrate will be used from this point onward.

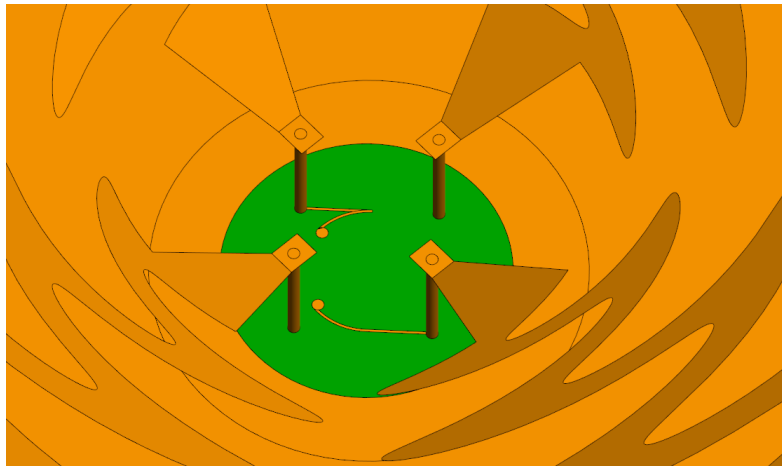
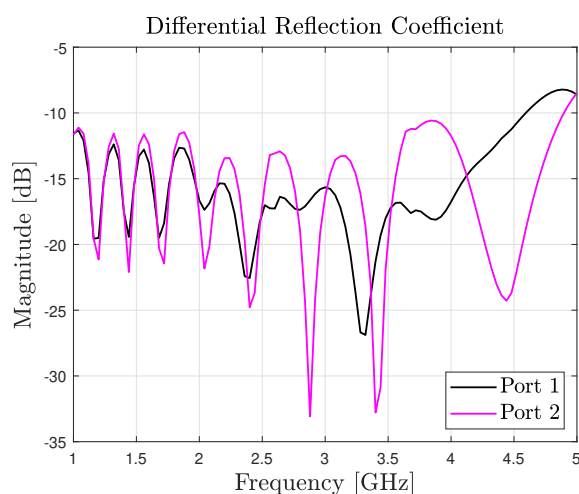
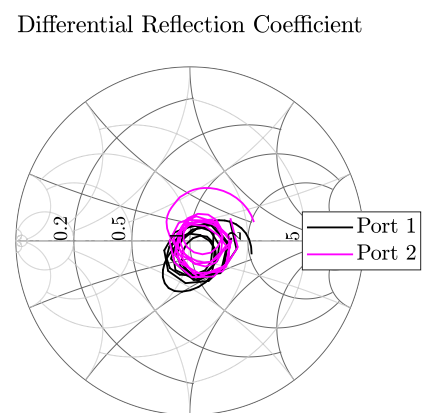


Figure 4.16: Implementation of the alternate descrambling method.

The reflection coefficient can be seen in Fig. 4.17. Ports 1 and 2's reflection coefficients aren't aligned at the higher frequencies due to the different electrical paths seen by each port. However, both ports reflection coefficients remain below -10 dB across the band.



(a) Reflection coefficient magnitude



(b) Reflection coefficient polar plot

Figure 4.17: Alternate descrambling approach: Reflection coefficient.

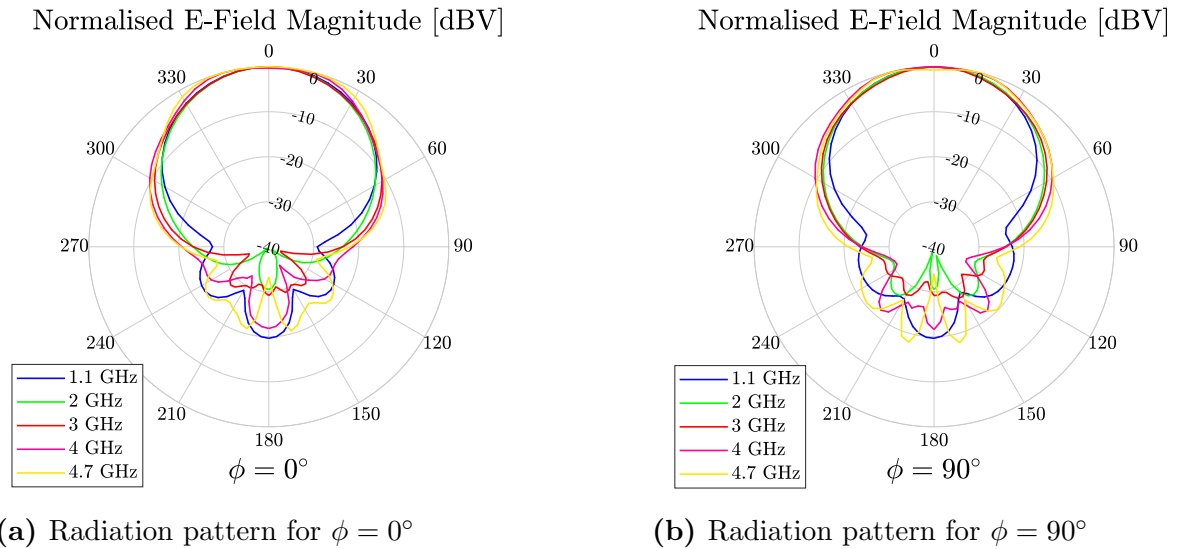


Figure 4.18: Simulated E-field with alternate descrambling network for the $\phi = 0^\circ$ and $\phi = 90^\circ$ cuts.

In Fig. 4.18 the polar plots for this descrambling method are shown, showing rotation symmetry is maintained. While the reflection coefficient and radiation patterns is a good result, it was realised that integration with the coaxial Marchand balun would be technically difficult to implement practically. The first reason is that the lines widths are 0.11 mm, which means that it could not be made in-house. The lines could be made thicker, but the nature of the lines going to arms 1 and 4 (Fig. 4.15) would introduce a shorter path for currents to follow than for arms 2 and 3. The balun attachment points are also of importance for two reasons. The first reason the spacing between the attachments pads is 3 mm, while the spacing between the twin output lines of the Marchand balun is 1.64 mm. The second reason is that the new centre to centre length between the pins supporting the arms is 8 mm. This implies that the balun attachment points would have to be less than 8 mm, introducing a cramped area to work in given the size of the balun outputs. While this approach works with the much narrower microstrip baluns, it would be difficult to implement with the coaxial Marchand balun.

New Descrambling Method

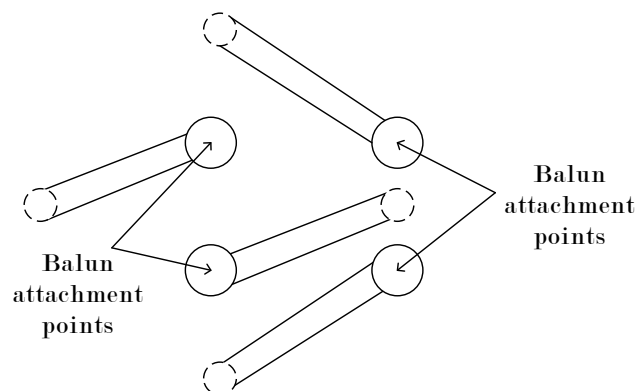


Figure 4.19: New suggested descrambling method.

A new descrambling method is shown in Fig. 4.19. This descrambling network was tailored for the coaxial Marchand balun described in section 3.3, and requires only one layer of a substrate. The balun attachment points are moved off-centre so that simple straight lines can be connected to the pins connecting the sinuous arms. The pins are shown as dashed circles. The spacing between the attachment pads is 1.64 mm to match the baluns' output twin lines. The line widths were chosen as 0.24 mm, which can be manufactured by the engineering departments workshop. The lines lengths from the attachment points to the pins are kept the same to preserve radiation pattern symmetry.

The antennas reflection coefficient for this implementation can be seen in Fig. 4.20 where the Rogers4003C substrate is used. While not as good as the result from the previous method, it reaches a maximum of -8.5 dB at 1.9 GHz and remains well below this value across most of the band. From the smith chart, the reason for its performance is clear, showing that the reflection coefficient as seen from the ports is relatively capacitive. Various attempts have been made to increase the inductance mechanically, such as decreasing line widths, increasing line lengths, narrowing of the sinuous arms by decreasing the rotation angle δ , and increasing pins lengths.

However, none of these attempts made any significant improvements when compared to the increased fabrication difficulty. The ground plane was then changed to the lower permittivity Rogers5880 substrate to reduce the total capacitance in the system. This change showed a significant improvement, however, the substrate was not available at the time of fabrication. The antennas reflection coefficient for the Rogers5880 substrate is shown in Fig. 4.21. For this substrate, the magnitude remains well below -10 dB across the band.

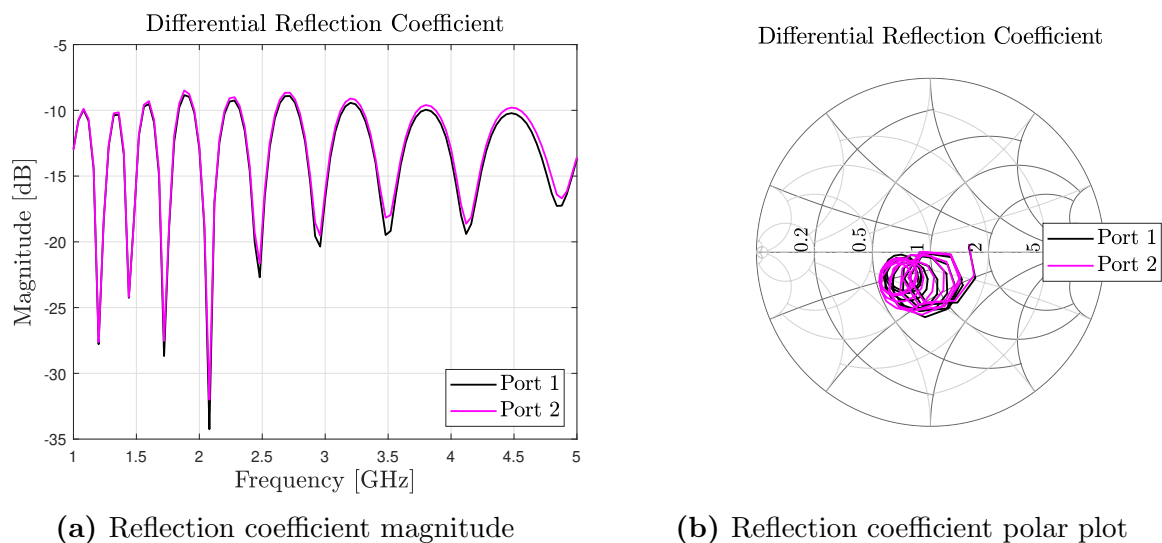


Figure 4.20: New descrambling method's with reflection coefficient for the Rogers4003C substrate.

For completeness, the new methods' radiation pattern is shown in Fig. 4.22. Both substrates have similar symmetrical patterns, thus only the Rogers4003C implementation is shown.

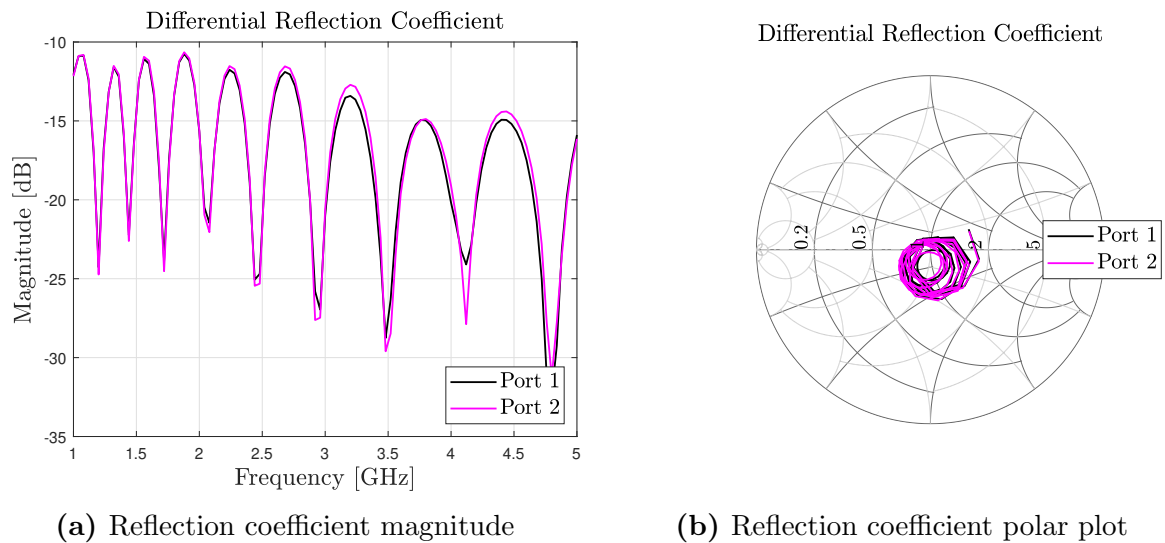


Figure 4.21: New descrambling method's reflection coefficient for the Rogers5880 substrate.

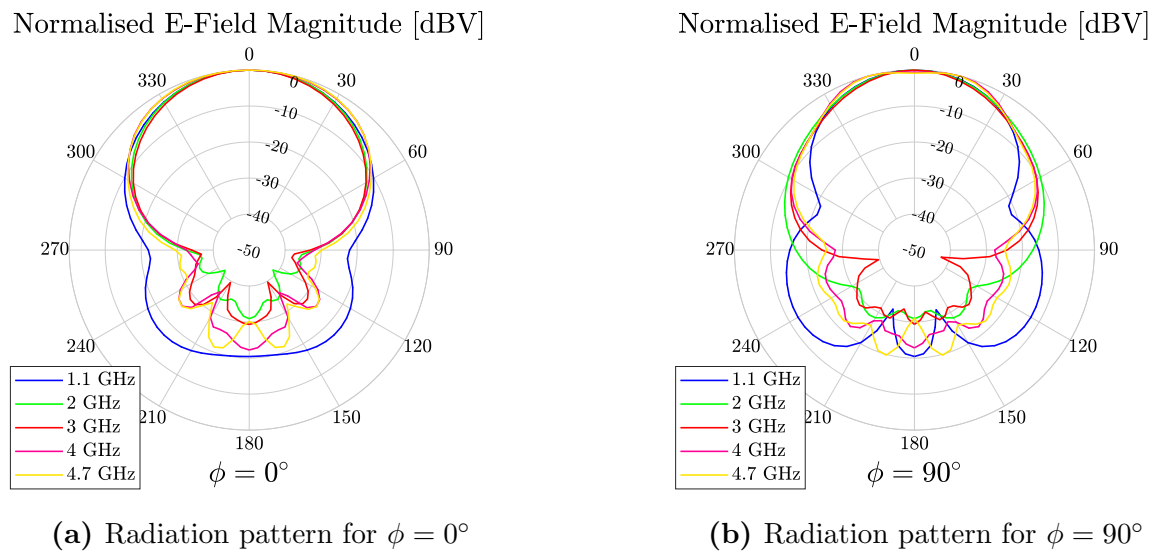


Figure 4.22: Simulated E-field for the new descrambling method.

4.3.2 Balun Integration

Having the performance of the sinuous antenna with the new descrambling method established, it is now tested with two coaxial Marchand baluns. Only the Rogers4003C substrate is covered in this section due to its availability and time constraints as a result of simulation times.

Simulations

The FEKO implementation is displayed in Fig. 4.23. For stability, the antennas' ground plane is rested on both baluns, where they would be glued to stay in place. For this simulation, including the whole substrate has a memory requirement of 13.773 GB. As before, the substrates' radius was decreased to reduce the memory requirement to 6.993 GB for a relatively faster simulation time.

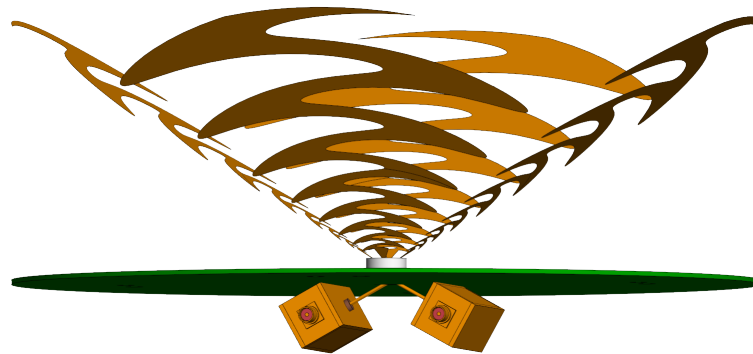


Figure 4.23: Four-arm sinuous antenna integrated with the Marchand balun.

The reflection coefficient of the antenna and balun integration is shown in Fig. 4.24. The first integration attempt used the Marchand balun as presented by [10]. However, this resulted in a reflection coefficient of -7 dB around the 3.9 GHz region. To improve this result, the total length of the baluns' twin lines was reduced from 25 mm to 23 mm. This length decrease shifted the 3.9 GHz regions' minimum (and therefore the total minimum) reflection coefficient to -7.5 dB. With this minimum, the four-arm implementation matches what was found in [10], meeting the goal in simulation. For an improved reflection coefficient, the Phelan balun is suggested and designed in Chapter 5.

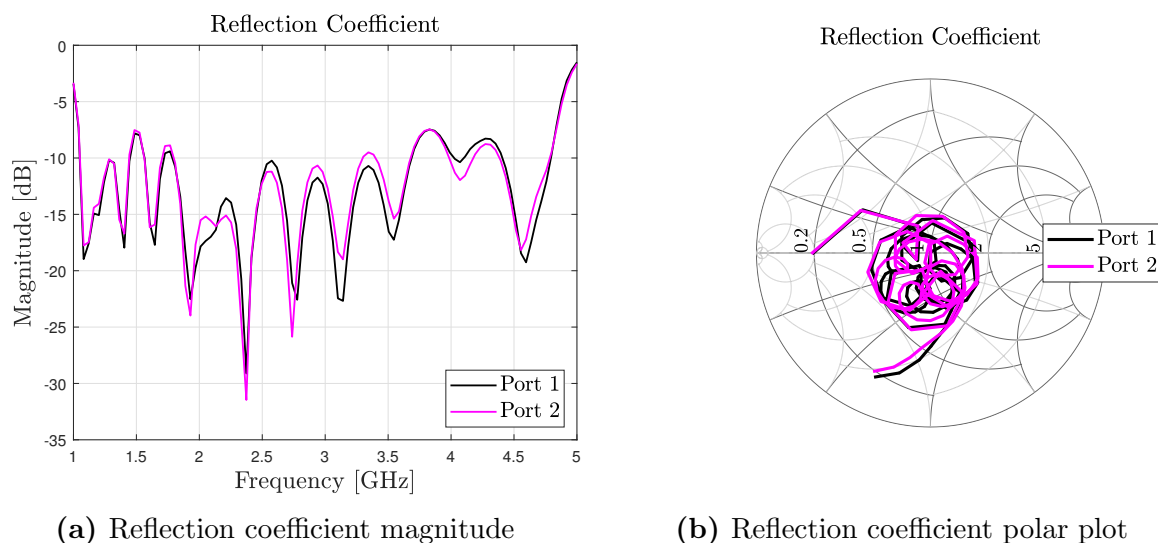


Figure 4.24: New descrambling method's reflection coefficient for the Rogers4003C substrate.

For structural integrity, metal strips were added to the low-frequency portion of the sinuous and directly connected to the ground plane as in Fig. 4.25. While this connection provides a direct pathway to the ground plane, most of the currents are either radiated or reflected by the sinuous geometry before the transition region is reached.

As a result, the effect on the antenna's performance is minimal. It should be noted that wider metal strips were tested, however, this interfered with the radiation pattern. The results of this final iteration of the four-arm sinuous antenna and balun integration is shown in Figs. 4.26 and 4.27.

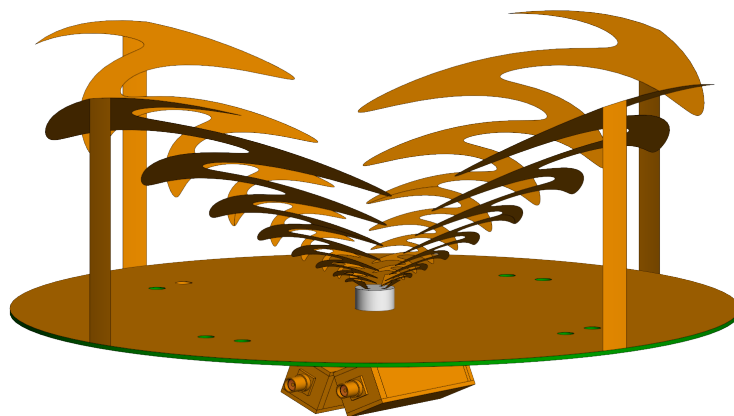


Figure 4.25: Four-arm sinuous antenna integrated with the Marchand balun, including metal strips to add structural integrity.

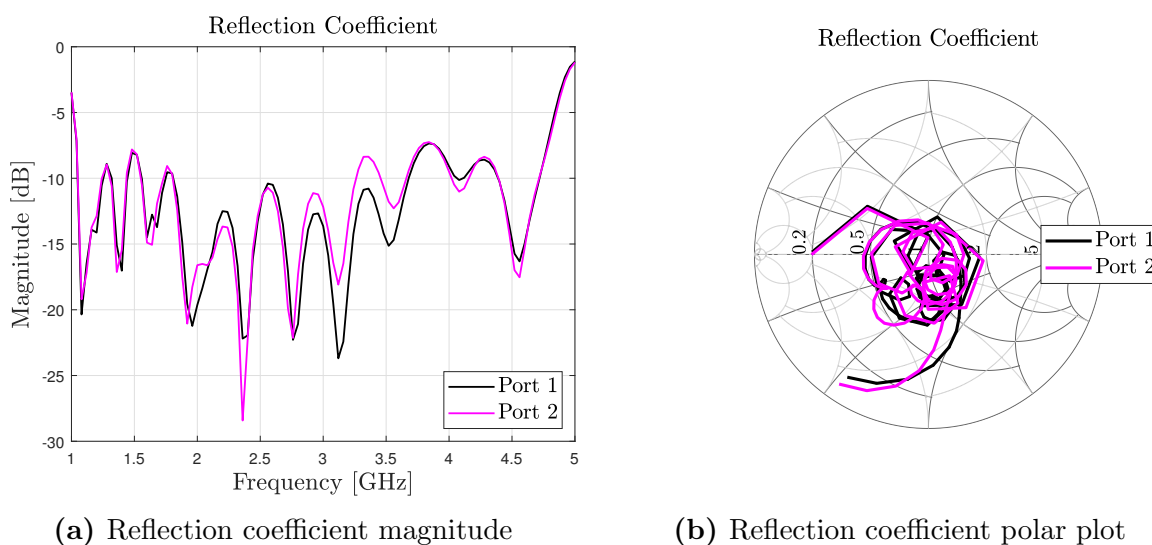


Figure 4.26: Final four-arm sinuous antenna with added structural support.

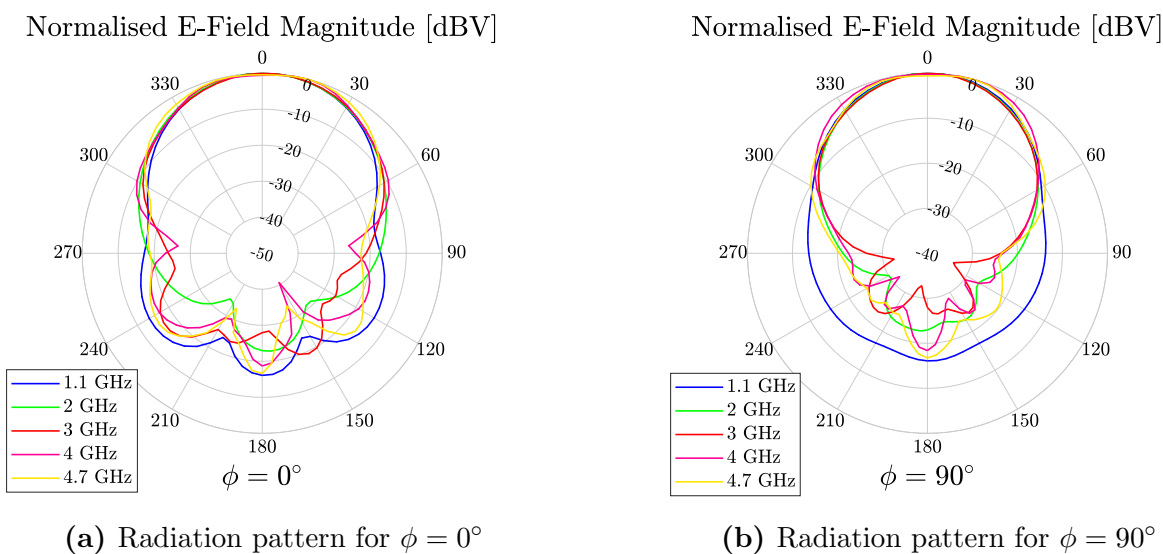
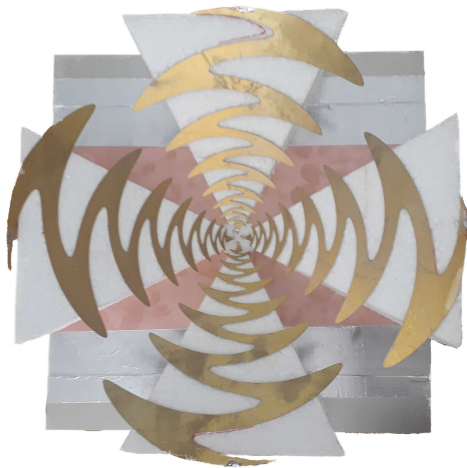


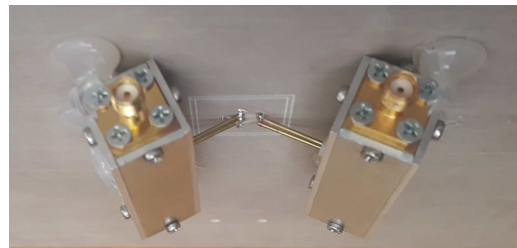
Figure 4.27: Simulated E-field of the four-arm sinuous antenna with added structural support.

Fabrication and Measurements

The fabricated antenna is displayed in Fig. 4.28. As before, the sinuous arms are held up by styrofoam cut-outs in the form of trapezoidal prisms. In addition, the metal strips are connected to ground for added stability. The total diameter of the circular ground plane in the simulations was 260 mm, which was too large to be milled. Instead, a smaller square was chosen as the ground plane, where the descrambling network was milled out on the bottom layer. To meet the total 260 mm diameter requirement, additional metal plates were taped to the sides of the ground plane. The two Marchand baluns were attached to the descrambling network as in Fig. 4.28b and was glued to stay in place. Overall, this version of the antenna is much more robust than the previous version in Fig. 4.7.

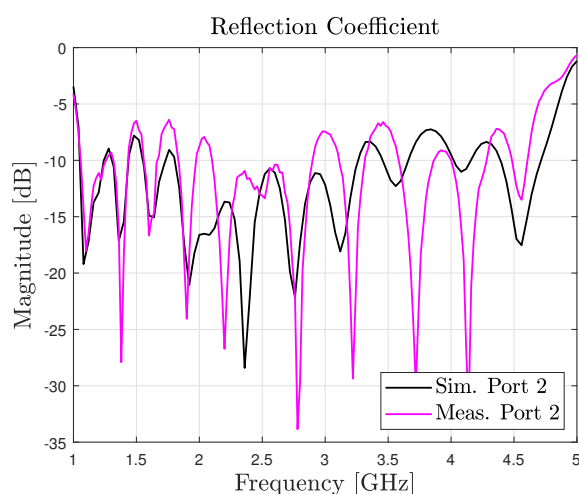


(a) Top view of four-arm pyramidal sinuous antenna

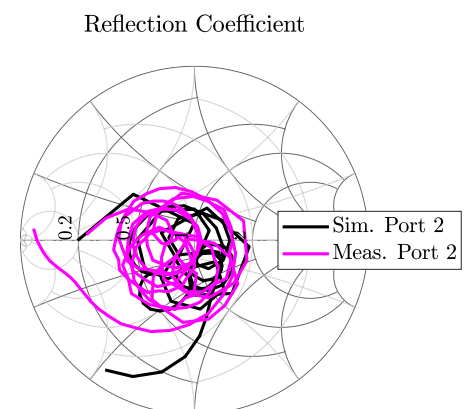


(b) Bottom view showing balun connection

Figure 4.28: Fabricated pyramidal sinuous antenna with Marchand balun integration. Here the baluns are attached to the descrambling attachment points and glued onto the Rogers4003C substrate.



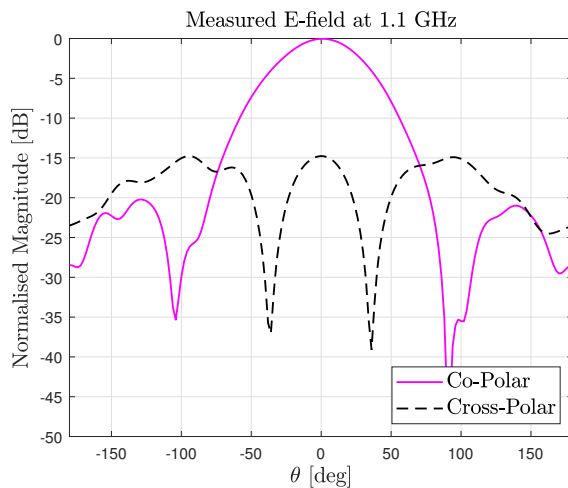
(a) Reflection coefficient magnitude



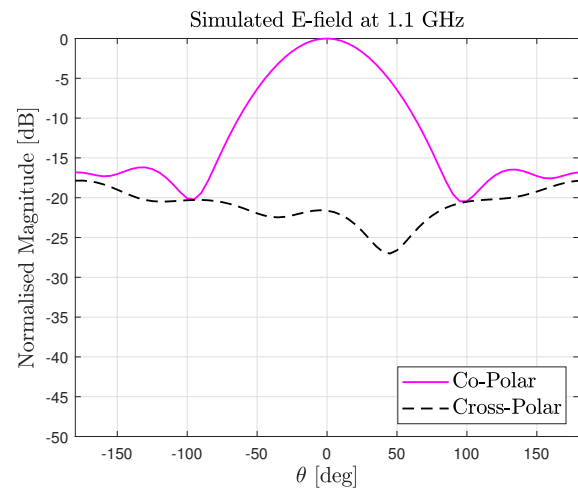
(b) Reflection coefficient polar plot

Figure 4.29: Measured reflection coefficient of the four-arm sinuous antenna.

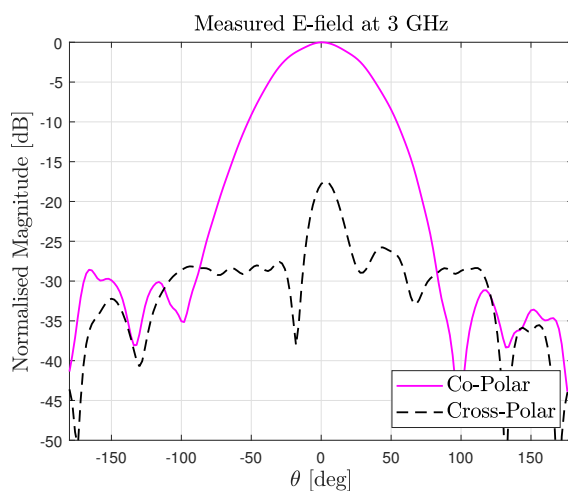
The reflection coefficient is compared to the simulation in Fig. 4.29. It should be noted that when port 1 was torqued for measurement with the VNA, the descrambling traces for port 1 tore away from the ground plane. There was an attempt to fix the traces with bond wires, however, this did not work. The matter was not pursued further in order to preserve port 2's integrity. Hence, only port 2's result is shown. At the lower frequencies (1-2 GHz range) the measured result seems to follow the simulation, with a 1-2 dB difference at the peaks. In the 2-4.7 GHz range, the measured result seems to be a shifted version of the simulation, where there are more significant differences between peaks. The reason for this can be seen in Fig. 4.29b. Generally, the measured complex impedance seen at the baluns' input port is less concentrated around unity when compared to the simulated complex impedance. As mentioned before, the Marchand balun was optimised for a 300 Ω load, which excluded any antenna reactance as seen from the input. In Chapter 5, it is found that a parallel-connected balun reduces the load impedance seen by the input by a factor of 4. A parallel connected balun is therefore suggested as an improvement for integration with the sinuous antenna. The antennas' radiation pattern is shown in Fig. 4.30 for 1.1 GHz, 3 GHz and 4.7 GHz. As before, the co- and cross-polar fields of both the simulated and measured results were normalised to the co-polar fields.



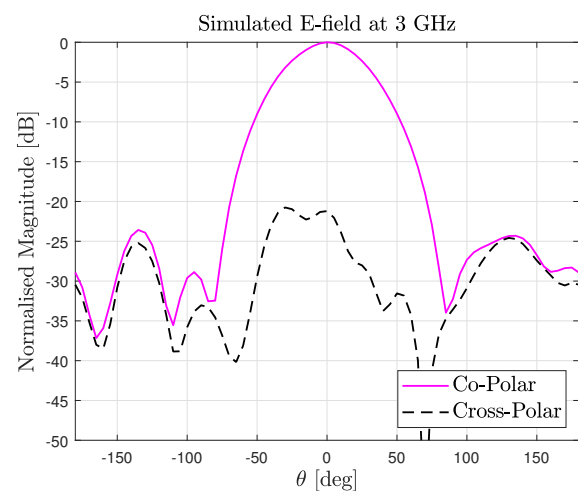
(a) Measured E-field in the E-plane at 1.1 GHz



(b) Simulated E-field in the E-plane at 1.1 GHz



(c) Measured E-field in the E-plane at 3 GHz



(d) Simulated E-field in the E-plane at 3 GHz

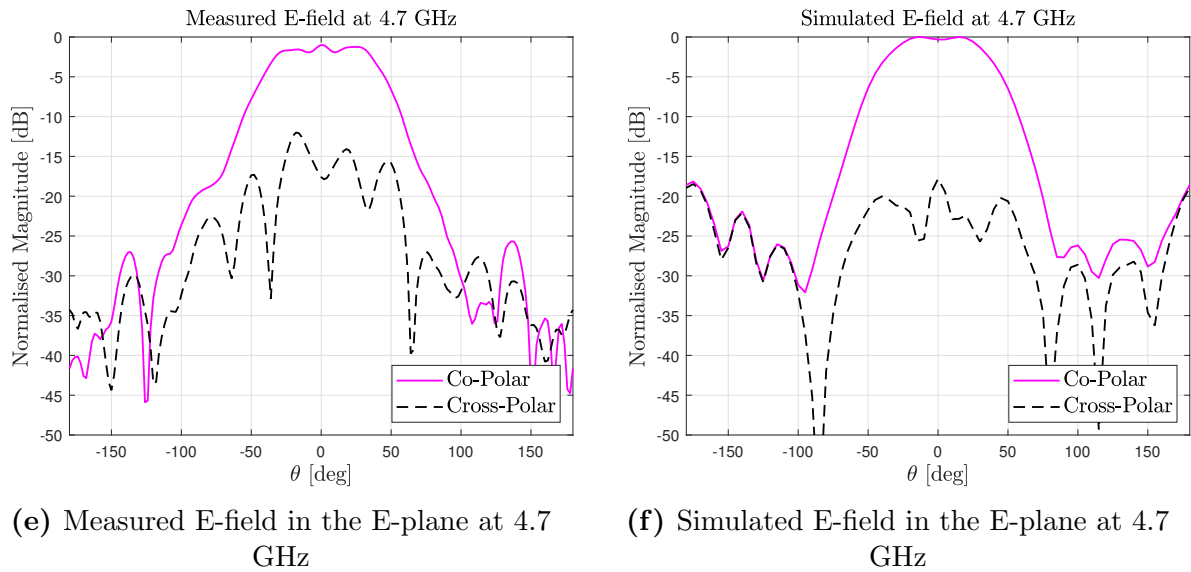


Figure 4.30: Comparison of the measured and simulated E-field for the completed sinuous antenna at 1.1 GHz, 3 GHz, and 4.7 GHz.

From the results, it is clear that the antenna retains a constant pattern. The simulated results have slightly higher sidelobes due to the currents on the baluns. The reason why the side lobes are not similar to the measured results is because of the much larger, square ground plane that was used for the manufactured antenna. By the measure of η_{BOR_1} , rotational symmetry is confirmed for the simulated results in the following section.

4.4 Efficiency as a Feed for the SKA Shaped Dish

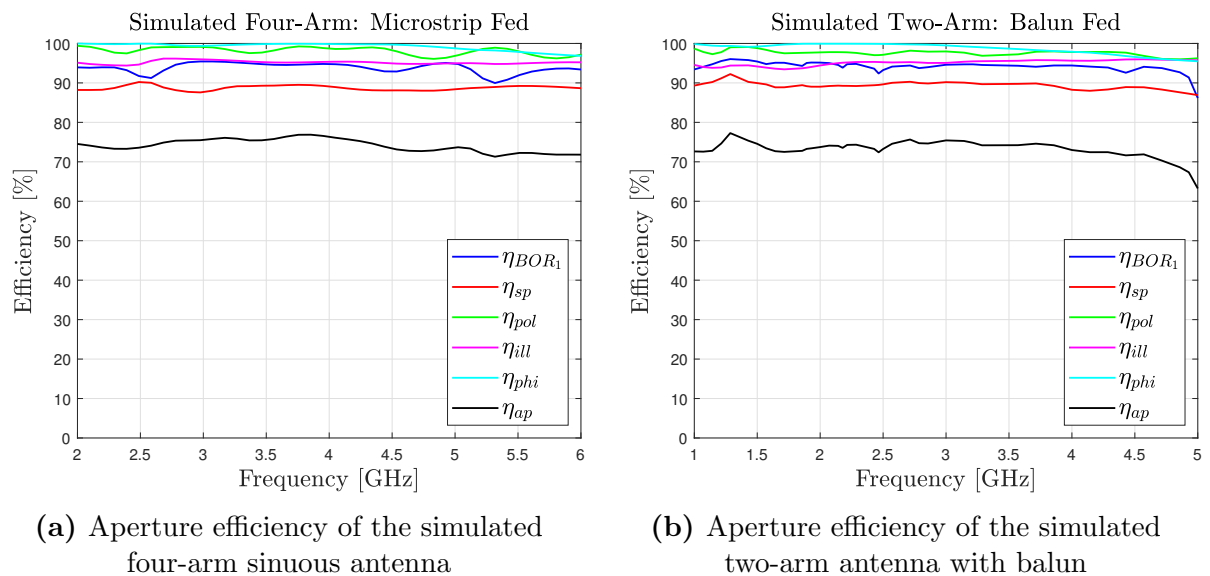


Figure 4.31: Efficiencies of the simulated four-arm microstrip fed and the two-arm balun integrated antennas.

In this section, the efficiency of the sinuous antennas as a reflector feed by using the simulation results only. As mentioned in section 2.3, the reflector of interest is the SKA shaped offset Gregorian reflector.

In Fig. 4.31 the BOR_1 efficiency confirms the rotational symmetry of both antennas, remaining above 90% across their respective bands. Overall, the aperture efficiency also shows a good result, staying above 70%. This indicates that both antennas could have relatively high efficiencies if they are to be used as a reflector feed. It should be noted that only one polarisation is shown for the four-arm antenna. Next, the simulated efficiencies of the final antenna and balun integration are shown in Fig. 4.32. The efficiencies for the antenna that is fed by the Marchand balun retains the efficiency of the earlier antennas across the band.

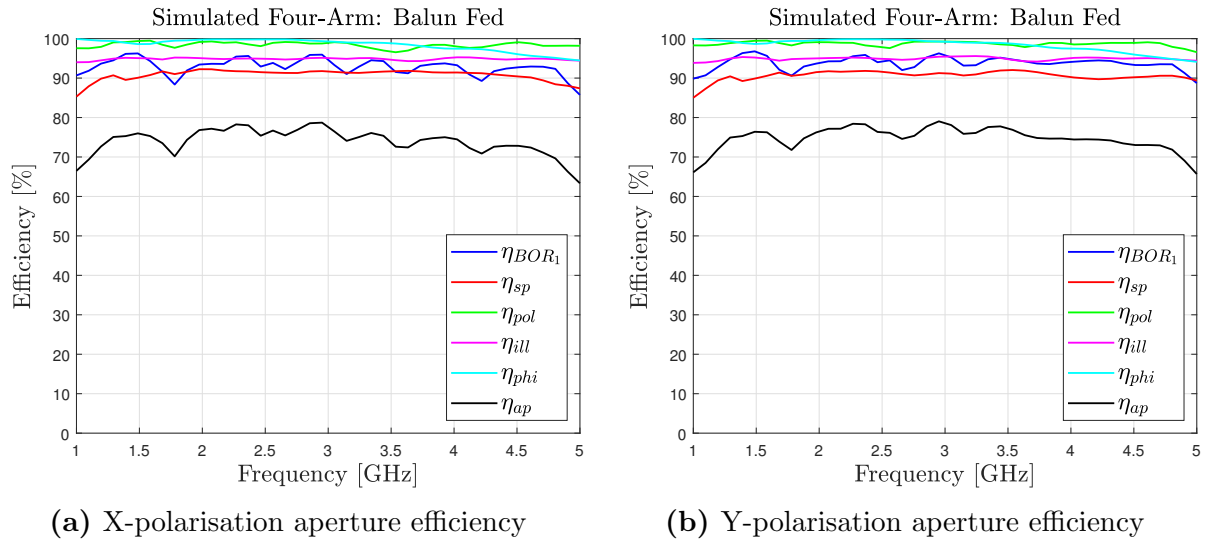


Figure 4.32: Efficiencies of the simulated four-arm final four-arm antenna, balun integrated.

The results show these antennas, specifically the balun fed antennas, have a relatively high-efficiency potential when used as a reflector feed. The aperture efficiency performance limit of this reflector system is investigated in [39] for the SKA band 1 and 2, 0.35-1.05 GHz and 0.95-1.76 GHz, respectively. While the band of the antennas in this thesis is not identical to band 1 and 2, the reported aperture efficiency limit in the 1.055-1.76 GHz range is between 90-92%. The theoretical limit is shown to provide an idea of what is possible in theory. As a comparison, the aperture efficiency found in [9] is around 65% for MeerKAT for 3:1 bandwidth. Although the comparison here is between two different reflectors (MeerKAT and a shaped offset Gregorian reflector), it is with the same antenna over a wider 4.5:1 band. As mentioned before, the antenna's frequency independence allows it to be scaled in physical size (and therefore frequency) to match the SKA's bands of interest across a 4.5:1 band if desired. The frequency ranges chosen here was for manufacturing convenience (in terms of the physical size of the antenna).

4.5 Chapter Summary

Firstly, the chapter starts by investigating the feasibility of manufacturing a sinuous antenna without a substrate on its arms. The reason for this investigation is to avoid exciting surface waves which can affect wideband performance. It is found that the differential reflection coefficient and antenna patterns for the manufactured antenna closely resemble the simulated version. From this build, some improvements are suggested for the next antenna that will integrate the Marchand balun to ease construction. Secondly, a two-arm version incorporating only one Marchand balun is implemented in simulation, including the improvement suggestions from that resulted from the previous version. The simulation confirmed compatibility with the Marchand balun. It was also found that an improved reflection can be found with low permittivity substrates. Thirdly, for the four-arm implementation, a descrambling network was designed and compared to an existing network in the literature. The results showed that both networks' reflection coefficients remained below -10 dB. However, the version in the literature was technically difficult to implement due to the double substrate layer requirement (Top and bottom layer). As a consequence of requiring two layers, the electrical path is different for both ports which yielded differing reflection coefficients for both ports. The "new" suggested descrambling network requires a single layer, reduces complexity, and yields a similar reflection coefficient for both ports. Using this network to implement the four-arm antenna showed simulation results consistent with what was found in previous work of a direct two-arm balun integration. The antenna patterns of the manufactured antenna remained similar to the simulated version. This confirmed the descrambling network and the Marchand baluns' amplitude and phase unbalance performance. The manufactured version had a higher reflection coefficient when compared to the simulated antenna. As a result, a Phe-lan balun is investigated in Chapter 5 as a candidate replacement due to its inherent 4:1 impedance transformation. Lastly, the subject antenna of each section is tested as a reflector feed for the SKA's offset Gregorian reflector. The resulted in each antenna yielding an excellent aperture efficiency of above 70 % in their bands of interest. The BOR_1 efficiency is also calculated here which was above 90%, confirming each antennas rotational symmetry.

Chapter 5

Phelan Balun Design

In Chapter 4 it was shown that integrating the sinuous antenna with the Marchand balun yielded acceptable results in simulation. However, the reflection coefficient could be improved upon. It was therefore decided that the Phelan balun could be a candidate for integration. In this Chapter, the Phelan balun is investigated as a possible feed for the sinuous antenna. The first section (5.1) is focussed on the mathematical derivation of the design equations of the Phelan balun. Section 5.2 follows the design of a suitable Phelan balun that could feed the sinuous antenna. The simulation and measured results are shown here as well. Lastly, section 5.2.1 shows the simulation results of other parallel-connected baluns that would allow for simpler integration with the sinuous antenna.

5.1 Phelan Balun Theory

In this section, an expression for the bandwidth capability of both series and parallel-connected, uncompensated baluns is derived. An example of an uncompensated balun is the folded balun as depicted in Fig. 3.3. The term “uncompensated balun” generally refers to a balun without an additional shunted, open-circuited stub to compensate for the reactance of a shorted transmission line. The term “series-connected/parallel-connected” simply refers to whether the load has series or parallel topology. This idea is shown in Fig. 5.1. An example of a compensated balun is a Marchand/Roberts balun in Fig. 3.5a. As per the definition, the Roberts balun is similar in structure to the folded balun, except for the added open-circuited stub, which in turn yields a wider bandwidth. Phelan [34] showed that parallel-connected, uncompensated baluns have an inherent 4:1 impedance transformation, which is ideal for the sinuous antennas’ high input impedance.

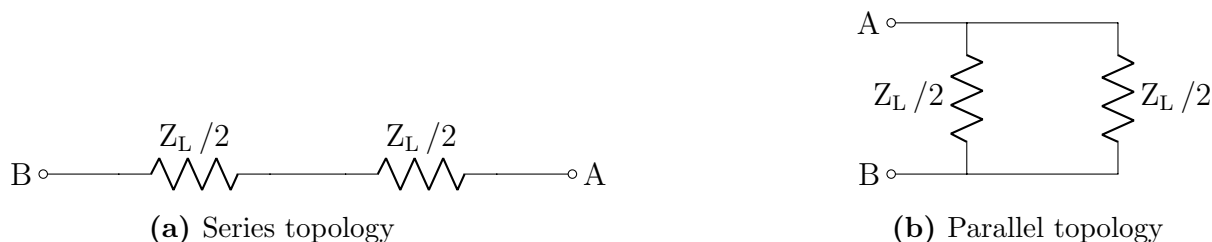


Figure 5.1: Series and parallel load topology.

5.1.1 Analysis

The Phelan balun analysis starts with a simplified equivalent circuit of an uncompensated, resonant balun as in Fig. 5.2. Due to the resonance of the balun, the load is placed in parallel with a resonant cavity impedance. This starting point applies to both series and parallel-connected baluns, and for that reason, the load topology is introduced at the end of the derivation.

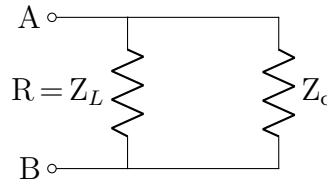


Figure 5.2: Uncompensated, resonant balun equivalent circuit.

First assuming a real load impedance and that $R = Z_L$, the equivalent input impedance as seen across nodes A and B can be written simply:

$$Z_{\text{in}} = \frac{Z_L Z_c}{Z_L + Z_c}, Z_c = j Z_e \tan(\beta l) = j X_c. \quad (5.1)$$

Here Z_c is the cavity impedance and Z_e is defined as the effective resonant line characteristic impedance, with $l = \lambda_0/4$, where λ_0 is the wavelength at the band centre frequency and β is the propagation constant. Given that Z_{in} is a complex number, it is simplified into its real and imaginary components as

$$Z_{\text{in}} = \frac{Z_L X_c^2}{Z_L^2 + X_c^2} + j \frac{Z_L^2 X_c}{Z_L^2 + X_c^2} \quad (5.2)$$

with its components written as $R_{\text{in}} = \text{Re}(Z_{\text{in}})$ and $X_{\text{in}} = \text{Im}(Z_{\text{in}})$. These components can be normalised to the load impedance Z_L resulting in:

$$R_n = R_{\text{in}} / Z_L = \frac{Z_e^2 \tan^2(\beta l)}{Z_L^2 + Z_e^2 \tan^2(\beta l)} = \frac{\gamma^2 \tan^2(\beta l)}{1 + \gamma^2 \tan^2(\beta l)} \quad (5.3)$$

$$X_n = X_{\text{in}} / Z_L = \frac{Z_L Z_e \tan^2(\beta l)}{Z_L^2 + Z_e^2 \tan^2(\beta l)} = \frac{\gamma \tan^2(\beta l)}{1 + \gamma^2 \tan^2(\beta l)} \quad (5.4)$$

and simplifying

$$Z_n = R_n + j X_n \quad (5.5)$$

where $\gamma = Z_e / R = Z_e / Z_L$. Here it should be noted that the impedance bandwidth is proportional to γ . Next, from the normalised equations (5.3) and (5.4) the voltage reflection coefficient can be written as

$$\rho = \frac{Z_n - 1}{Z_n + 1} = \frac{R_n + j X_n - 1}{R_n + j X_n + 1} = \frac{R_n^2 + X_n^2 - 1}{(R_n + 1)^2 + X_n^2} + j \frac{2 X_n}{(R_n + 1)^2 + X_n^2}. \quad (5.6)$$

Now the VSWR can be calculated from its definition as in [21]

$$\sigma = \frac{1 + |\rho|}{1 - |\rho|} \quad (5.7)$$

Finally, when γ is made the subject of the formula of (5.7) with $\beta l = (2\pi/\lambda)(\lambda_0/4)$, then the result is

$$\gamma = \frac{\sqrt{\sigma}}{\sigma - 1} \cot\left(\frac{\pi}{B + 1}\right) \quad (5.8)$$

Equation 5.8 is plotted for different VSWR values in Fig. 5.3. This result shows that the γ is proportional to the bandwidth ratio, and the growth rate (amplitude in (5.8)) for each function is dependent on the chosen VSWR.

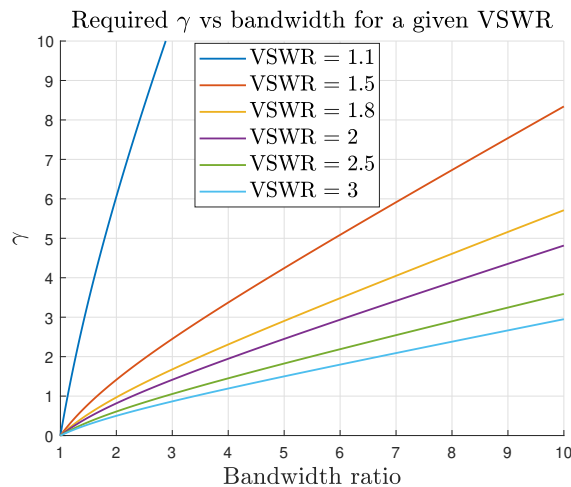


Figure 5.3: Bandwidth ratio design curves for a given VSWR.

Given that $\gamma = Z_e/R$, it becomes clear that a parallel-connected balun reduces the γ requirement by a factor of 4 when compared to a series-connected balun. For an explanation, the first case that will be considered is the series-connected topology. If nodes A and B in Fig. 5.1a replaces the load R in Fig. 5.2, then the cavity is in parallel with Z_L . When the cavity is at a quarter wavelength resonance, that is the cavity impedance approaches infinity, then only Z_L is seen at the input.

The second case for the parallel-connected topology follows similarly. When the nodes A and B in Fig. 5.1b replaces the load R in Fig. 5.2, then at quarter wavelength resonance the input observes $Z_L/4$. The parallel-connected case is also shown in Fig. 3.8. This shows the inherent 4:1 impedance transformation of parallel-connected baluns, and why this impedance transformation directly translates to an inherent 4:1 bandwidth ratio when compared to a serially connected balun. Formally, what the input “observes” in both cases is called the balun junction.

5.2 Design

The Phelan balun was designed around the sinuous antennas’ 300 Ω input impedance. This input impedance would become the baluns load. To match the 1-5 GHz band of the antenna, the bandwidth was chosen as 5:1 with a minimum VSWR of 2. With

this information, the required γ for would be calculated with (5.8). The characteristic impedance for the cavity in Fig. 3.7 was found empirically by [34] as

$$Z_{o,cavity} = 138 \log_{10} \left(\frac{D}{1.5d} \right) = \frac{1}{2} Z_e \quad (5.9)$$

and has a reported accuracy to within 0.07%. For (5.9), D refers to the diameter of the cavity and d is the outer diameter of the dummy rod, input and output lines. The physical and electrical design parameters are summarised in Table 5.1.

Table 5.1: Phelan balun design parameters

Description	Parameter	Value
Load impedance	Z_L	300 Ω
Outer diameter of coaxial lines	d	5.00 mm
Inner diameter of coaxial lines	N/A	4.55 mm
Cavity diameter/width	D	30.0 mm
Length of cavity	L	147. mm
Input coaxial line centre conductor diameter	N/A	2.00 mm
Output coaxial line centre conductor diameter	N/A	0.80 mm
Balun junction gap	N/A	2.00 mm

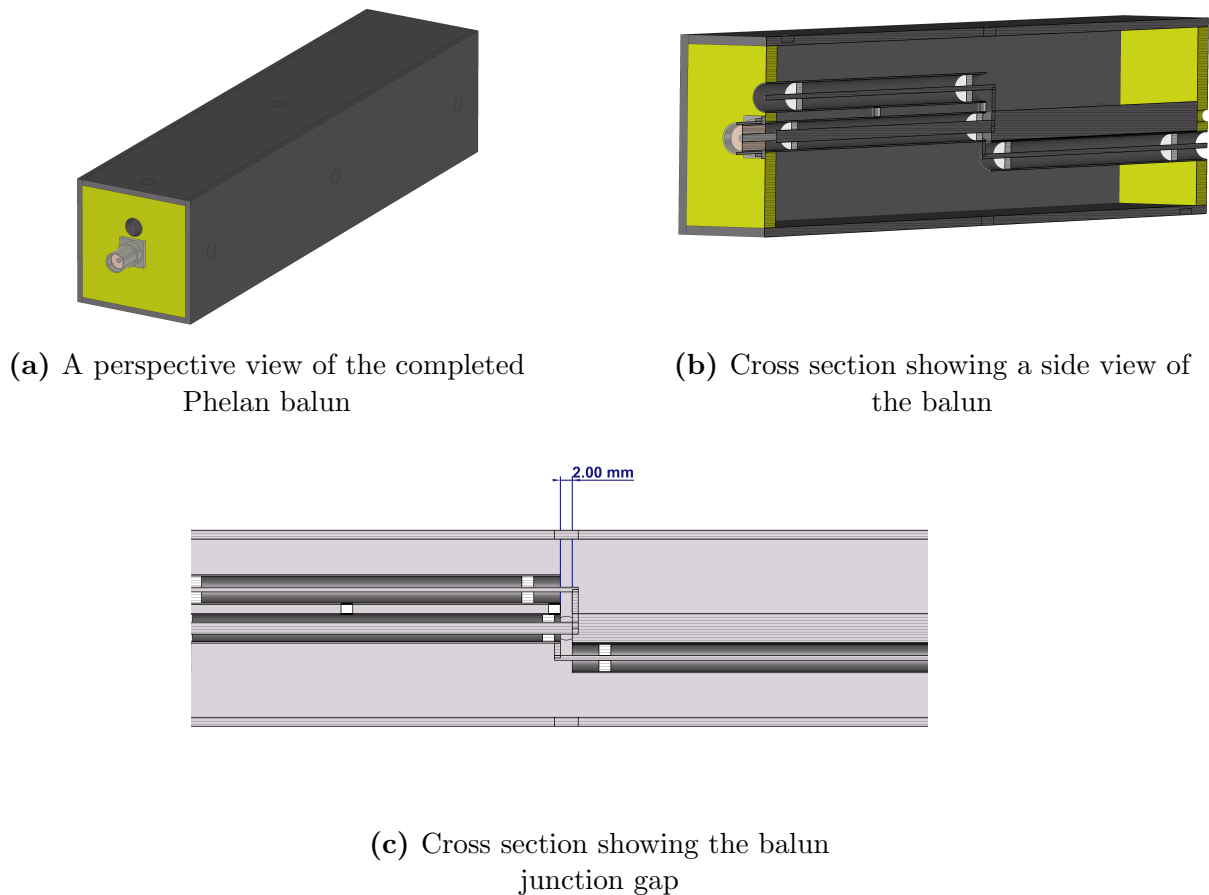


Figure 5.4: CST simulation models of the Phelan balun.

For the simulation, it was decided to use off-the-shelf components to ease fabrication and to get an idea of any complications that may arise. It should be noted that the length L was chosen post-priori to match SKA band 1 and 2, which combined is 0.35-1.76 GHz, as a test case. A higher frequency band would require a shorter length, which could increase fabrication difficulty. The balun junction gap was also found to be of critical importance. For this balun, if the gap was out by more than a millimetre, then the bandwidth and output balance would drop significantly.

Simulation Results

The reflection coefficient of the simulated balun is shown in Fig. 5.5. A $50\ \Omega$ waveguide port was used as a source at the input and the output was terminated with $300\ \Omega$ load ($150\ \Omega$ per port). The magnitude remains below -10 dB across the band of interest, resulting in 7:1 bandwidth, spanning 0.26-1.8 GHz.

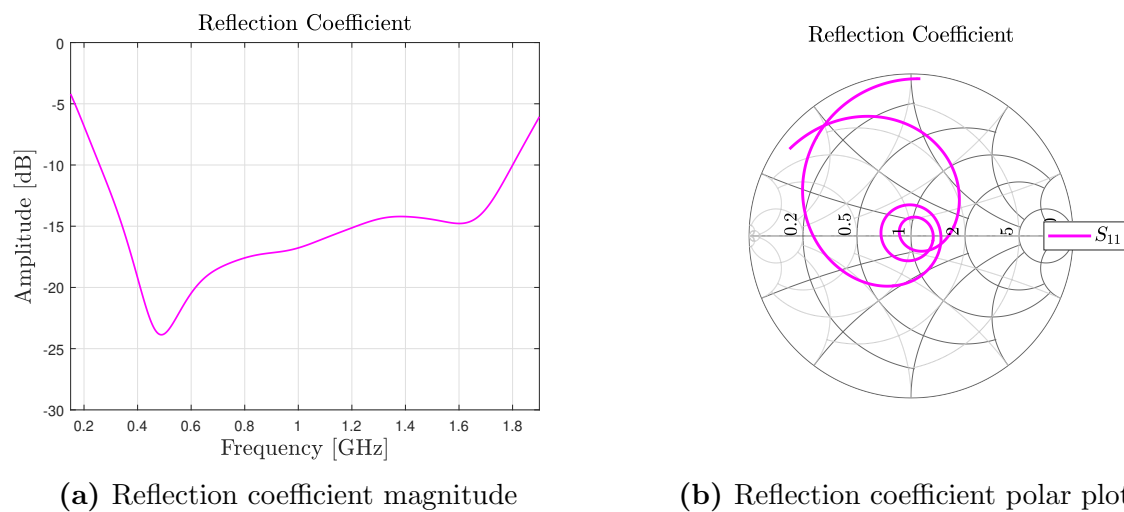


Figure 5.5: Simulated Phelan balun reflection coefficient.

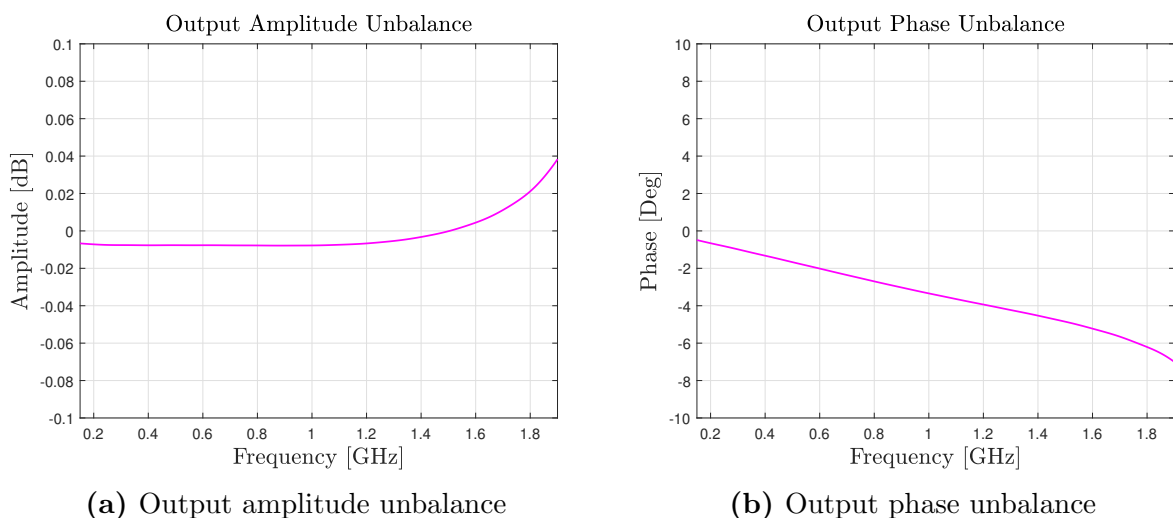


Figure 5.6: The Phelan balun's output ports unbalance.

The amplitude and phase unbalance at the output ports are shown in Fig. 5.6. This was calculated by taking the difference between the output ports' S-parameters magnitude and phase. The balun has good amplitude balance, with the difference remaining constant at -0.0075 dB across most of the band, reaching 0.02 dB at 1.8 GHz. In the 0.35 - 1.05 GHz range, the outputs have a phase unbalance of less than -4° , and reach a maximum unbalance of -6.2° at 1.8 GHz. The total phase unbalance is less than 3.5% across the band. Lastly, to ensure that the input power is distributed evenly amongst the output ports, the power accepted at each port is plotted. The Phelan balun was simulated with lossy aluminium, brass, and Teflon found in CST's standard material library. In Fig. 5.4, aluminium is represented by grey, and yellow is brass. Teflon is used in the SMA connector and to align the coaxial lines' inner conductors. While these lossy materials do not necessarily match the actual materials used during the manufacturing process, this was done to match the non-ideal materials as closely as possible.

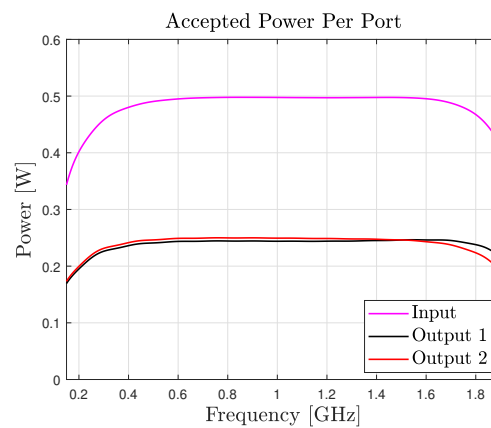
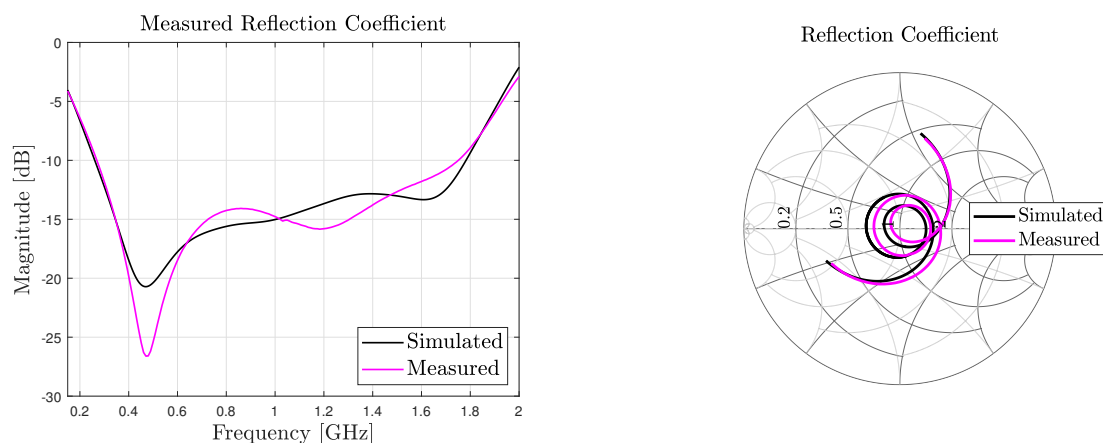


Figure 5.7: Power accepted per port showing that the input power divides evenly.

Fabrication and Measurements

A comparison between the measured and simulated reflection coefficient is shown in Fig. 5.8. It should be noted that the simulated results in this section are slightly dif-



(a) Reflection coefficient magnitude

(b) Reflection coefficient polar plot

Figure 5.8: Comparison between the simulated and measured reflection coefficient.

ferent from what is seen in Fig. 5.5. This difference is due to a different Z_L to match the fabricated version. After fabrication it was found that the departments' workshop had no 150Ω chip resistors, however, 160Ω versions were available for a total load of 320Ω . The simulation used for comparison here also uses a 320Ω load. Even with a load higher than 320Ω , the reflection coefficient remains well below -10 dB across the 0.26 - 1.747 GHz band. Thus, there is a remarkable agreement between the simulated and measured results, indicating that the balun had been built accurately. It is worth noting that the amplitude and phase unbalance could not be measured because of the custom coaxial lines' dimensions. Custom connectors would have to be designed and machined, which is out of the scope of this thesis. Images of the Phelan balun are shown in Fig. 5.9.

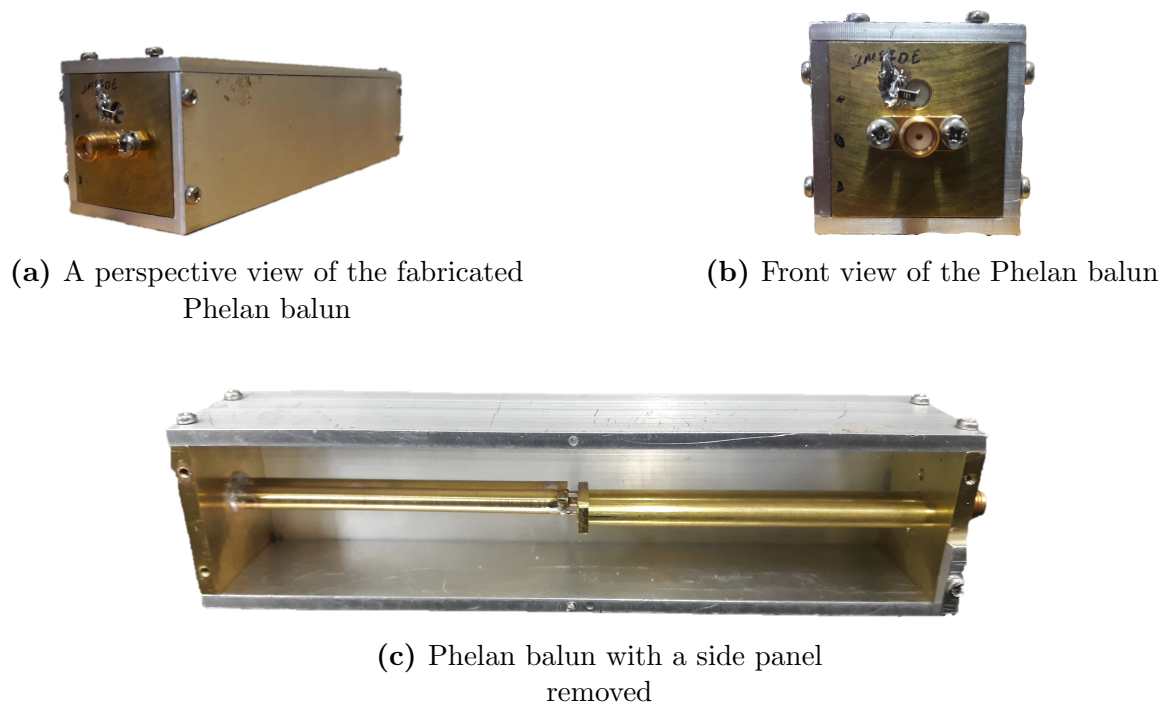


Figure 5.9: Fabricated Phelan balun.

5.2.1 Other Parallel-Connected Balun Topologies

To integrate the Phelan balun with the sinuous antenna, custom coaxial cables would have to be manufactured. While this is possible, it would be easier if both cables exited the balun on the same side. In [34], it is mentioned these parallel resonant balun topologies exist. An example of this can be seen in Fig. 5.10. The structure follows the parallel connections of a Phelan balun, where the input shield connect to output lines. The centre conductor of an output line B connects to the shield of the output line A and vice versa.

Simulation

The balun in Fig. 5.10 was designed to match the sinuous antenna using the same equations that were derived in section 5.2. A cross-section of the balun is shown in Fig. 5.11.

The reflection coefficient of this balun is shown in Fig. 5.11 where a 300Ω load is attached to the centre conductors of the output lines. While the result is not as good as the Phelan balun, it remains below -10 dB across the band and would be a good

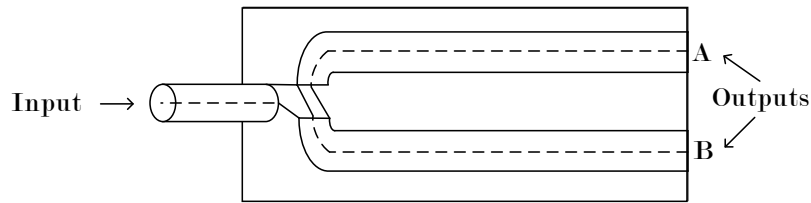


Figure 5.10: Another parallel connected balun topology, following [34].



Figure 5.11: Cross-section of simulated balun.

alternate balun. However, after consulting the departments' workshop, it was found to be too difficult to manufacture. The gap requirement is as critical as it was for the Phelan balun. The added bend for the output coaxial lines makes this balun impractical and only realisable in simulation. Thus it is concluded that if the Phelan balun is to be integrated with the sinuous antenna, currently the simplest option would be to manufacture custom output cables.

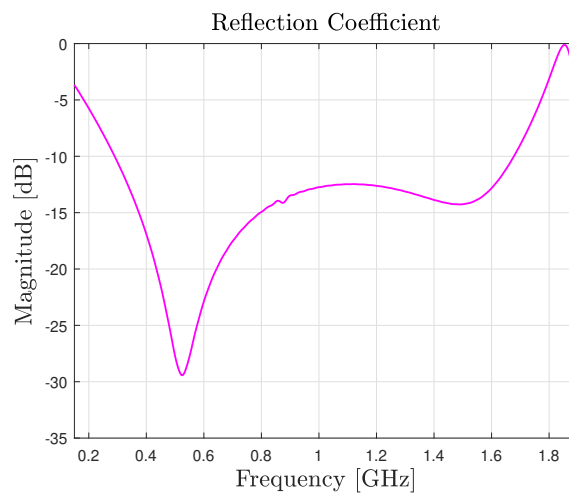


Figure 5.12: Simulated reflection coefficient of other parallel-connected balun topology.

5.3 Chapter Summary

Firstly, this chapter differentiates between series and parallel-connected baluns. It was found that parallel-connected baluns allow for a higher load impedance when compared to their series-connected counter-parts. The reason for this is due to the load topology.

Secondly, the design equations for a parallel-connected balun (the Phelan balun) is derived. As a result of the load topology, it is shown that this balun has an inherent 4:1 impedance transformation, leading to an inherent 4:1 bandwidth ratio.

Thirdly, the Phelan balun was designed, simulated, and fabricated. The simulated and measured reflection coefficient showed an excellent correlation, indicating that the model was simulated and manufactured correctly. This Phelan balun's reflection coefficient magnitude is well below -10 dB in the 0.26-1.8 GHz range, yielding a near 7:1 bandwidth ratio. This bandwidth covers the SKA's band 1 and 2. Lastly, another parallel-connected balun topology was briefly investigated in pursuit of an easier sinuous antenna integration option. While this option compared well to the Phelan balun, it was found to be impractical. It was concluded that the best option, currently, would be to manufacture custom output cables for the Phelan balun.

Chapter 6

Conclusion and Recommendations

6.1 Results Summary

The main focus of this thesis was to integrate a balun with the pyramidal sinuous antenna to provide a constant radiation pattern with rotational symmetry across frequency. The reason for the antenna pattern requirement is because the antenna and balun system is to be used as a reflector feed. The focus is then shifted to finding a suitable balun to match the high 300Ω input impedance of a sinuous antenna. A Marchand balun from previous work was characterised and results show a maximum amplitude unbalance of ± 0.2 dB and a maximum phase unbalance of 1.5° . This balun's simulated and measured reflection coefficient also remained below -10 dB across a 1.05-4.7 GHz band under a 300Ω load. This balun, therefore, was chosen for an initial integration.

To design the pyramidal sinuous antenna, the first objective was to analyse its performance and fabrication feasibility without a substrate on its arms. This was done to avoid the excitation of surface waves in the dielectric, which was shown to affect wide-band performance. Thus a 2-6 GHz pyramidal sinuous antenna was designed and fed via microstrip lines. This frequency range was chosen for manufacturing convenience, and the antenna can be scaled to any other 3:1 band (the SKA's band 1, which is 0.35-1.05 GHz for example). The simulated and measured results showed a differential reflection coefficient of below -10 dB across most of the band with a constant, symmetric radiation pattern. From this design, suggestions were made to ease the fabrication process, such as using thicker sinuous arms and allowing for a larger gap between feeding pins. This was implemented in the design of subsequent antennas.

The next objective was to design a suitable descrambling network to integrate the Marchand balun and a four-arm sinuous antenna. An existing network was considered first, however, it was found technically difficult to manufacture and had unequal reflection coefficient responses on both ports in simulation. A new network was designed and showed equal reflection coefficients at both ports while remaining below -10 dB. A two-arm antenna was designed in the 1-5 GHz band and simulated to ensure compatibility with the Marchand balun. The reflection coefficient remained below -10 dB across most of the band and the radiation pattern also retained symmetry.

A four-arm, balun fed sinuous antenna was designed to match the 1.05-4.7 GHz balun range. This design implemented the new descrambling network. The simulated reflection coefficient again remained below -10 dB for most of the band, with a shape consistent

with what was found in previous work for two-arm integrations. The radiation pattern also retained symmetry. With design confirmation, this version of the antenna and balun was manufactured. While the measured reflection coefficient was above the expected simulated results, pattern symmetry was retained and remained constant. The reason for the discrepancy between the simulated and measured results is because the balun was optimised for a 300Ω load, which did not include the antennas' reactance.

To improve the reflection coefficient, a Phelan balun was suggested due to its inherent 4:1 impedance transformation, which is better suited for high impedance loads. A prototype was designed for the 0.26-1.8 GHz range to include the SKA's band 1 and 2 (again, band 1 and 2 combined is 0.35-1.76 GHz). Both the simulated and measured reflection coefficient remained well below -10 dB for a 320Ω load. Simulations showed a constant amplitude unbalance of -0.0075 dB, and a maximum phase unbalance of 3.5% across the band.

Lastly, the antennas discussed here were also tested as feeds for the SKA's shaped offset Gregorian reflector. The simulated radiation patterns showed a BOR_1 efficiency better than 90% across their respective bands, and a total aperture efficiency of above 70%. For the four-arm antenna, the result confirms that Marchand baluns' amplitude and phase balance, as well as the performance of the descrambling network.

6.2 Recommendations

For further investigation, the following is recommended for improvement:

- Design a larger descrambling network to improve its physical robustness. This will also allow for vias to be included around each line. The inclusion of vias may further improve the isolation between the baluns.
- Integrating the Phelan balun with the sinuous antenna. This suggestion also includes further work with other Phelan balun topologies that will be relatively simple to manufacture and integrate. The recommended topology is a parallel-connected balun where both outputs exit on the same side.

Bibliography

- [1] P. E. Dewdney, P. J. Hall, R. T. Schilizzi, and T. J. L. W. Lazio, “The square kilometre array”, *Proceedings of the IEEE*, vol. 97, no. 8, pp. 1482–1496, Aug. 2009. DOI: 10.1109/JPROC.2009.2021005.
- [2] I. Heywood, F. Camilo, W. D. Cotton, *et al.*, “Inflation of 430-parsec bipolar radio bubbles in the Galactic Centre by an energetic event”, *Nature*, vol. 573, no. 7773, pp. 235–237, Sep. 2019, ISSN: 0028-0836. DOI: 10.1038/s41586-019-1532-5.
- [3] P. E. Dewdney, R. Braun, and W. Turner, “The mid-frequency telescope for the square kilometre array (ska-mid)”, in *2017 XXXIInd General Assembly and Scientific Symposium of the International Union of Radio Science (URSI GASS)*, Aug. 2017, pp. 1–4. DOI: 10.23919/URSIGASS.2017.8105425.
- [4] R. Lehmensiek and I. P. Theron, “Minimizing the meerkat system noise temperature”, in *2014 XXXIth URSI General Assembly and Scientific Symposium (URSI GASS)*, Aug. 2014, pp. 1–4. DOI: 10.1109/URSIGASS.2014.6930057.
- [5] V. Rumsey, “Frequency Independent Antennas”, in *IRE International Convention Record*, vol. 5, Institute of Electrical and Electronics Engineers, 1958, pp. 114–118. DOI: 10.1109/IRECON.1957.1150565.
- [6] R. H. DuHamel, “Dual Polarized Sinuous Antennas”, U.S. Patent 4,658,262, 1987.
- [7] Y. Mushiake, “Self-Complementary Antennas”, *IEEE Antennas and Propagation Magazine*, vol. 34, no. 6, pp. 23–29, Dec. 1992, ISSN: 10459243. DOI: 10.1109/74.180638.
- [8] N. Mutonkole, “Study of a Wideband Sinuous Feed for Reflector Antenna Applications”, Master’s thesis, Stellenbosch University, 2013.
- [9] N. Steenkamp, “Design of a Wideband Sinuous Antenna for Radio Telescope Applications”, Master’s thesis, Stellenbosch University, 2018.
- [10] M. Johnston, “Wideband Balun Design for the Pyramidal Sinuous Antenna”, Master’s thesis, Stellenbosch University, 2019.
- [11] G. A. Deschamps, “Impedance Properties of Complementary Multiterminal Planar Structures”, *IRE Transactions on Antennas and Propagation*, vol. 7, no. 5, pp. 371–378, 1959, ISSN: 00961973. DOI: 10.1109/TAP.1959.1144717.
- [12] J. L. Volakis, *Antenna Engineering Handbook*. McGraw-Hill Education, 1993, p. 1401, ISBN: 9781259644696.
- [13] C. A. Balanis, *Antenna Theory: Analysis and Design*. Wiley-Interscience, 2005, p. 1072, ISBN: 9781118642061.
- [14] Altair, *FEKO*, version FEKO 2018. [Online]. Available: <https://altairhyperworks.com/product/FEKO>.

- [15] P. Gonnet, A. Sharaiha, C. Terret, and A. Skrivervik, “Feeding networks for sinusoidal antennas”, *Microwave and Optical Technology Letters*, vol. 20, no. 3, pp. 195–200, Feb. 1999, ISSN: 08952477. DOI: 10.1002/(SICI)1098-2760(19990205)20:3<195::AID-MOP15>3.0.CO;2-C.
- [16] A. Jafargholi and M. Kamyab, “A new approach for feeding sinusoidal antenna”, *AEU - International Journal of Electronics and Communications*, vol. 65, no. 4, pp. 312–319, Apr. 2011, ISSN: 14348411. DOI: 10.1016/j.aeue.2010.03.010.
- [17] K. M. P. Aghdam, R. Faraji-Dana, and J. Rashed-Mohassel, “The sinusoidal antenna-A dual polarized feed for reflector-based searching systems”, *AEU - International Journal of Electronics and Communications*, vol. 59, no. 7, pp. 392–400, 2005, ISSN: 16180399. DOI: 10.1016/j.aeue.2004.11.046.
- [18] R. Gawande and R. Bradley, “Towards an ultra wideband low noise active sinusoidal feed for next generation radio telescopes”, *IEEE Transactions on Antennas and Propagation*, vol. 59, no. 6 PART 1, pp. 1945–1953, Jun. 2011, ISSN: 0018926X. DOI: 10.1109/TAP.2011.2122238.
- [19] J. Yin, J. Yang, M. Pantaleev, and L. Hellndner, “The circular eleven antenna: A new decade-bandwidth feed for reflector antennas with high aperture efficiency”, *IEEE Transactions on Antennas and Propagation*, vol. 61, no. 8, pp. 3976–3984, 2013, ISSN: 0018926X. DOI: 10.1109/TAP.2013.2263275.
- [20] R. A. Chipman, *Theory and Problems of Transmission Lines*. McGraw-Hill Book Company, 1968, pp. 1–248, ISBN: 9780070107472.
- [21] D. M. Pozar, *Microwave Engineering*. Wiley, 2005, pp. 1–756, ISBN: 9780470631553. DOI: TK7876.P692011.
- [22] D. S. Prinsloo, P. Meyer, R. Maaskant, and M. Ivashina, “Design of an active dual-mode antenna with near hemispherical Field of View coverage”, *Proceedings of the 2013 International Conference on Electromagnetics in Advanced Applications, ICEAA 2013*, pp. 1064–1067, 2013. DOI: 10.1109/ICEAA.2013.6632405.
- [23] W. Fan, A. Lu, L. L. Wai, and B. K. Lok, “Mixed-mode S-parameter characterization of differential structures”, in *Proceedings of 5th Electronics Packaging Technology Conference, EPTC 2003*, Institute of Electrical and Electronics Engineers Inc., 2003, pp. 533–537, ISBN: 0780382056. DOI: 10.1109/EPTC.2003.1271579.
- [24] R. Lehmensiek, I. P. Theron, and D. I. L. de Villiers, “Deriving an Optimum Mapping Function for the SKA-Shaped Offset Gregorian Reflectors”, *IEEE Transactions on Antennas and Propagation*, vol. 63, no. 11, pp. 4658–4666, Nov. 2015, ISSN: 0018926X. DOI: 10.1109/TAP.2015.2477408.
- [25] P.-S. Kildal, *Foundations of Antenna Engineering: A Unified Approach for Line-of-Sight and Multipath*. Kildal Antenn AB, 2015, ISBN: 978-91-637-8515-3. [Online]. Available: <https://www.kildal.se/downloads/>.
- [26] P. S. Kildal, “Factorization of the feed Efficiency of Paraboloids and Cassegrain Antennas”, *IEEE Transactions on Antennas and Propagation*, vol. 33, no. 8, pp. 903–908, 1985, ISSN: 15582221. DOI: 10.1109/TAP.1985.1143689.
- [27] P. S. Kildal and Z. Sipus, “Classification of Rotationally Symmetric Antennas as Types BOR0 and BOR1”, *IEEE Antennas and Propagation Magazine*, vol. 37, no. 6, p. 114, 1995, ISSN: 10459243. DOI: 10.1109/MAP.1995.482130.

- [28] J. Yang, S. Pivnenko, and P. S. Kildal, “Comparison of two decade-bandwidth feeds for reflector antennas: The Eleven Antenna and quadridge horn”, in *EuCAP 2010 - The 4th European Conference on Antennas and Propagation*, 2010, ISBN: 9788476534724.
- [29] A. C. Ludwig, “The Definition of Cross Polarization”, *IEEE Transactions on Antennas and Propagation*, vol. 21, no. 1, pp. 116–119, 1973, ISSN: 15582221. DOI: 10.1109/TAP.1973.1140406.
- [30] A. Grebennikov, *RF and Microwave Transmitter Design*. John Wiley and Sons, Jul. 2011, ISBN: 9780470520994. DOI: 10.1002/9780470929308.
- [31] T. A. Milligan, *Modern Antenna Design*. Wiley-IEEE Press, 2005, ISBN: 9780471457763. DOI: 10.1002/0471720615.
- [32] W. K. Roberts, “A New Wide-Band Balun”, *Proceedings of the IRE*, vol. 45, no. 12, pp. 1628–1631, 1957, ISSN: 00968390. DOI: 10.1109/JRPROC.1957.278293.
- [33] G. Oltman, “The Compensated Balun”, *IEEE Transactions on Microwave Theory and Techniques*, vol. MTT-14, no. 3, pp. 112–119, 1966, ISSN: 15579670. DOI: 10.1109/TMTT.1966.1126188.
- [34] H. R. Phelan, “A Wide-Band Parallel-Connected Balun”, *IEEE Transactions on Microwave Theory and Techniques*, vol. 18, no. 5, pp. 259–263, May 1970, ISSN: 15579670. DOI: 10.1109/TMTT.1970.1127208.
- [35] J. H. Cloete, “EXACT DESIGN OF THE MARCHAND BALUN.”, *Conference Proceedings - European Microwave Conference*, pp. 480–484, 1979. DOI: 10.1109/euma.1979.332751.
- [36] V. Trifunoviä and B. Jokanoviä, “Review of Printed Marchand and Double Y Baluns: Characteristics and Application”, *IEEE Transactions on Microwave Theory and Techniques*, vol. 42, no. 8, pp. 1454–1462, 1994, ISSN: 15579670. DOI: 10.1109/22.297806.
- [37] Dassault Systemes, *CST Studio Suite*, version 2019.07. [Online]. Available: <https://www.3ds.com/products-services/simulia/products/cst-studio-suite/>.
- [38] National Instruments, *NI AWR Design Environment*, version 14.01r build 9173 Rev5 (113322). [Online]. Available: <https://www.awr.com/software/products/ni-awr-design-environment>.
- [39] R. Lehmensiek and D. I. L. de Villiers, “Aperture efficiency performance limits of the ska reflector system”, in *2017 IEEE International Symposium on Antennas and Propagation USNC/URSI National Radio Science Meeting*, Jul. 2017, pp. 989–990. DOI: 10.1109/APUSNCURSINRSM.2017.8072537.